Physics and Control of Flow Over a Thin Airfoil using Nanosecond Pulse DBD
Actuators

THESIS

Presented in Partial Fulfillment of the Requirements for the Degree Master of Science in
the Graduate School of The Ohio State University

By

Ata Ghasemi Esfahani, B.Sc.

Graduate Program in Mechanical Engineering

The Ohio State University

2017

Master's Examination Committee:

Professor Mo Samimy, Advisor

Professor James Gregory

Professor Igor Adamovich

Abstract

Flow separation leading to stall imposes considerable performance penalties on lifting surfaces. Limitations in flight envelope and loss of control are among the chief reasons for the interest in the aeronautical research community for better understanding of this phenomenon. This problem is relevant to a wide range of applications from wind turbines to rotorcraft blades and from the wings of super maneuverable fighter aircraft to agile micro air vehicles. The results of experiments designed to investigate excitation of flow over an airfoil with leading edge separation at a post-stall angle of attack with nanosecond pulse dielectric barrier discharge actuators are presented. The subject airfoil is designed with a small radius of curvature that potentially challenges the task of flow control as more centrifugal acceleration around leading is required to successfully reattach the flow. The Reynolds number based on the chord was fixed at $5 \cdot 10^5$, corresponding to a freestream flow of approximately 37 m/s. An angle of attack of 19° was used and a single plasma actuator was mounted near the leading edge of the airfoil. Fully separated flow on the suction side extended well beyond the airfoil with naturally shed vortices generated at a Strouhal number of 0.60. Excitation at very low (impulse excitation) to moderate (~1) Strouhal numbers at the leading edge generated organized coherent structures in the shear layer over the separated region with a shedding Strouhal

number corresponding to that of the excitation, synchronizing the vortex shedding from leading and trailing edges. Excitation around the shedding Strouhal number promoted vortex merging while excitation at higher Strouhal numbers resulted in smaller, weaker structures that quickly developed and disintegrate over the airfoil. Excitation around the shedding Strouhal number significantly increased both the lift and drag, but high frequency excitation moved the separation point downstream and reduced both the lift and drag. The primary mechanism of control is the excitation of instabilities associated with the vortices shed from leading edge. The excitation generates coherent large-scale structures that entrain high-momentum fluid into the separation region to reduce the separation and/or accelerate the flow over the airfoil and to modify the lift and drag properties. The baseline showed some spanwise non-uniformity both on and off the surface. Excitation at low Strouhal numbers ($0.3 < St_e < 0.78$) led to the emergence of spiral nodes near the trailing edge of the airfoil surface and a three-dimensional surface topology (similar to an asymmetric stall cell pattern). Off-surface stereo PIV data suggests, however, that the flow field remains nearly two-dimensional. Excitation at a Strouhal number of 2.04 produces distinct 3-D features in the stereo PIV data. Further increases in excitation Strouhal number result in slight acceleration of the flow near the leading edge and formation of two symmetric stall cells. Increasing the excitation Strouhal number even further results in more well-defined stall cells. This effect saturates around $St_e = 6.0$ and further increases in excitation frequency have minimal effects on the stall cells. This is surprising as the scientific community had hitherto believed stall cells

to form only over thick airfoils. The results clearly indicate that the instabilities responsible for stall cell formation are present on thin airfoils as well as thick ones and perhaps the lack the appropriate disturbance environment is the reason stall cells have hitherto not been observed on thin airfoils.

"It is the glory of God to conceal a matter; to search out a matter is the glory of kings."

Proverbs 25:2

This work is dedicated to my beloved family. Thank you for your endless love,

sacrifices, prayers and support.

Acknowledgments

Working with world-class facilities and interacting with and learning from the most accomplished researchers in the field is an invaluable experience and I'm forever indebted to my advisor, Prof. Mo Samimy, for giving me that opportunity and freedom to explore different avenues of research. I would like to thank Drs. Nathan Webb, Chris Clifford and Ching-Wen Kuo for sharing their wealth of knowledge and experience with me and all the members of Gas Dynamics and Turbulence Laboratory for the stimulating discussions and more importantly, their friendship. I would also like to acknowledge Josh Gueth for being there when things in the lab ground to halt.

I wish to specifically thank Prof. James Gregory, Dr. Kevin Disotell and Anshuman Pandey for the lengthy discussions on pressure sensitive paint measurements and providing me with the necessary equipment to conduct my experiments. I could not have done the PSP experiments without the invaluable help and support of Andito Eddy and Justin Niehaus.

I run into a plethora of issues and problems while working with nanosecond pulsers but the technical help and assistance from the members of Non-Equilibrium

Thermodynamics Lab, specifically Prof. Igor Adamovich, kept my pulsers going and my research afloat.

Special recognition is reserved for my family for their continuous encouragement and support. They instilled in me a love for knowledge and kept me going when nothing else could.

Vita

14 October 1990..…………………………Born Wigan, England

2012-2013 ....…………Undergraduate Research Assistant

AUTSat Research Center

Amirkabir University of Technology

2013...…………Undergraduate Teaching Assistant

Aerospace Engineering Department

Amirkabir University of Technology

December 2013 ....…………………..B.S Aerospace Engineering

Amirkabir University of Technology

2014...………..………………. Research Engineer

DANA Aerodynamics and Turbomachinery Laboratory

Amirkabir University of Technology

2015-2016 ....……………… Graduate Research Associate

Department of Mechanical and Aerospace Engineering

The Ohio State University

2017...…………...… Graduate Teaching Associate

Department of Mechanical and Aerospace Engineering

The Ohio State University

Publications

Conference Publications

1. Moeini, E., **Esfahani, A**., Sedghi, V., Karimian, S., "Empirical Evaluation of Thermal Contact Resistance of Bolted Joint Configurations fitted with Various Interface Materials under Vacuum Conditions", 64th International Astronautical Conference, IAC-13.C2. P.47.p1.x2294, 2013
2. **Esfahani, A**., Singhal, A., Clifford, C. J., and Samimy, M., "Flow Separation Control over a Boeing Vertol VR-7 using NS-DBD Plasma Actuators," 54th AIAA Aerospace Sciences Meeting, 2016-0843
3. **Esfahani, A**., Webb, N. J., and Samimy, M., "Stall Cell Formation over a Boeing Vertol VR-7 Airfoil," 55th AIAA Aerospace Sciences Meeting, 2017-1577

Journal Publications

1. **Esfahani, A**., Webb, N. J., and Samimy, M., "Stall Cell Formation over a Boeing Vertol VR-7 Airfoil," Experiments in Fluids, in review
2. **Esfahani, A**., Webb, N. J., and Samimy, M., "Effects of Low and High-Frequency Excitation with NS-DBD Actuators on a Boeing Vertol VR-7 Airfoil," Experiments in Fluids, in preparation

Fields of Study

Major Field: Mechanical Engineering

Studies in: Aerodynamics, Fluid Mechanics, Flow Control, Optical Diagnostics, Instabilities

Table of Contents

List of Figures

xvi

xviii

xx

xxiii

Chapter 1: Introduction

Rotorcraft have a unique place in the aeronautics enterprise. Their vertical takeoff and landing, and hover capabilities allow them unprecedented access to locations physically inaccessible to fixed-wing aircraft. The most familiar rotorcraft is the helicopter, widely used in both civil and military applications. However, helicopters have a fundamentally limited forward flight speed. A traditional helicopter typically utilizes a large rotor atop the aircraft that is solely responsible for both lift and thrust. The rotor faces two major issues during forward flight: compressibility effects and dynamic blade stall. Forward flight increases the rotor's relative speed on the advancing blade side and decreases it on the retreating blade side. On the advancing blade side, the maximum rotor tip speed is typically constrained to avoid tip losses due to compressibility effects [1]. On the retreating blade side, a more aggressive angle of attack is required to balance lift and prevent roll, which could lead to retreating blade stall [2]. The combination of these two effects limits the maximum achievable forward flight speed. Time-sensitive missions, such as search and rescue operations, necessitate the development of rotorcraft with greater forward flight speeds. Slowed-rotor compound vehicles are an emerging class of rotorcraft which achieve that goal by incorporating aspects of

1

xed-wing aircraft. Two examples of such compound vehicles are the Sikorsky X2 [3] and the Eurocopter X3 [4, 5], shown in Fig. 1.1. Slowed-rotor compound vehicles overcome the forward flight limitation by adding an auxiliary form of propulsion, such as a pusher fan, and short wings for increased lift [6]. The addition of a pusher fan, for example, relieves the main rotor of some or all thrust responsibilities and similarly the wing area provides supplemental lift during cruise. Since the main rotor is no longer the sole source of lift and thrust, it may spin more slowly during cruise, allowing for increased maximum forward velocity of the vehicle. However, the simultaneous increase in forward speed and decrease in rotor speed introduces a new issue: a significant portion of the retreating blade side becomes immersed in reverse flow creating a wake and a large drag penalty is incurred [7].

The present work seeks to understand the relevant flow physics and to explore flow control over VR-7 airfoil in massively separated flow conditions. Flow control is achieved by using nanosecond dielectric barrier discharge (NS-DBD) plasma actuators. These actuators are surface mounted devices composed of two electrodes separated by a dielectric barrier. The actuators utilize an input signal of periodic pulses that are 2 of high-voltage and short duration, resulting in rapid plasma formation. Unlike the more widely-studied alternating current DBD actuators (AC-DBDs), NS-DBDs exert a negligible body force on the flow [10]. Instead, rapid heating results in thermal and subsequent pressure perturbations that are capable of exciting flow instabilities [10], in a manner similar to that of another class of plasma actuators called localized arc filament

2

plasma actuators [11]. NS-DBDs have been proven as an effective control technique for leading-edge blade stall even at high speeds (typical aircraft take-off and landing speed) [12].

Chapter 2: Background

2.1 Separation Control

Improving the performance of rotorcraft is of paramount importance if they are to meet the future challenges. Eliminating, or at least alleviating, flow separation over rotorcraft blades could potentially bring about significant performance improvements for this class of aircraft. The airspeed of the retreating blade in rotorcraft decreases as result of an increase in forward flight speed. To compensate for the ensuing loss of lift due to a reduction in relative wind speed, the angle of attack of the retreating blade must increase so that the lift generated throughout the rotor disk is equally distributed. Flying at higher forward airspeeds necessitates a further increase in blade angle of attack and that would eventually lead to rotor stall. Commonly referred to as retreating blade stall, this phenomenon limits the highest speed that a rotorcraft can attain in forward flight[1]. Active flow control techniques present have the potential to provide viable solutions for this problem and plasma-based actuators due to their wide bandwidth, high amplitude[2]–[4] and absence of moving parts are promising candidates for implementation of active flow on rotorcraft blades.

Dielectric barrier discharge actuators driven by AC waveforms have been shown to have control authority at relatively low Reynolds numbers but scaling their effect for successful implementation in high speed flows requires the use of thicker dielectrics and higher voltages[5]–[8]. Even when these changes are implemented, despite the fact that the body force produced by an actuator using a thick dielectric and driven by higher voltages might be as high as 20 times the body force induced by an actuator using a thin Kapton dielectric[9], there is a limit to the effectiveness of DBD actuators driven by AC waveform[7]. An alternative, first investigated by Roupassov et al.[10]–[12] is to supply the asymmetric single dielectric barrier discharge actuators with nanosecond high voltage DC pulses with pulse repetition rates that are varied from less than 100 Hz to several KHz. These actuators have demonstrated control authority at relatively higher flow speeds[12]–[19] as their control mechanism is not momentum-based which is in direct contrast to AC driven DBD actuators.

The results of the several studies conducted by Roupassov et al.[10], [12], Che at al.[20], Popov at al.[21], Correale et al.[22], Starokovskii et al.[23] Little et al.[15] and Takashima et al.[24], [25] point to the fact that nanosecond pulse driven DBD actuators mainly affect the flow through generating rapid, localized Joule heating that can excite the instabilities in the flow leading to the generation of coherent structures which promote mixing in the flow[26]–[29]. A distinctive signature of the rapid localized heating generated by the mentioned actuators is the generation of compression waves that are originated near the discharge[23], [24], [26], [28]. These waves have been reported to

5

be formed by discharge filaments[23], [28], [30] but it is not clear whether they significantly contribute to the control authority of the NS-DBD actuators[26]. Reports by Correale at al.[22] and Dawson et al.[28] indicate that the strength of the compression waves strongly depends on discharge voltage.

This work aims to study the interaction of the nanosecond pulse driven DBD actuators installed over a VR-7 rotorcraft airfoil with a low-Reynolds number flow. As the characteristics of the airfoil selected for this study are not well documented in the existing literature, the baseline model has been characterized using various diagnostic methods to provide an insight into the behavior of this airfoil at pre and post-stall regimes. One particular aspect of the selected airfoil that seriously challenges successful implementation of any flow control technique is its small radius of curvature leading edge. According to Greenblatt and Wygnanski[31], larger momentum coefficients are required to achieve successful control over an airfoil with a smaller leading edge radius of curvature. Also, notable in their study, which was focused on NACA 0012 and 0015 airfoils, was the conclusion that actuation at higher Strouhal numbers was advantageous when implemented over NACA 0012 airfoil. Compared to a NACA 0012 airfoil, the model studied in this work designed with a leading edge that has a slightly smaller radius of curvature and this suggests that the previously reported unsteadiness in separation and reattachment near stall angle[31], [32] might be observed.

Based on the preceding remarks, an important aspect of the present study that differentiates it from the works done on NS-DBD actuators hitherto is the implementation

of these actuators on a thin, asymmetric airfoil with leading edge separation. Reports of the studies conducted by Little et al.[15], [19], Correale et al.[22] and Rethmel et al.[17] on thick airfoils (NASA EET and NACA 0015 respectively) point the effectiveness of excitation at lower Strouhal numbers St ≈ O(1). In addition, in the small existing body of work on NS-DBD actuators, the merits of forcing at higher Strouhal numbers, mentioned in the works of Amitay and Glezer[33] and Glezer et al.[34], are not explored and therefore there is no information on how the flow would respond when forced by a NS-DBD actuator at high frequencies.

As forcing at low and high Strouhal numbers hypothetically rely on different mechanisms to achieve control, the results of forcing experiments are presented in two separate sections. This segment outlines the physics of flow response to actuation at Strouhal numbers of O(1). Several studies in the past have identified signature characteristics of a flow forced at such frequencies[33]–[37]. Forcing at low reduced frequencies primarily relies on relatively narrowband receptivity of the separated shear layer and wake to any forcing that would modify the global characteristics of the flow field via generating large-scale structures that promote mixing. According to Gelzer et al.[33], [34] a Coanda-like deflection of the separated shear layer results in the convection of the shear layer vortices downstream in close proximity to airfoil surface and an increase in circulation around the airfoil which a consequence of dominate shedding in the wake. It must be noted that in such an approach to control, the time-scale of convection over the airfoil length is in the order of actuation period. This results in a potentially undesirable phenomenon in which

periodic shedding of vorticity concentration into the wake brings about oscillations in the forces experienced by the airfoil[38]. This can be circumvented by forcing at higher frequencies as reported previously by several authors. The comparison between the effects of forcing the flow at low versus high Strouhal numbers can be seen in Figure 1 where low-frequency forcing by synthetic jet actuators leads to the generation of coherent vortical structures that are absent at the high-frequency forcing regime.
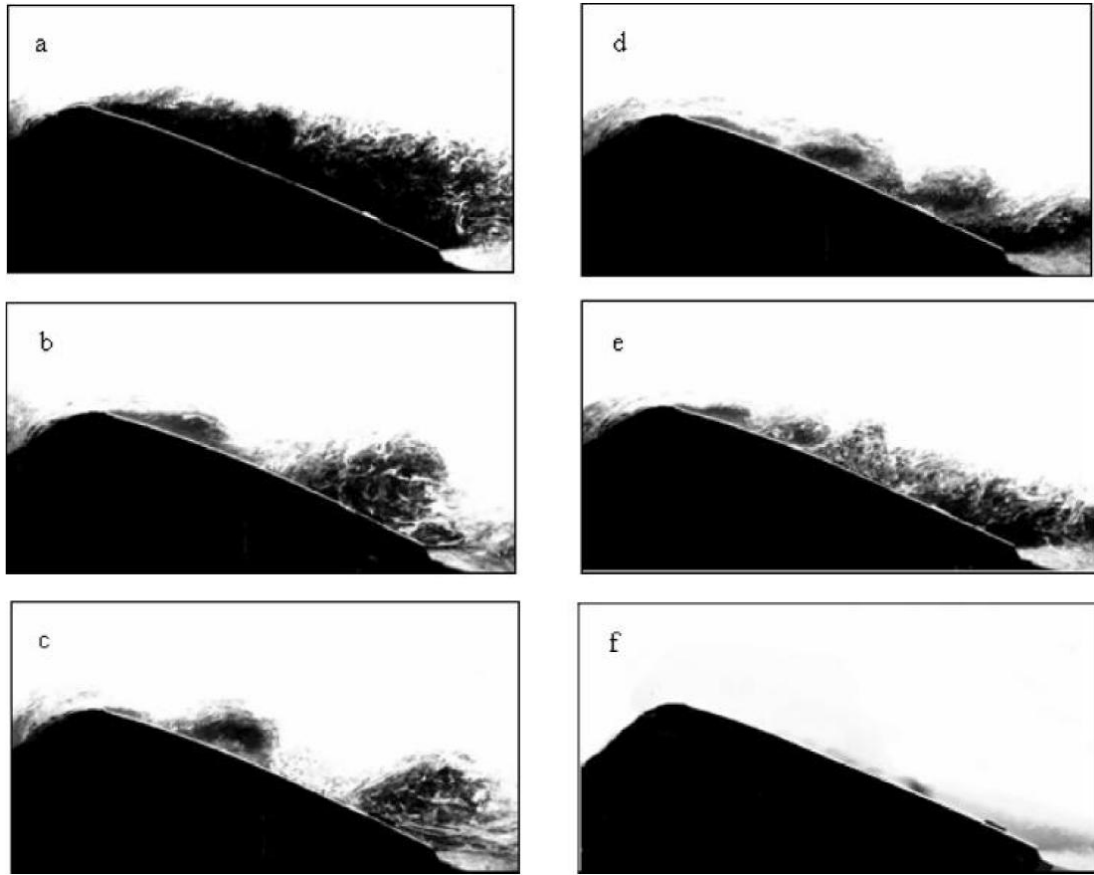
Figure 1. Phase-locked smoke visualization of the flow at different excitation Strouhal numbers, $St_f = 0.95$ to 10 by Glezer *et al.* [34]

This work seeks to explore the physics of low and high-frequency flow excitation and determine the control mechanism of each excitation regime. Flow development over the separated flow region has been studied using time-averaged and phase-locked velocity distributions to ascertain the excitation regime effects on the time-averaged flow field and the development of coherent structures over the airfoil and in the wake region, respectively. Wake pressure spectra has also been acquired to further illustrate the flow field development. Finally, the data set is complemented by time-averaged surface pressure distributions obtained under various flow excitation frequencies. These results are then compared with the existing works that have employed other flow actuation means in order to underline the differences between NS-DBD actuator control mechanisms and other flow excitation approaches.

2.2 3-D Flow Fields in Massively Separated Flows

Flow separation leading to stall imposes considerable performance penalties on lifting surfaces. Limitations in flight envelope and loss of control are among the chief reasons for the interest in the aeronautical research community for better understanding of this phenomenon. This problem is relevant to a wide range of applications from wind turbine to rotorcraft blades and from the wings of super maneuverable fighter aircraft to agile micro air vehicles.

The stall characteristics of various airfoils are directly related to their geometry where thick airfoils are known to undergo a so-called gentle stall in the form of trailing edge

separation which progressively moves towards the leading edge with increase in the angle of attack. Thin airfoils, on the other hand, display what is commonly referred to as abrupt stall characteristics where a sudden flow separation from leading edge leads to the abrupt loss of lift [39]. The leading edge radius of curvature dictates the momentum required to maintain attached flow and this, in turn, shapes the stalling behavior of thin and thick airfoils [31]. The emergence of three-dimensional flow features in post-stall regimes further complicates the stall phenomenon and leads to manifestation of effects such as lift and drag modulation and variation along the airfoil span [40], [41]. Consequently, studies in which only two-dimensional measurement techniques are employed where three-dimensional features might be present may result in under- or overestimation of the loads experienced by the airfoil.

The mushroom-shaped three-dimensional flow features, referred to as stall cells, have been the subject of investigation for at least 40 years with early reports of their appearance by Gregory[42] dating back to 1971. Further investigation of stall cells by Winkelman and Barlow[43], Weihs and Katz[44], Boiko et al.[45], Yon and Katz[46], Broeren and Bragg [47] and Schewe[48] using flow visualization techniques such as tufts and surface oil flow visualization shed light on the conditions in which stall cells emerge and also resulted in derivation of empirical relations that could be used for predicting the number and wavelength of stall cells. A better understanding of stall cells has been obtained recently through the use of advanced optical diagnostic techniques such stereo PIV and pressure sensitive paints. Studies by Manolesos and Voutsinas[49], DeMauro et

al.[50], Dell'Orso et al.[51], Disotell and Gregory[52] and Ragni and Ferreira[41] have used two-component planar and stereo PIV not only to determine the extent of the stall cells, but also to study their temporal evolution, extract frequency content in the reversed flow region and obtain the distribution of vorticity and Reynolds stress concentrations within the flow field. Disotell et al. [53] used fast-responding pressure sensitive paint to obtain the pressure distribution over a pitching wind turbine blade in the presence of stall cells. While advances in flow diagnostics have helped to further understanding of the stall cells and their characteristics, the underlying mechanisms that led to their emergence in post-stall flows are not yet well-understood.

Early work of Weihs and Katz [44] postulated that the stall cells are formed due to the excitation of the Crow instability [54] whereby the interaction between the vortex lines shed from the leading and trailing edges of the airfoil leads to the formation of vortex rings which impinge on the airfoil surface and form the stall cells. This mechanism is displayed schematically in Figure 2.
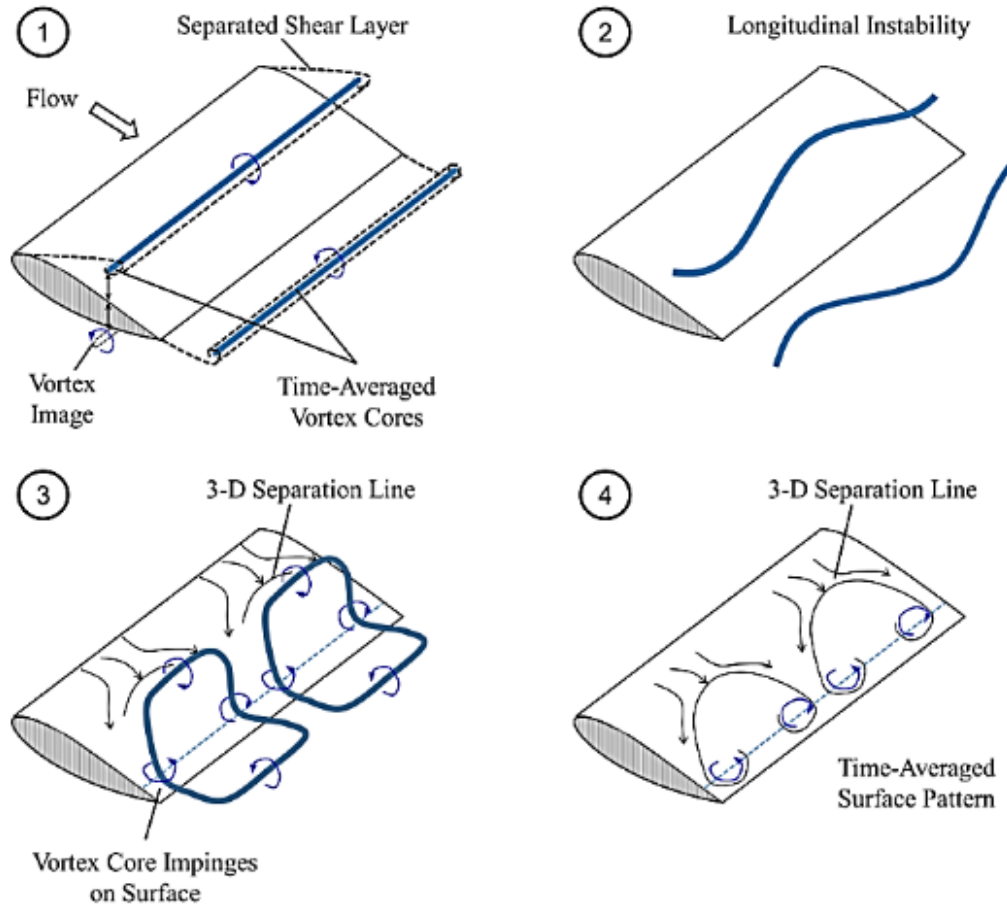
Figure 2. Stall cell formation mechanism suggested by Weihs and Katz [44]

Yon and Katz [46] in their study concluded that shear layer roll up is not the mechanism responsible for the formation of stall cells. Rodriguez and Theofilis [55] performed some numerical and theoretical work aimed at exploring the formation mechanism of stall cells with a different approach. They perturbed a low-Reynolds flow having a laminar separation bubble with two- and three-dimensional disturbances. They found that disturbances of any amplitude would induce three-dimensional features as the

investigated flow was unstable due to the presence of the low-momentum reversed flow region. This, in turn, led to the breakdown of the flow in the spanwise direction and formation of stall cells. Manolesos and Voutsinas [49] combined stereo PIV data and CFD simulations to offer a model for the vortex system over an airfoil when a stall cell is present. They concluded that three types of line vortices are present in such a flow field: a bent and deformed shear layer line vortex, trailing edge vortex and a pair of streamwise vortices that impinge on the airfoil surface and create the so-called spiral nodes commonly observed in surface flow visualization experiments. The vortex system established with the emergence of stall cells can be seen in Figure 3.
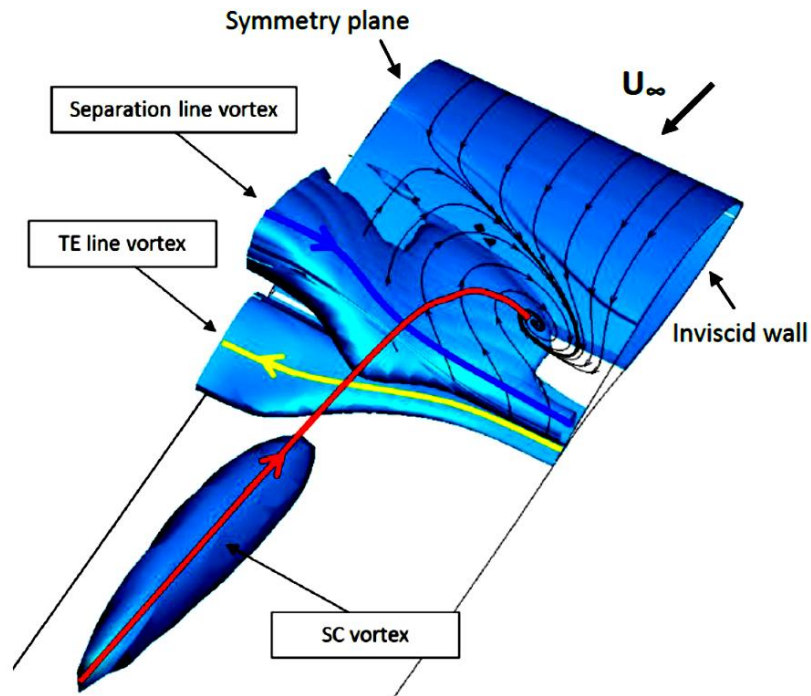
Figure 3. Vortex system associated with a stall cell as proposed by Manolesos [49]

A new stall cell formation mechanism was also proposed by Manolesos [49] as he believes that despite the role of Crow instability in bending the parallel vortex lines, no vortex rings would form due to this process. Instead, his proposed model suggests that perturbations generated due to the bending of the vortex lines lead to a 3-D separation front which in turn, induces pressure gradients and generates the streamwise vortex lines that are responsible for bending the shear layer and creating the stall cells. This process is illustrated in Figure 4.
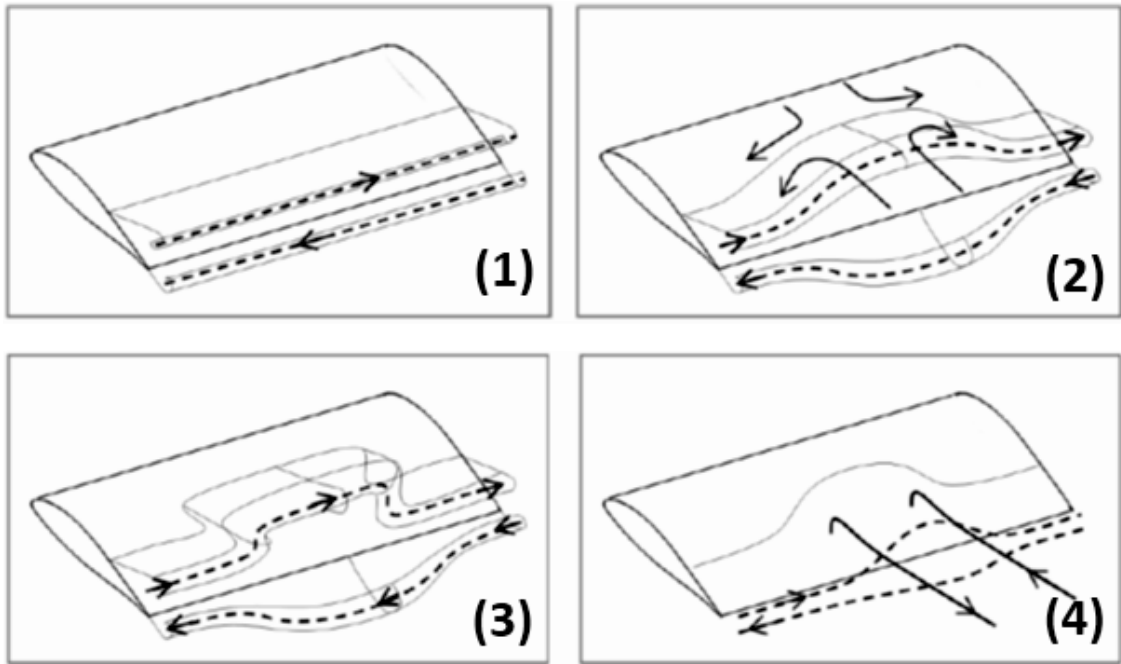
Figure 4. Stall cell emergence mechanism proposed by Manolesos [49]

More recently, De Mauro et al. [50] and Dell'Orso et al. [51] demonstrated the use of zig-zag tapes as 3-D disturbances for inducing stall cells in flow conditions in which stall cells did not appear naturally. Dell'Orso et al. [56] reported that the use of a 2-D step installed along the entire span did not result in the emergence of stall cells. In a later study, Dell'Orso et al. [51] demonstrated that zig-zag tapes can introduce 3-D features throughout their length by installing partial-span and full-span tapes and studying the cells that emerged due to the presence of the tapes. When using piezoelectric-driven partial-span steps, Dell'Orso et al .[56] observed that fully extending the step would nearly eliminate the stall cell that was present when the step was flush with the surface. The unsteady behavior of the flow field in the actuation period where flow alternates between a quasi-two-dimensional and a three-dimensional state suggests that alternate shedding and shear layer flapping, as reported by Driver et al. [57] might be playing a role. Manolesos and Voutsinals [49] also explored the use of zig-zag tapes in their work for a different purpose. They found that the use of a limited-span tape can eliminate the jostling motion of the stall cells, previously reported by Yon and Katz [46], and stabilize them for their stereo PIV experiments. While the exact mechanism of stall cell formation remains an open question, it is clear that the perturbation environment has a strong effect on the presence, nature, and dynamic behavior of stall cells.

In addition to investigating the effects of excitation frequency on the flow field, this work also seeks to explore the three-dimensional flow features on a thin, post-stall airfoil, and the potential control opportunities using instability excitation by NS-DBD actuation.

15

Development of 3-D features under excitation at various frequencies is studied using fluorescent surface oil flow visualization and stereo PIV. The data is then compared with streamwise planar PIV data. Ensemble-averaged, cross-stream PIV data were acquired to elucidate the general features of the flow field. To further investigate the perturbation characteristics which lead to stall cell formation, relatively low pulse repetition rate excitation signals are modulated with high-frequency carrier waves. The implications of the presented findings are discussed.

Chapter 3: Facilities and Experimental Techniques

3.1 Wind Tunnel

The experiments were conducted in a closed return, Gottingen-type wind tunnel of Gas Dynamics and Turbulence Laboratory at the Aerospace Research Center. The tunnel employs a 200 hp, variable speed AC induction fan to create the air flow. Than fan speed can be varied manually using a control panel or automatically by receiving a variable voltage DC signal from an NI BNC-2110 breakout box. The tunnel can operate in a fully automated mode via the use of a LabView code that enables the user to define a set of data points, i.e. various combinations of free-stream velocity and angle of attack, and acquire surface pressure or microphone data automatically. By adjusting the fan speed from 5 to a maximum of 90 Hz, the tunnel can produce a continuous range of flow velocities from $3 - 95$ m/s. The corresponding Reynolds numbers based on chord length $(Re = u_\infty c/\nu$ are $0.04 \times 10^6 - 1.20 \times 10^6$. The freestream turbulence intensity is on the order of 0.25% at fan speeds up to 40 Hz, corresponding to a chord-based Reynolds number of 0.78×10^6, and less than 1% at higher free-stream velocities.

17

The optically clear acrylic test section, measuring 61×61 cm in cross-section and 122 cm in length, at present can accommodate a series of custom-built composite airfoils with a chord of $c = 20.3$ cm that can be mounted in the center of the test section between two acrylic disks. The angle of attack, in the same fashion as the fan speed, can be adjusted either manually or automatically. To adjust the angle of attack manually, the disks can be rotated continuously, allowing for any angle of attack to be set accurately using a high-precision digital protractor. The automated mode of operation is preferred if a significant number of data points are to be acquired. In this mode, the angle of attack is set using a servo controlled by the tunnel's LabView code. A special pair of windows and rims, holding the airfoil, are connected to the servo via two belts. The servo angle is zeroed before the experiments using a high-precision digital protractor. The setup for automated angle of attack setting can be seen in Figure 5.

This setup was initially used to conduct angle of attack sweeps across the parameter space to characterize the baseline airfoil. However, it was discovered that due to servo jitter there is a 1-2° uncertainty in angle of attack measurements, which was deemed to be unacceptable, and thus all of the data were acquired in the manual mode where the angle of attack could be set with an uncertainty of about 0.05°.
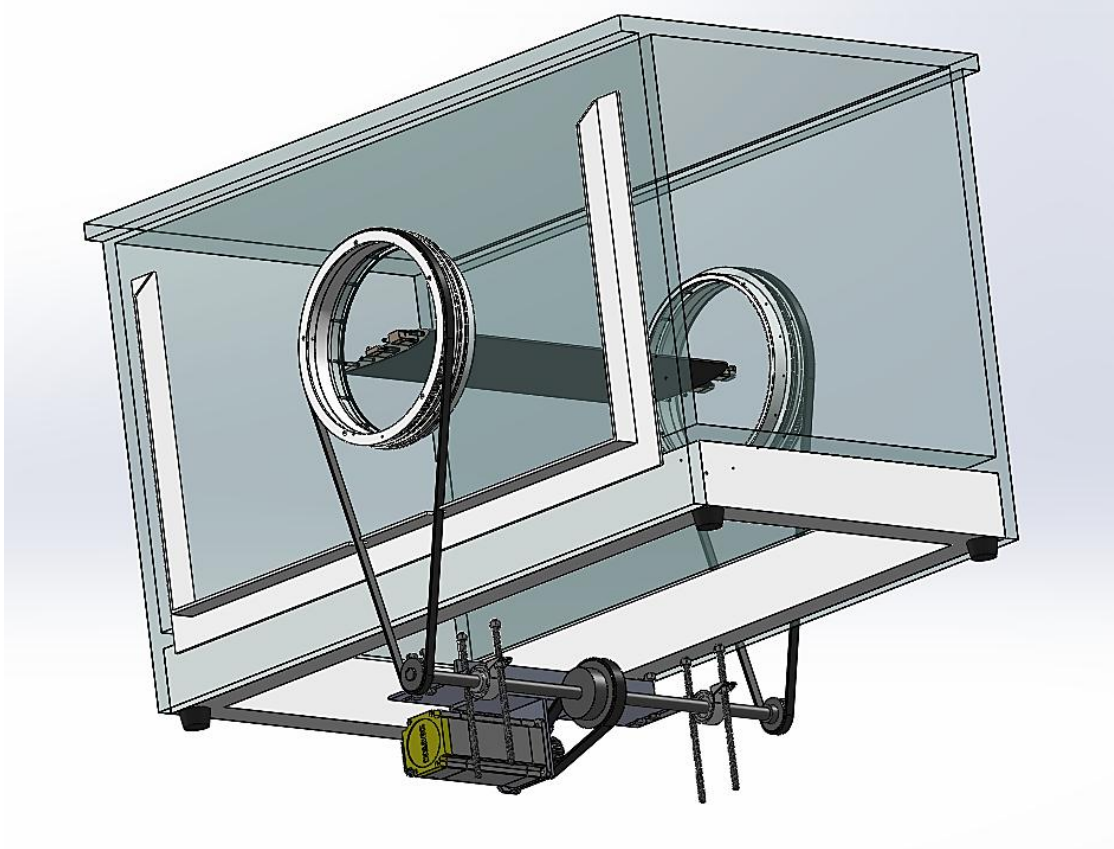
Figure 5. Driver mechanism for automated angle of attack adjustments

Freestream static pressure (p_∞) and stagnation pressure (p_o) are measured using piezometer rings consisting of four pressure taps. Located at the nozzle outlet and settling chamber, respectively, these pressure taps are connected to Omega pressure transducers (models PX655-25DI and PX655-5DI). The DC output signals from Omega DP-25 B-E readouts are then collected using a NI BNC-2110 breakout box and are converted to pressure and displayed using the tunnel's LabView code. Free stream velocity is calculated using the following form of the Bernoulli's Equation:

$$u_\infty = \sqrt{2k \frac{p_o - p_\infty}{\rho}} \qquad (3.1)$$

where $k = 1.05$ is the corrective factor and was empirically determined using a hot-wire anemometer. Ambient pressure data is recorded from METARs data reported by OSU Airport (KOSU) and is updated before each run. Freestream temperature is measured using a As is the case with all closed return facilities, special care must be taken to monitor and control the freestream temperature. This is accomplished by using a thermocouple and a commercial heat exchanger. The thermocouple located downstream of the test section close to the guiding vanes at the tunnel's 1st corner. This thermocouple is also used to obtain the ambient temperature prior to the startup of the tunnel. Experience has shown that the signal from the thermocouple is highly susceptible to EMI when the nanosecond pulser is operating. Since the automated tunnel control code relies on constant updates of tunnel conditions for feedback control of the freestream velocity, contamination of the temperature signal by EMI would lead cause the tunnel control code to crash. Therefore, it was decided to abandon the automated operation scheme and conduct the experiments while manually controlling the tunnel operation.

As mentioned before, heat management in a closed return facility is important and could turn into a challenging task specially when the ambient temperature rises in the hotter months of the year. The water-cooled heat exchanger, fed with the water taken from the cooling lines of the ARC compressors, is capable of maintain a relatively stable temperature (in the mid-70s during colder months) after the initial rise following the

20

tunnel startup. However, operating the tunnel for extended periods of time in the summer months would increase the freestream temperature to more than 100°F. This, in turn, affects the accuracy of the test Reynolds number calculated by the LabView code monitoring the tunnel operation so care must be taken to account for the temperature rise before interpreting the data taken in such conditions. A schematic of the tunnel along with the position of the pressure measurements and the location of the thermocouple can be seen in Figure 6.
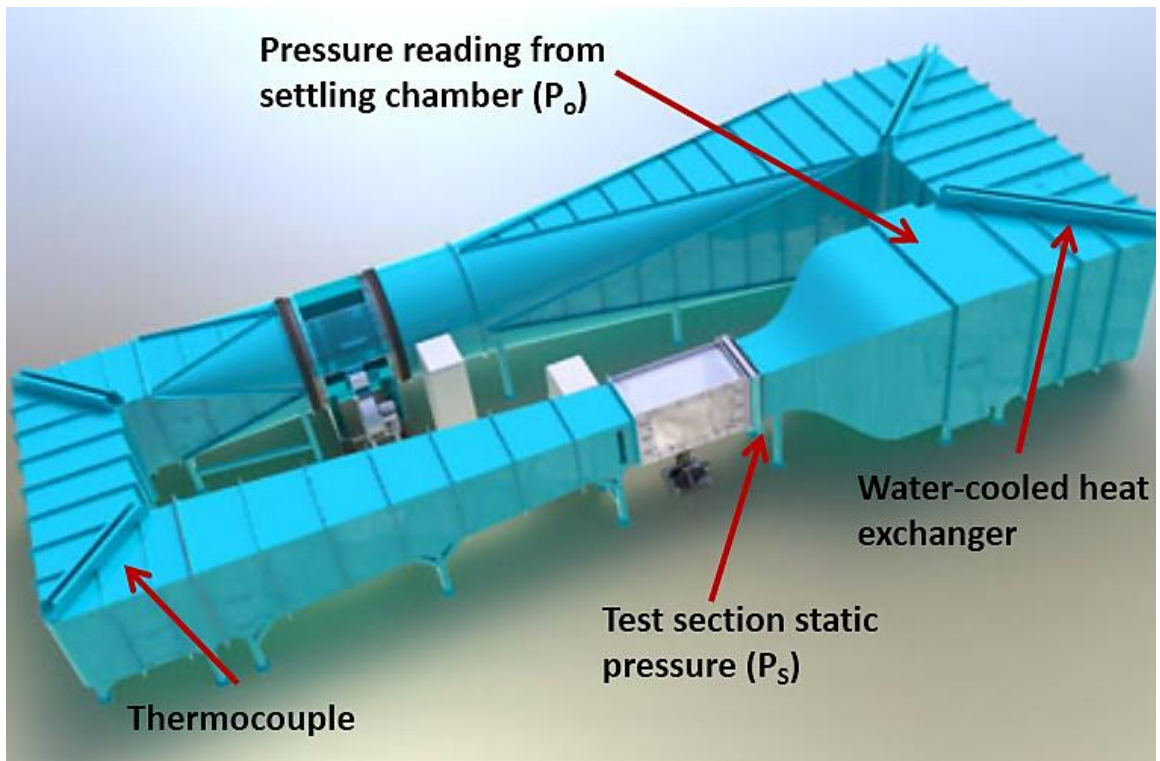
Figure 6. Schematic of the closed return, low-speed wind tunnel at GDTL
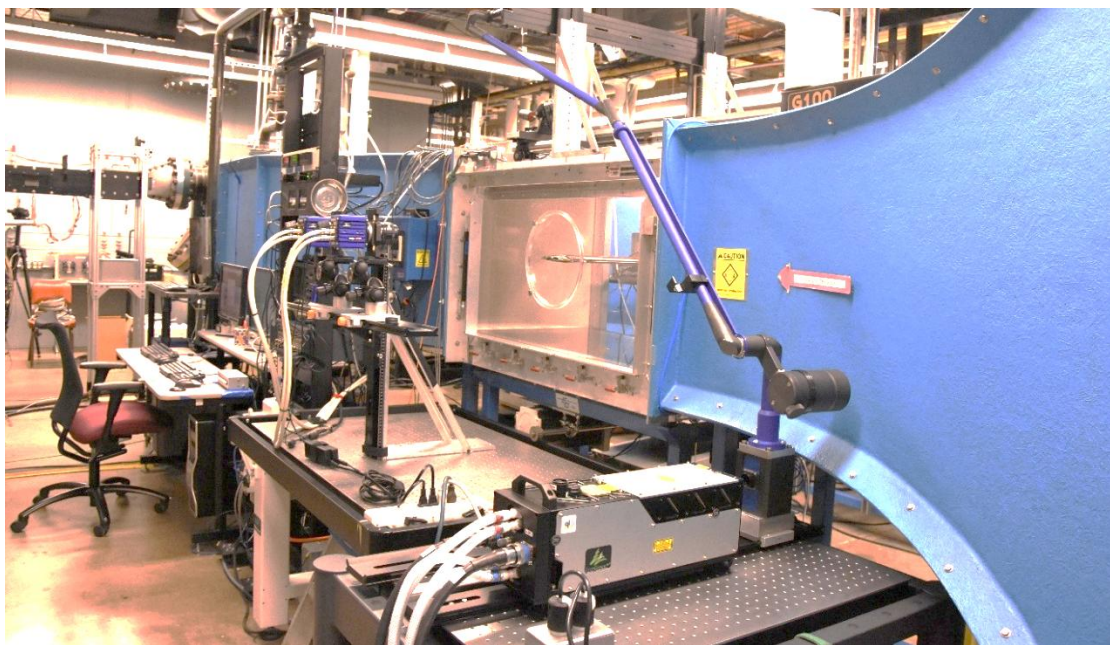
Figure 7. Data acquisition equipment setup for the low-speed tunnel

A two-axis traversing mechanism, manufactured by Velmex Inc., is used to traverse the microphone probe in the test section in the *xy* plane parallel to the free-stream flow. The traverse axes are driven by Velmex Inc., DC stepper motors which can position the probe with an accuracy of 0.1 mm. The traverse operation is automated using a dedicated LabView code which can be coupled to the tunnel control code. The traverse is "zeroed" by positioning the probe manually at a reference point. The traverse code would then take over by moving the probe to the specified coordinates. The stepper servo drivers, along with the pressure readouts, are installed on a rack next to the tunnel's control panel. The layout of the tunnel control station and the data acquisition equipment can be seen in Figure 7.

Two coordinate systems are used throughout this work. The first coordinate system has its origin fixed at the airfoil leading edge. The system is a two-dimensional grid aligned with the test section where streamwise and normal axes are normalized by the chord, denoted x/c and y/c and the spanwise axis is normalized by the span denoted by z/b. The second system is in the test section reference frame, with its origin at the trailing edge of the airfoil, and is used to present streamwise 2-D-2C and spanwise stereo PIV data. Here, normal and spanwise axes are normalized by the chord and span, respectively, and are denoted by y/c and z/b.

3.2 Airfoil and DBD Actuator

A Boeing Vertol VR-7 airfoil was chosen as the test model at the request of the sponsor agency (ARL) as it represents thin, cambered airfoils commonly used in rotorcraft blades. The maximum thickness of the airfoil is 10% of the chord at $x/c = 0.3$ The composite airfoil, painted black to minimize laser reflections from the surface, has a chord of $c = 20.3$ cm and is mounted in the center of the test section between two acrylic disks. The airfoil is equipped with a total of 35 static pressure taps, arranged in a staggered configuration slightly to the left of the centerline, and three high bandwidth 2.5 mm (~0.1 in) diameter Kulite pressure transducers (XCQ-080-25A) flush mounted near the centerline. Based on the previous experience, it was decided not to use the Kulite transducers as they are highly susceptible to EMI. Due to presence of the actuator close to leading edge where the

23

pressure taps are closely spaced, 3 taps are covered by the plasma actuator and therefore the MATLAB code used for processing the pressure data was modified to discard the data from those taps when plotting the surface pressure data. The distribution of the static pressure taps as well as the location of the covered taps can be seen in Figure 8.
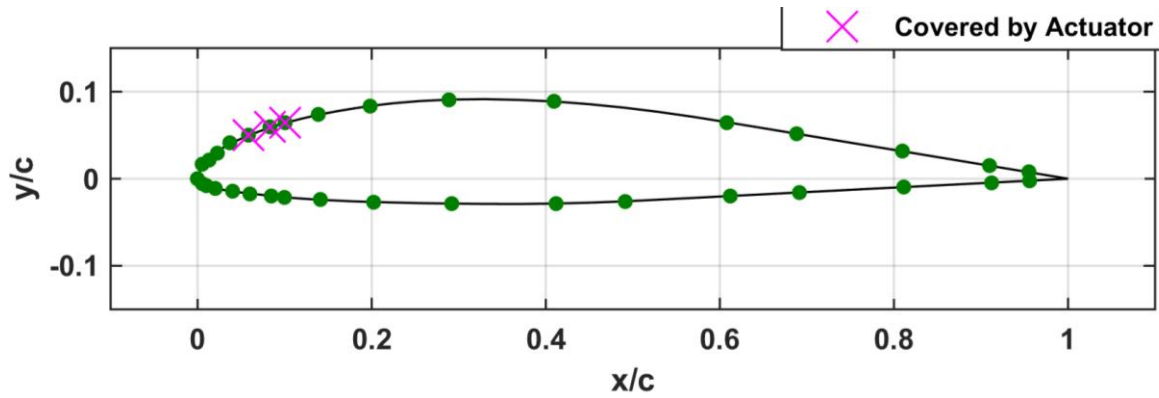
Figure 8. Distribution of static pressure taps over the airfoil

A single linear DBD actuator was placed on the airfoil to evaluate the efficacy of excitation. The actuator is constructed of two 0.09 mm thick copper tape electrodes; the exposed high-voltage electrode is 6.35 mm (0.25 in) wide and the covered ground electrode is 12.70 mm (0.50 in) wide. The dielectric layer is composed of three layers of Kapton tape, each 0.09 mm thick with a dielectric strength of 10 kV. The total thickness of the entire actuator is 0.45 mm. The actuator was placed on the suction side of the airfoil with the electrode junction at x/c=0.04. This location was just upstream of the separation location as determined by surface oil flow visualization. A schematic of the

24

airfoil demonstrating the location of the actuator and the reference coordinates can be seen in Figure 9.
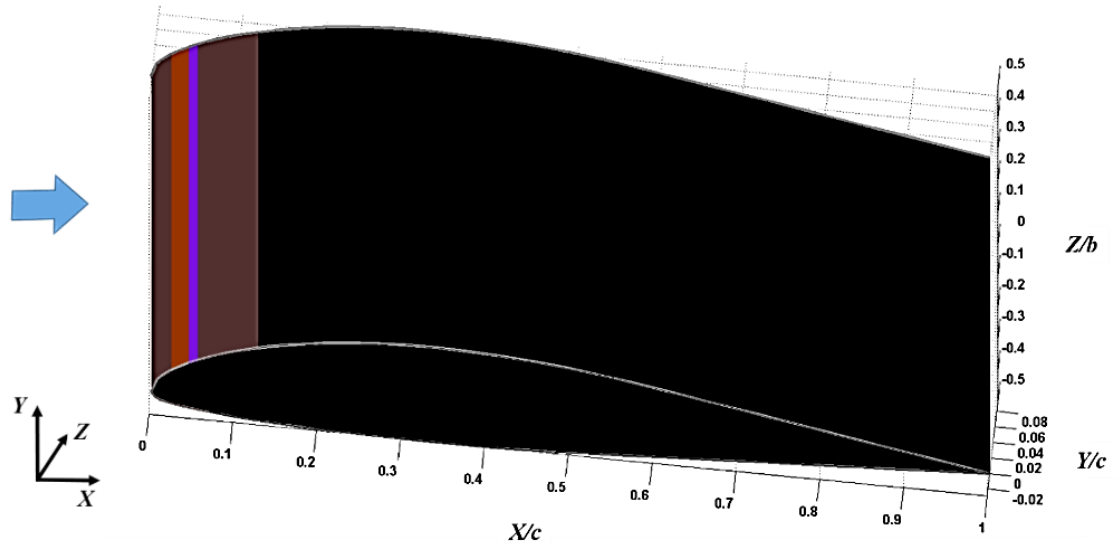
Figure 9. Schematic of the experimental arrangement demonstrating the chosen coordinate origin and actuator location

Since the presence of the relatively thick copper electrodes close to the leading edge was suspected to be affecting the accuracy of surface pressure distribution data, it was decided to fabricate the exposed and ground electrodes via circuit printing techniques to eliminate the intrusive exposed electrodes from the equation. This process is briefly described in the following paragraphs.

25

The first step in the process is to design the electrode and print the design over copper-clad Kapton sheets. A special class of printers using molten wax, instead of ink cartridges, is needed for this process. The molten wax is used to protect the copper layer on top of the Kapton sheet when the entire sheet is submerged into an acid solution. Samples of ground and exposed electrodes printed via this technique can be seen in Figure 10.
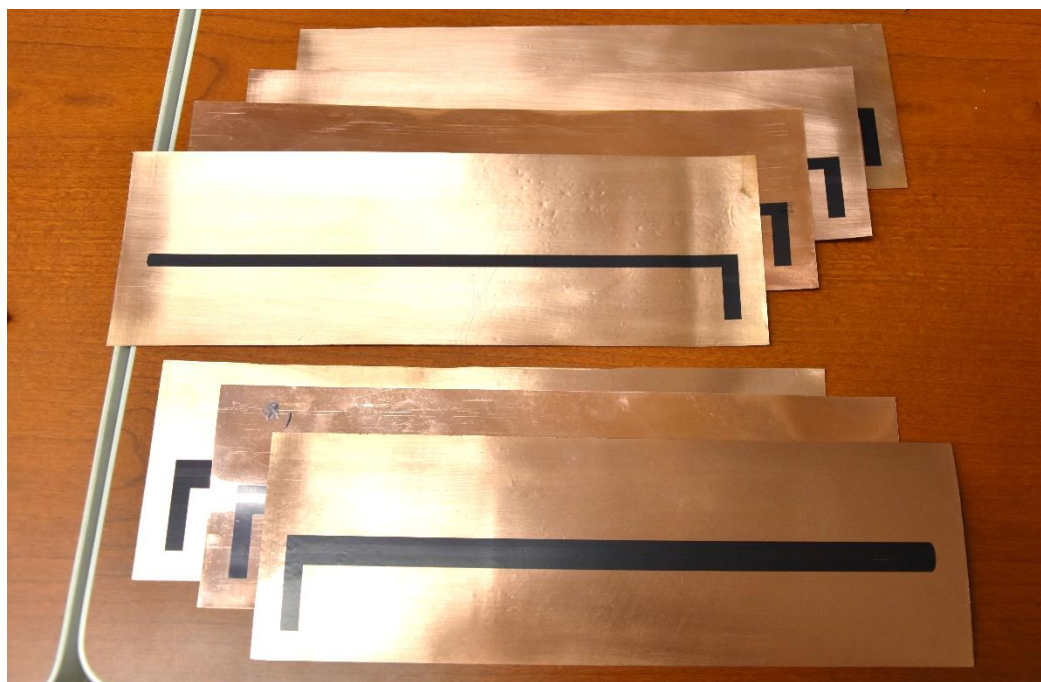
Figure 10. Samples of electrodes printed for use in the etching process

The printed electrodes are treated in the etching process where a strong etchant such a Ferric Chloride is used to dissolve the copper layer on top of the Kapton sheet. A commercial etching kit from MG Chemicals (model 416-ES) was used for this purpose. The kit consists of a tub, a fish tank pump (aerator), an electric heater and a thermometer.

The air pump is used for blowing air into the solution which would act as a catalyzer to expedite the etching solution. Depending on the solution temperature and the area of the electrode sheets, the process would take between 15 to 30 minutes to complete. It is necessary to check the electrodes regularly during the process to ensure that the wax protecting the copper has not dissolved due to exposure to the acid. A sample treated electrode after the process is shown in Figure 11. The acid residue on the electrode is the washed off with running water and the electrode surface is polished. Samples of finished ground and exposed electrodes can be seen in
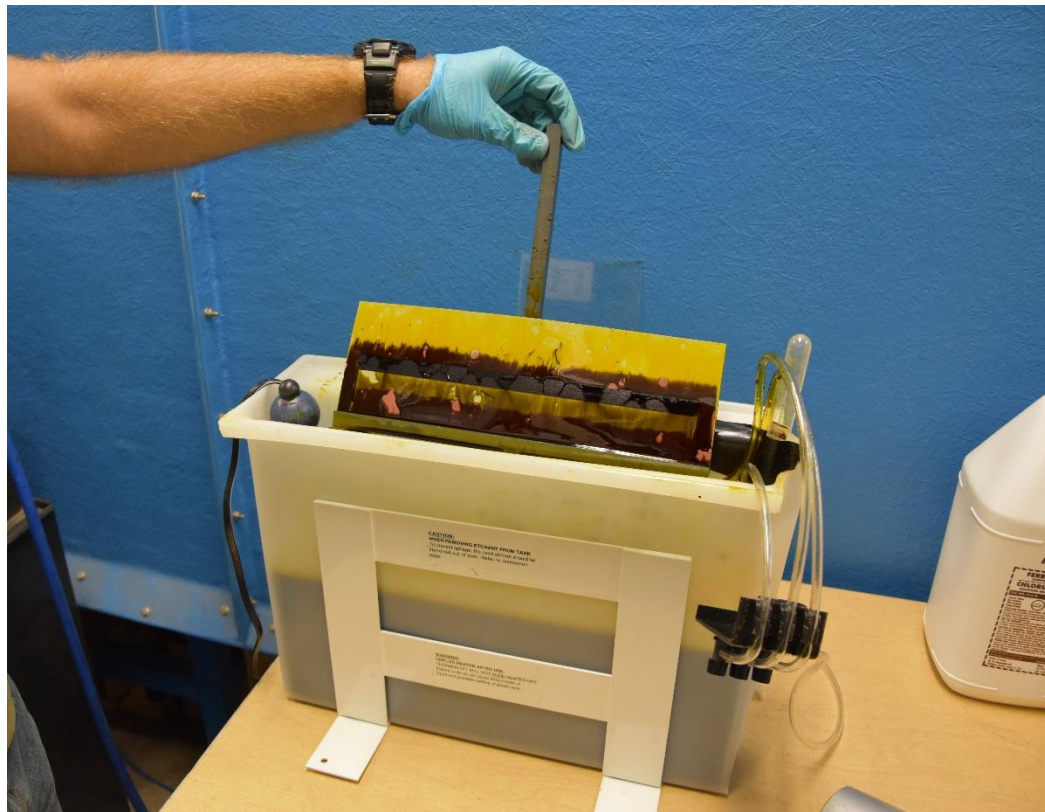
Figure 11. Removing the treated electrode from the acid tub
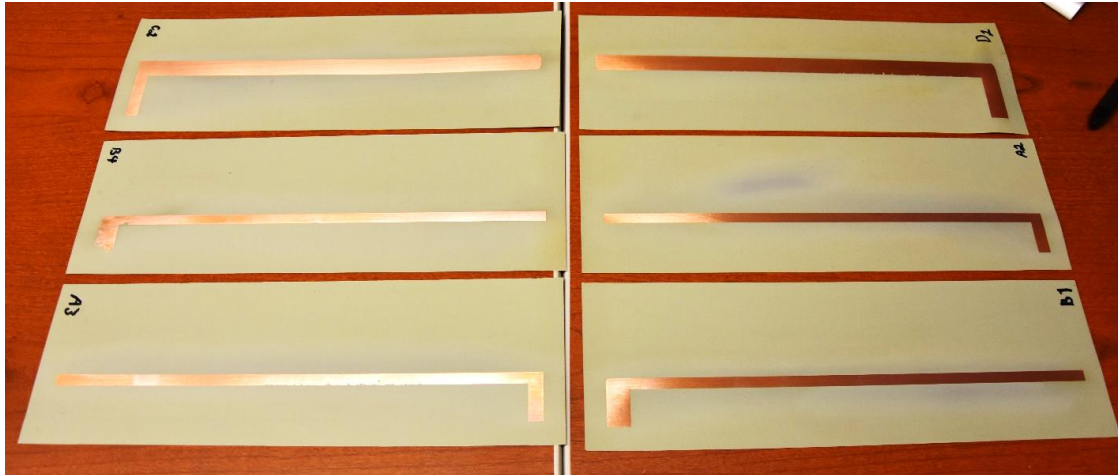
Figure 12. Electrodes fabricated with circuit board printing techniques

Finally, the electrodes are attached to the airfoil using double-sided tape. Since the Kapton used in the Copper clad sheets has twice the thickness of the Kapton tape normally used for fabricating the DBD electrodes, no additional dielectric layers are needed. The airfoil with PCB-printed electrodes installed in the leading-edge groove is shown in Figure 13.

Figure 13. Airfoil model with PCB-printed actuator

A series of experiments were conducted to ascertain the effects of using PCB-printed actuators on pressure distributions and lift and drag coefficient of the baseline airfoil. An angle of attack sweep between 0 and 20° for each actuator, i.e. hand-made vs. PCB-printed, was performed and 1500 samples of surface pressure data were acquired and averaged for each data point. As can be seen in Figure 14, the airfoil with the copper tape for the exposed electrode appears to performs better, i.e. has a higher lift coefficient and lower drag coefficient compared to the airfoil with PCB-printed electrodes. The unfortunate fact is that the actuator made with PCB-printed electrodes blocks 6 pressure taps close to the leading edge where the majority of the lift for this airfoil is generated. This is an artifact of the actuator construction where 4 electrodes, instead of 2, have to be used due to the limitations in the size of the sheet that the wax printer can accept. As a result, the lift coefficient of the airfoil equipped with such an actuator would always appear to be lower than that of the one with a hand-made actuator.

The loss of numerous pressure taps close to the leading-edge and associated inaccuracies in the pressure data was deemed unacceptable and therefore it was decided to conduct the experiments with the hand-made actuators. Nevertheless, this experience demonstrated that it is possible to fabricate high-quality, low-cost printed electrodes in-house with inexpensive equipment and if the limitations in the size of the printed sheet can be overcome, fabricating the actuators with printed electrodes would eliminate the supposedly intrusive copper electrodes of the earlier actuators.
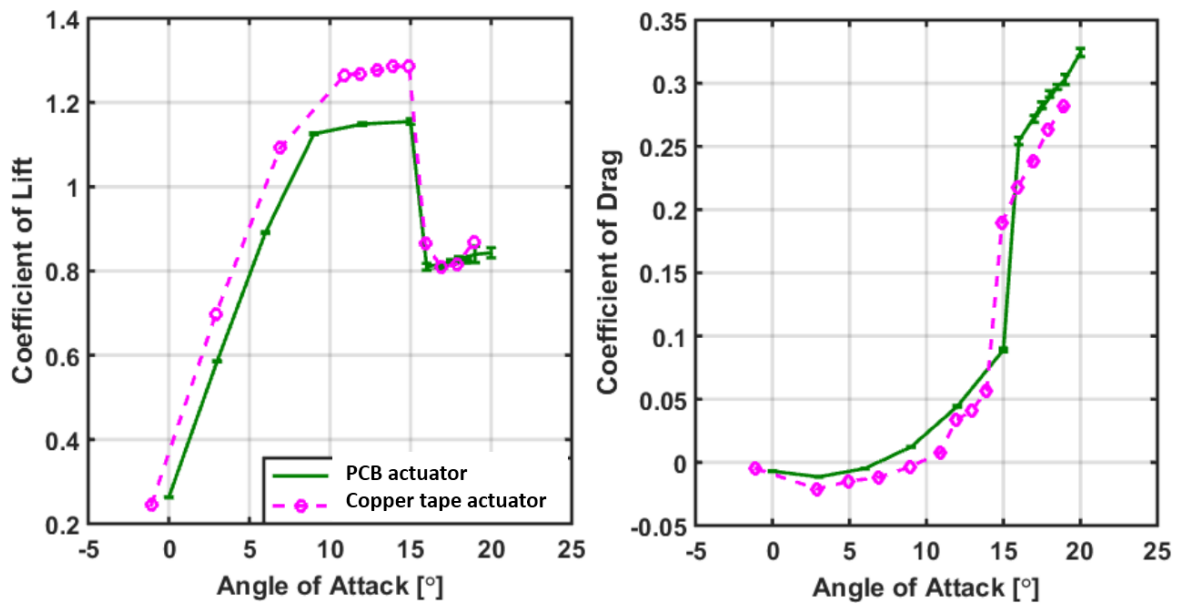
Figure 14. The effects of using a PCB-printed actuator and an actuator made with copper tape on lift and drag coefficients

3.3 Optical Diagnostic Techniques

3.3.1 Particle Image Velocimetry (PIV)

3.3.1.1 Planar Streamwise PIV

Particle image velocimetry (PIV) was the primary optical diagnostic technique in this work. PIV is a quantitative technique that enables the mapping of the velocity and vorticity fields via imaging the laser light reflections from the seed particles in the flow. Despite being very informative by providing vector maps of the flowfield, PIV, in practice, is a time-consuming technique and thus was used to further investigate a limited number of promising cases earmarked by other diagnostic techniques such as surface oil flow visualization and pressure measurements. Planar PIV data were acquired using widely expanded streamwise laser sheet along with a side by side camera configuration seen in Figure 15 which allowed a large flow field, including the suction side of the airfoil and the wake area, to be imaged. Ensemble-averaged maps of the normalized total velocity magnitude, $U^* = U/u_\infty$, normalized vorticity, $\omega^* = \nabla^* \times U^*$, and normalized Reynolds shear stress, $u'^* v'^*$, were extracted from the raw two-dimensional vector fields and were used to characterize the time-averaged flow field features. The seed particles were injected upstream of the test section through a nozzle array installed inside the settling chamber. Sub-micron seed particles were generated using a TSI 6-jet atomizer (model 9306A) which atomized extra virgin olive oil. The seed particles were illuminated using a Spectra Physics PIV-400

double-pulsed Nd:YAG laser with a 10 Hz pulse repetition rate. The maximum energy per pulse is 400 mJ and the pulse width is 10 ns. The laser beam is formed into a sheet with the use of a 1 m focal length spherical lens and two 25 mm focal length cylindrical lenses. The laser sheet has a thickness of ~2 mm and was located at 39.6% of the span of the airfoil from the far end of the acrylic test section. Several first-surface turning mirrors were used to direct the laser beam, over a long beam path of about 6 m unto the sheet-forming optics. The laser beam path can be seen in Figure 16.
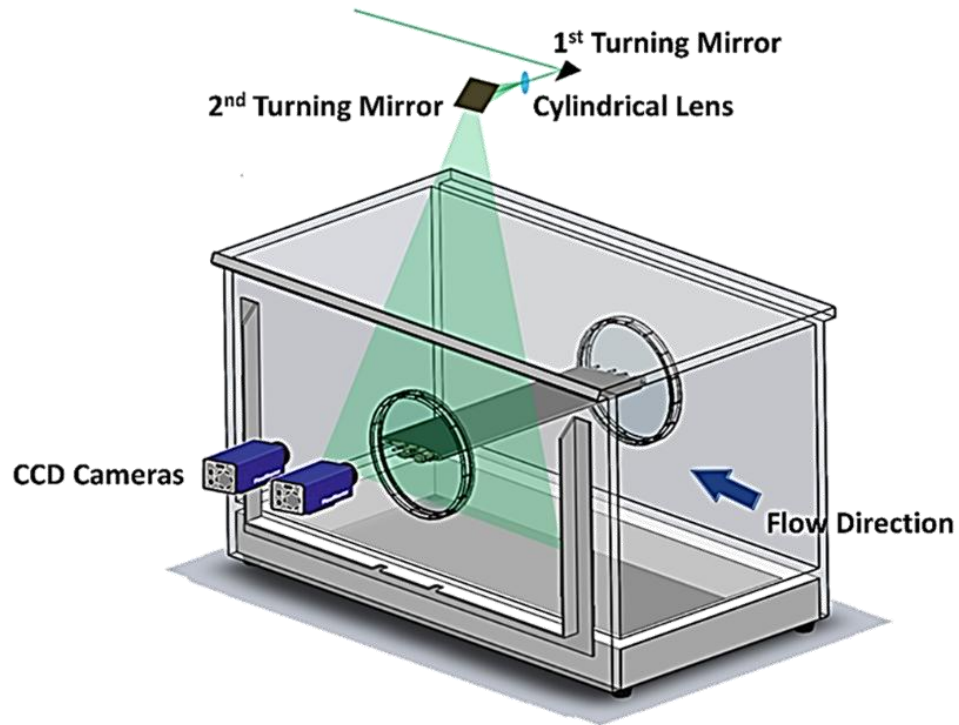
Figure 15. Schematic of the dual-camera streamwise 2-D-2C PIV setup
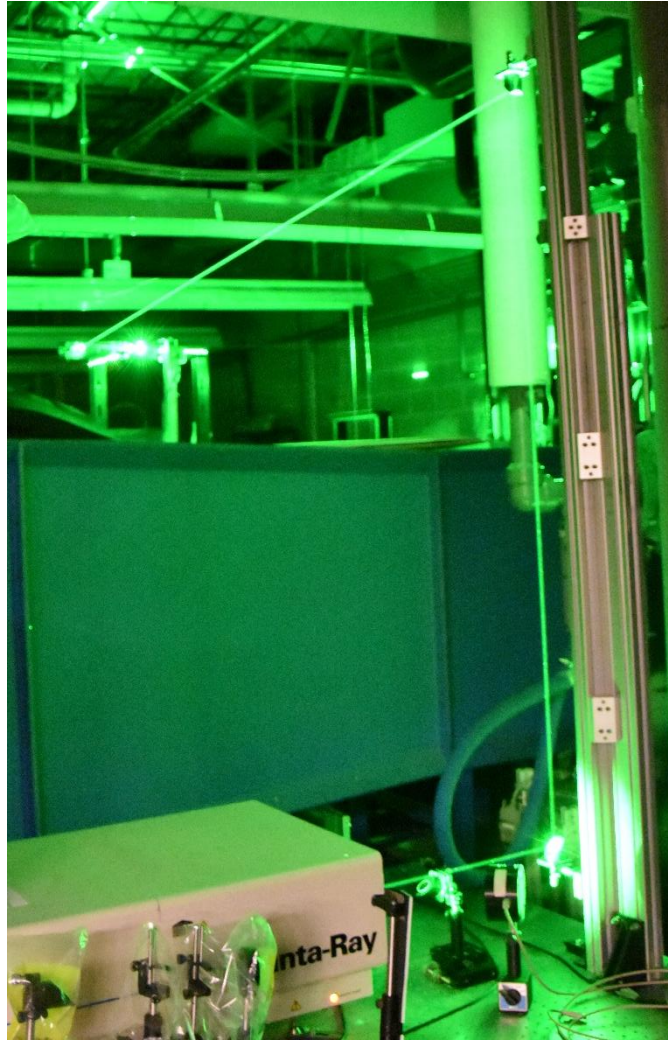
Figure 16. Laser beam path for the planar streamwise setup

The long beam path of the setup used in the experiments makes it particularly susceptible to minor misalignment of the laser heads or optics. On several occasions, it was noticed that the particles would "drop out" or disappear when comparing the shots in an image pair. This issue can be addressed by ensuring that the laser pulses from the two heads are aligned with each other. This can be done by inspecting the particle movements in image

pairs while simultaneously adjusting the optics or the laser heads. Laser alignment paper can also be used to trace the beam path and ensure alignment.

To acquire data over the airfoil and in the wake region, a two-camera setup (shown in Figure 15) comprised of two LaVision 12-bit 2048×2048 px Imager Pro camera bodies, each with a Nikon Nikkor 35 mm f/1.2 lens was employed. While the use of short focal length lenses allows for a larger field of view to be imaged, it also introduces perspective distortion effects. These effects become more pronounced when images acquired by the camera pair are stitched together. A particular feature, which could not be easily eliminated with this choice of lenses is the arc, seen in samples of streamwise PIV data such as Figure 17, which is introduced by the edge of the Acrylic disks holding the airfoil in place. Since this distortion is present in the velocity vector fields, it would also appear on all the velocity-derived vector fields, such as vorticity as well.
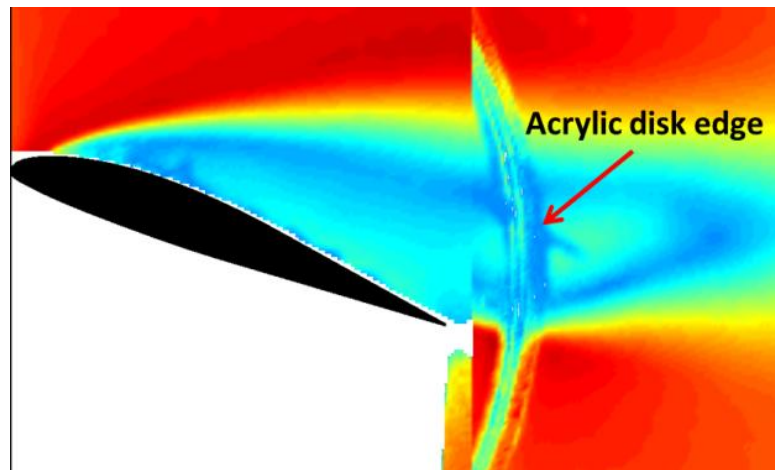
Figure 17. Sample of streamwise PIV data depicting the distortions introduced by the Acrylic disks

34

The cameras were positioned 253 mm center to center on a horizontal optical rail and the camera lenses were located ~980 mm away from the laser sheet. The cameras acquired data simultaneously at an average acquisition rate of 3.3 Hz. For excited cases, five sets of 100 image pairs were taken for a given case, whereas for the baseline data, a single set of 1000 images were taken. A limited series of experiments aimed at characterizing coherent structures over the airfoil were carried out using a one-camera setup. This choice was dictated by the need for a higher spatial resolution to detect the small-scale structures that would be generated due to high-frequency excitation of the flow. As such, it was decided to dedicate the entire CCD sensor area to imaging the suction side of the airfoil. A 14-bit La Vision Imager Pro X 4M camera with a 50 mm lens was employed for this purpose. Two sets of 250 image pairs per data point were acquired at an average rate of 5 Hz with this camera. Although both PIV setups described above were observed to be susceptible to EMI especially at higher actuator pulser repetition rates (> 1000 Hz), the 14-bit camera setup proved to more resilient when its trigger signal was contaminated with spurious EMI-originated pulses. The laser trigger signal, in both setups, was also contaminated by EMI-related noise despite the use of heavily shielded cables. It was also found that the programmable trigger unit (PTU) installed on the data acquisition computer's motherboard, would send out spurious trigger pulses whenever it was close to the nanosecond pulse generator. Positioning the DAQ computer as far away from the pulse generator and the actuator was found to be the best possible solution.

The cameras in the two-camera setup were calibrated simultaneously using LaVision's Davis 7.2 software. The first step in the calibration process is to accurately position and align the 3-D calibration target with the laser sheet. Having acquired images of the calibration target using both cameras, the user is then prompted to select three points on the calibration target that would serve as reference coordinates. Then the software would attempt to identify the circular dots printed on the calibration target using an edge detection algorithm and would compare their spacing in the image, which could be affected by a variety of factors such as optical distortions, with the specifications of the calibration target stored in the software's libraries. The root mean square (RMS) of the deviations should be less than 1 px. Values less than 0.5 are considered to be excellent according to Davis' manual. The calibration setup for the streamwise planar PIV experiments can be seen in Figure 18.
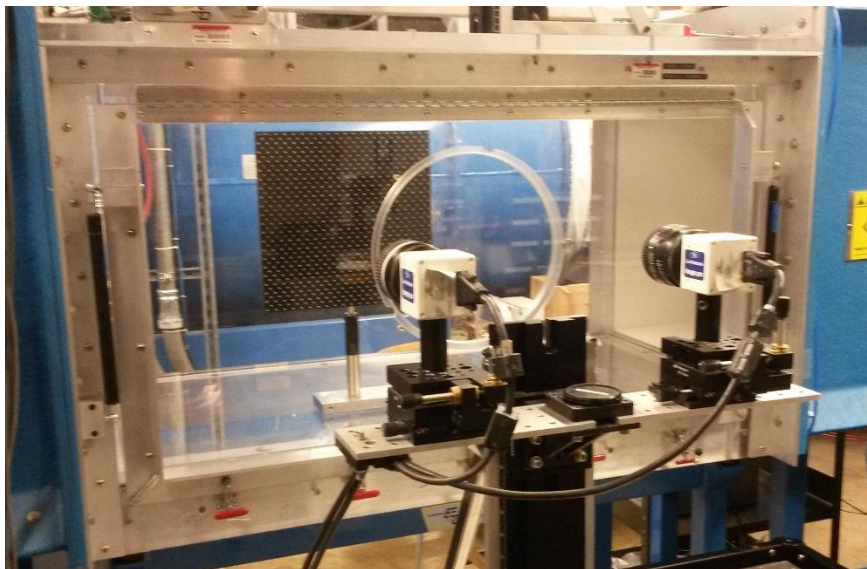
Figure 18. Two-camera system calibration setup

36

All of the planar streamwise data were processed using LaVision's DaVis 7.2 software. The data were further post-processed in DaVis and then averaged, normalized and plotted using an in-house MATLAB code. For each image pair, a multi-pass cross correlation was used. The first window size used was 64×64 px with a 50% overlap, followed by two 32×32 px windows with a 75% overlap. The final pass was performed using a B-spline-6 reconstruction. The velocity fields were then post-processed to remove spurious vectors using a correlation peak ratio criterion, allowable vector range, and median filter based on nearest neighbor. The resulting velocity field was then smoothed using a 3x3 px Gaussian smoothing filter. Afterward, the images from each camera were stitched together and averaged. Full scale error was computed using

$$\epsilon_{vel} = \frac{\epsilon_{cp}}{S \, dt}$$

where ϵ_{vel} is the full-scale error [m/s], ϵ_{cp} is the correlation peak estimation error [px], S is the scaling factor [px/m], and dt is the laser pulse separation [s]. The laser timing error was assumed to be negligible and ϵ_{cp} was taken to be 0.1 px [59]. This corresponds to an error in instantaneous velocity of 0.74 m/s (or 2% of the freestream velocity).

Three forms of PIV data were acquired – ensemble averaged, actuator phase locked, and pressure phase locked. Ensemble averaging of the instantaneous images provides a view of the time-averaged flow near the airfoil and in its wake while the forcing mechanism can be explored using phase-locked PIV. Instantaneous images were captured similar to baseline PIV, but were synchronized with specific phases throughout the forcing period

37

and then phase-averaged. The phases considered here were 0°, 30°, 60°, 90°, 120°, 150°, 180°, 210°, 240°, 270°, 300°, and 330°. The delay between the trigger signal and plasma formation was accounted for so that plasma formation occurred at 0°. Swirling strength was used as the vortex identification technique, detailed by Adrian et al. [60], and was non-dimensionalized to Strouhal number as described above.

An alternate phase locking method that synchronized the camera and laser triggering with shedding of vortical structures, rather than plasma formation, was also employed. A Brüel and Kjær model 4939 microphone and a Nexus 2690 signal conditioner were used, in conjunction with an in-house LabView code to provide a trigger signal based on vortex shedding events. The code acquires pressure data, applies a first-order Butterworth band-pass filter about the shedding frequency, and outputs a square-wave trigger on a rising edge. A conditional averaging based on covariance was used in post-processing to filter out spurious trigger events. This method allows a phase-locked baseline to be acquired. Acquiring phase-locked data, in general, was found to be more challenging due to spurious triggering by EMI-induced peaks in the trigger signal.

As was mentioned earlier, the streamwise laser sheet for planar PIV experiments was located at approximately 40% of span or z/b = -0.1. Due to the presence of a slot on the test section ceiling, used for traversing probes in the streamwise direction, the laser sheet could not be located exactly at mid-span. The discrepancy between the data acquired at this spanwise location and the surface pressure data acquired at approximately $z/b = 0.1$ gave rise to the suspicion that three dimensional features might be present in the flow

field and led to the discovery that stall cells were present on the suction side of the airfoil when the flow was perturbed at mid to high frequencies. The location of laser sheet relative to the airfoil in the chosen coordinate system is depicted in Figure 19.
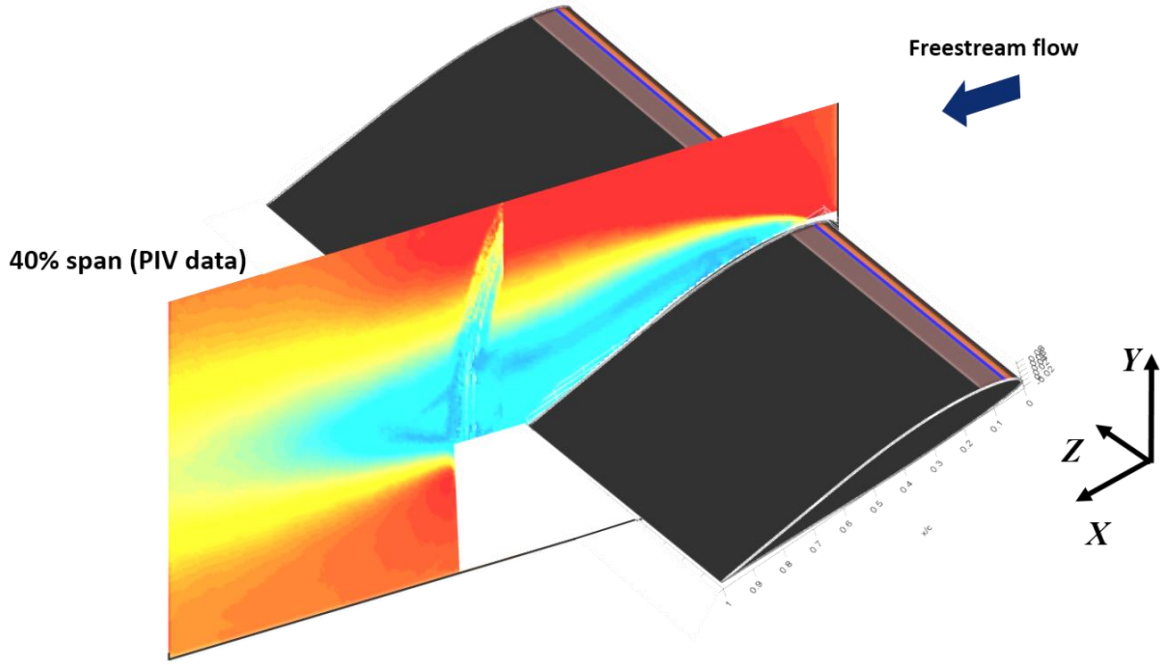
Figure 19. Sample of streamwise planar data

As mentioned earlier, various vector fields were extracted from the raw velocity distribution maps obtained by DaVis. Non-dimensional swirling strength, $\gamma_{ci}^* = \gamma_{ci}c'/u_\infty$, was used as the vortex identification technique. Unlike vorticity, which identifies both rotation and shear, swirling strength negates shear and highlights only rotation. This is a critical point method using the local velocity gradient tensor and its

eigenvalues, as detailed by Adrian et al. [46]. Although only two components of velocity were available (u and v), a three-dimensional tensor was utilized assuming incompressibility in the spanwise direction. Swirling strength is quantified by the largest imaginary component of the eigenvalues of the three-dimensional velocity tensor. The tensor was calculated using a second-order accurate central divergence scheme and the eigenvalues were found using MATLABs built-in `eig()` command. Samples of distribution maps derived from the raw velocity vector fields of DaVis using an in-house MATLAB code developed by Clifford [61] are shown in Figure 20.
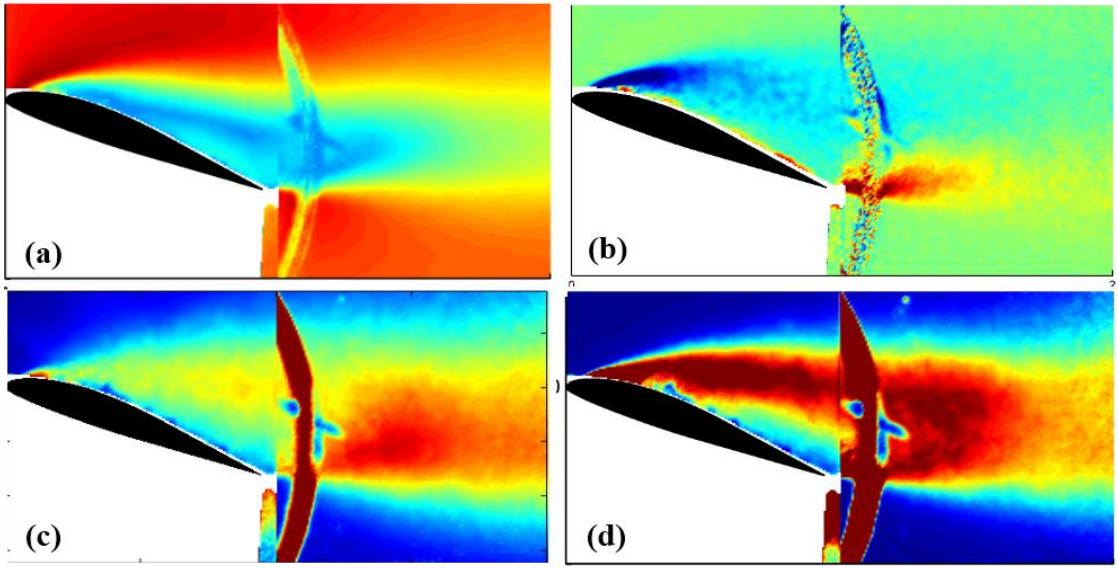
Figure 20. Samples of data extracted from the acquired planar velocity fields (a) total velocity distribution, U^* (b) vorticity distribution, $\boldsymbol{\omega}^*$ (c) v_{rms} distribution (d) Reynolds shear stress distribution, $\boldsymbol{u'^*v'^*}$

3.3.1.2 Spanwise Stereo PIV

A stereo cross stream PIV setup, depicted in Figure 21, was employed to investigate flow non-uniformities due to the presence of 3-D features in the spanwise direction. The stereo PIV setup was comprised of two 5.5 million pixel, 16 bit LaVision Imager sCMOS cameras. Each camera was fitted with a 24 mm, wide-angle Nikon Nikkor f/2.8 lens in order to maximize the field of view. Approximately 89% of the airfoil span was imaged with this setup. The angle between the camera sensor normal vector and the tunnel centerline was approximately 37°. One set of 600 image pairs was acquired at a rate of 10.5 Hz for each data point. Ensemble-averaged and actuator-phase-locked data at various excitation frequencies were acquired to characterize the flow field.
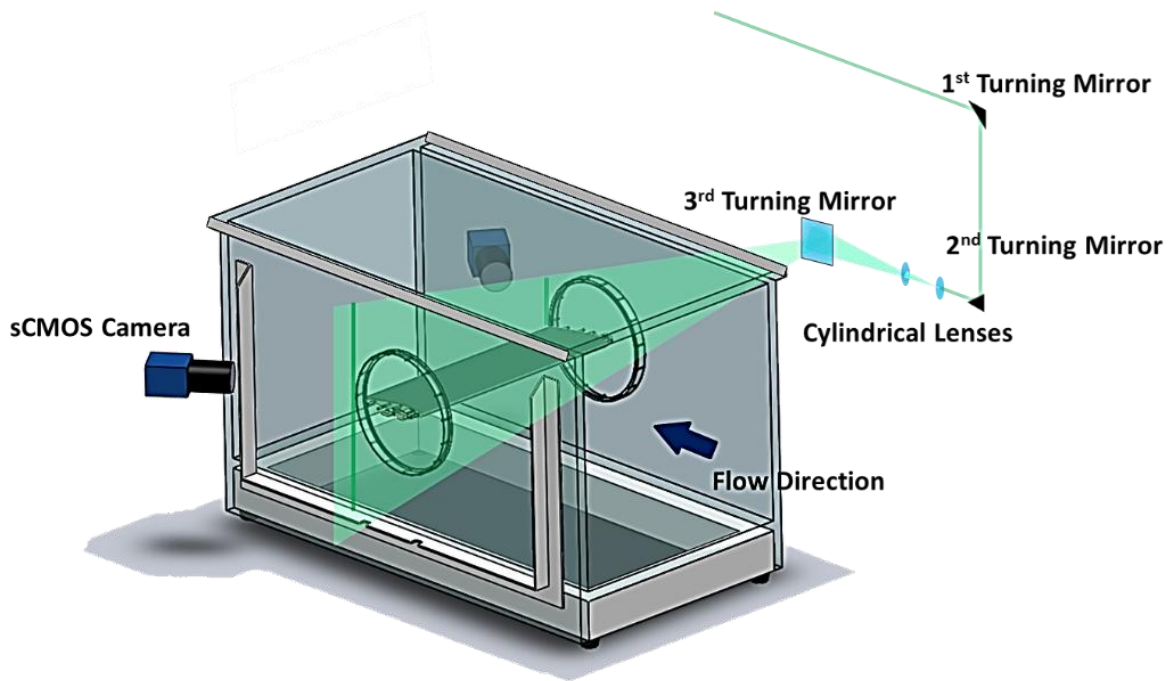
Figure 21. Schematic of spanwise stereo PIV setup

Two 25-cm focal length cylindrical lenses along with three first-surface turning mirrors (seen in Figure 21) were used to form a laser sheet. The spherical focusing lens was discarded to avoid thinning the laser shit. It is known that having the thicker laser sheet would reduce the errors in calculating the out-of-plane component of velocity[59]. The laser sheet in this setup was approximately 7 mm.

The stereo setup shown in Figure 21 is referred to as forward, backward scatter setup in the literature[62] as the intensity of Mie scattering in the direction of the incident light (forward scatter) is much higher than the opposite direction (backward scatter). Due to the space or optical access limitations it was not possible to position the cameras so that both could collect the scattered light in the forward scatter mode. This proved to be significant challenge as the 12-bit CCD cameras initially used in this setup were unable to register enough scattered light in the backward scatter for the cross-correlation algorithm to calculate the velocity vectors. Thus, it was decided to use the highly sensitive 16-bit sCMOS cameras from LaVision in this setup. The intensity of the scattered light can be marginally increased, to facilitate the detection of particles by the cross-correlation algorithm, by increasing the laser power to about 320 mJ/pulse (80%) and increasing the seeding in the tunnel by simultaneously raising the seeder's air supply pressure (up to 11 psi) and employing more atomizer jets (up to 6).

The light scattered from the seed particles in the above conditions can be seen in the images acquired by the sCMOS cameras (Figure 22) and a color CMOS camera (Figure 23).
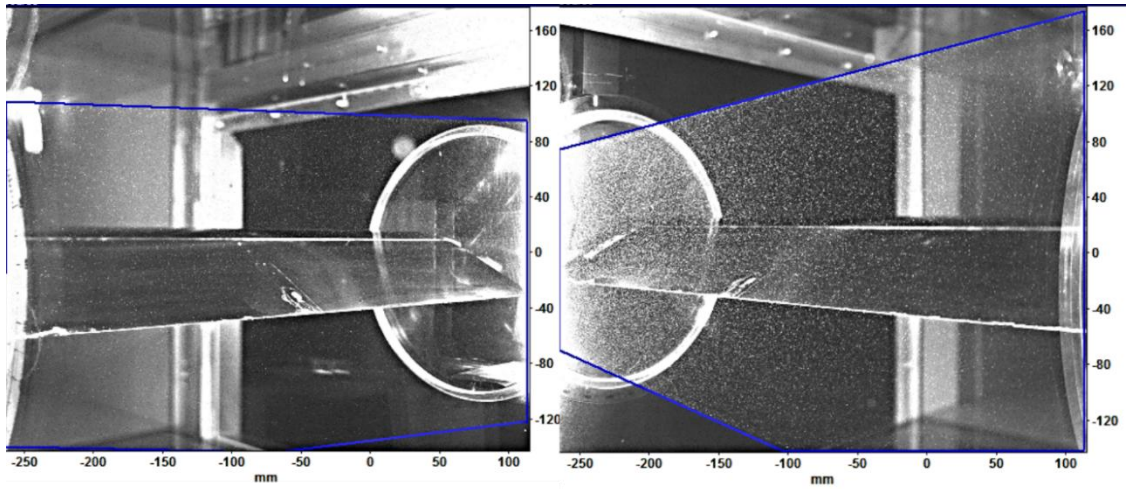
Figure 22. Difference between the scattered laser light in forward and backward scatter

modes
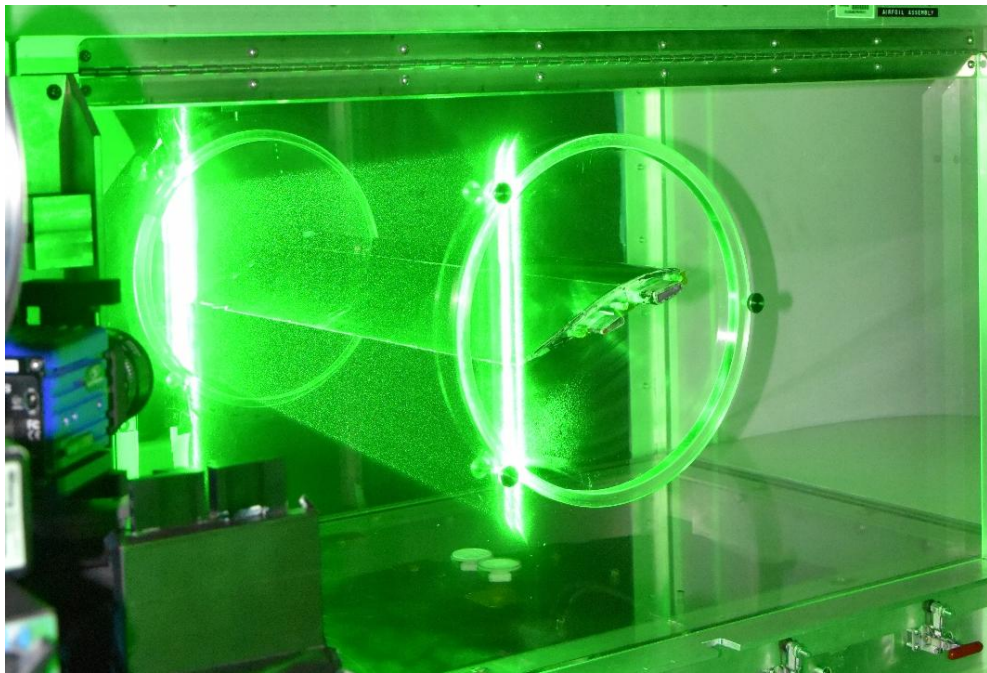
Figure 23. Maximum light scattering from the laser sheet in the forward scatter mode

Once it became clear that the use of 14-bit cameras along with increased laser power and seed density would give the desired results, the cameras in the setup were calibrated. The stereo calibration wizard in LaVision's DaVis 8.3 was used for this purpose. As with the streamwise planar setup, the surface of the 3-D calibration target was carefully aligned with the laser sheet which was positioned 0.5% of the chord downstream of the trailing edge similar to a setup used by Manolesos[49] to study stall cells. The center of the calibration target in each image (see Figure 24) was chosen as the reference point. Samples of calibration images where white circular dots of the target plate are identified by DaVis (marked by green dots) can be seen in Figure 24.
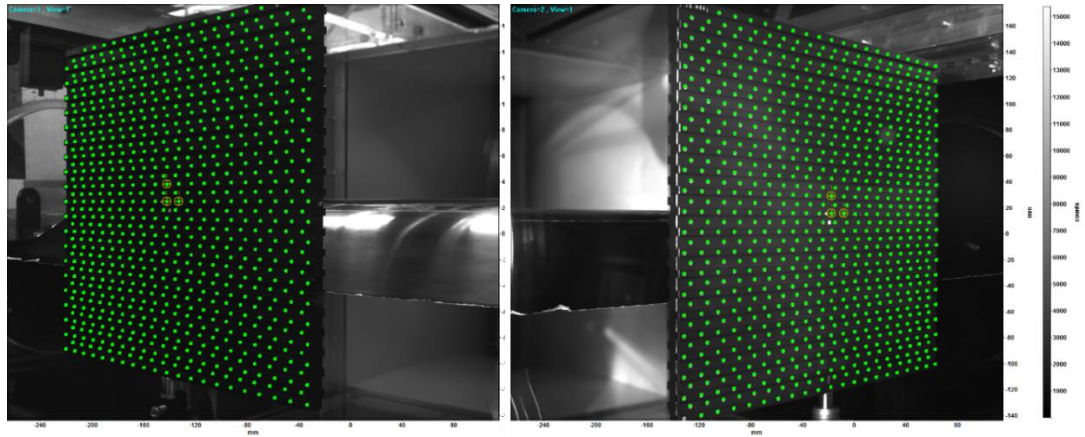
Figure 24. Calibration images of the target plate acquired by camera 1 (right) and 2 (left)

A multi-pass, decreasing window size vector calculation algorithm was used with 2 passes of 64×64 px windows with 50% overlap and 2 passes with 32×32 px windows having the same overlap as before. The vector fields where post-processed using median

filters. A sample velocity vector field, calculated by DaVis along with a corrected image from the calibration wizard are shown Figure 25.
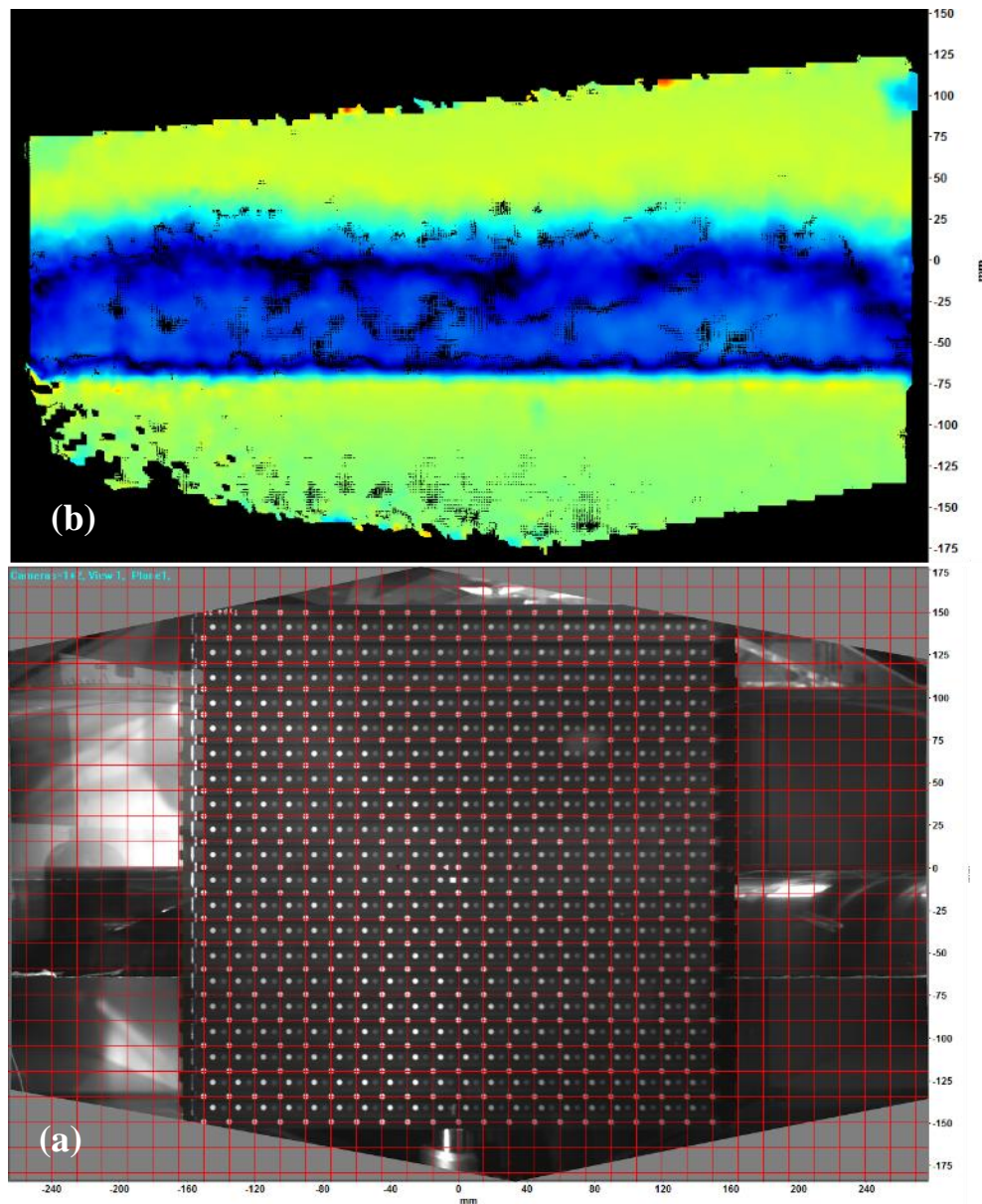
Figure 25. (a) Corrected calibration image (b) post-processed velocity field from DaVis

45

A different coordinate system, fixed the trailing edge, was used to present the spanwise stereo data. The location of the laser sheet plane relative to the airfoil in the chosen coordinate system is depicted in Figure 26.
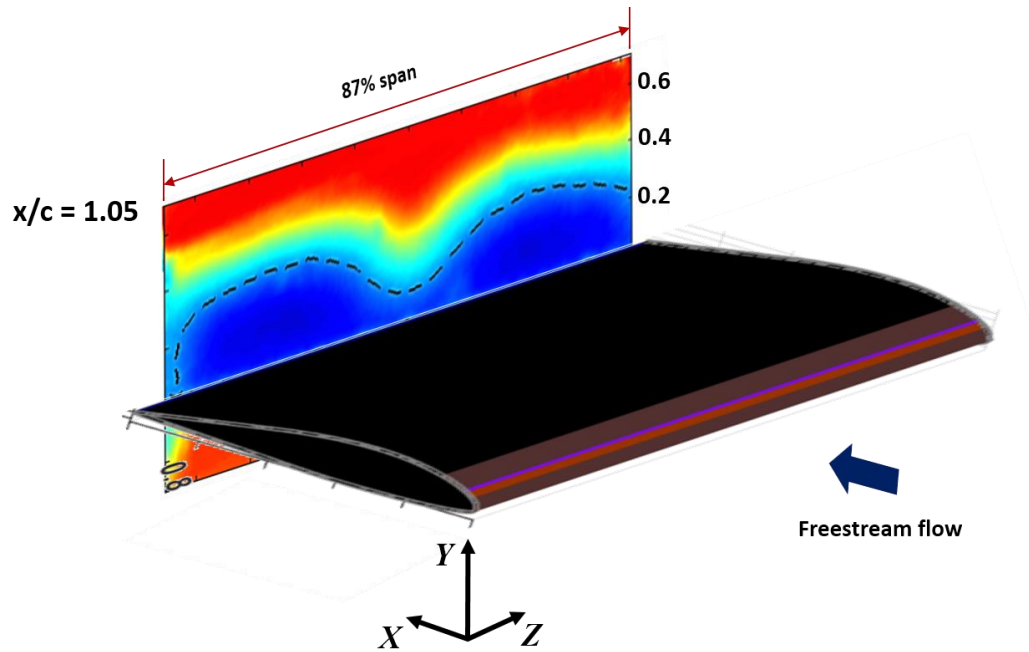
Figure 26. Sample spanwise stereo PIV velocity field superimposed on the airfoil

As before, the velocity vector fields calculated with DaVis were imported for averaging, extracting additional data and data visualization in MATLAB. The existing MATLAB code used for processing the planar PIV data was modified to account for the additional velocity component (out of plane) present in the data. Samples of the data derived from the three-component velocity vector fields are plotted in Figure 27.
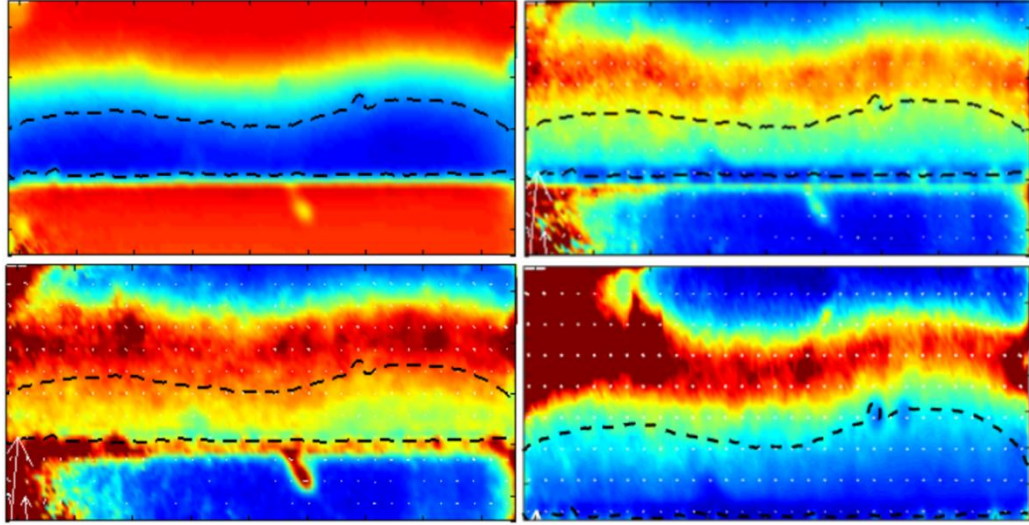
Figure 27. Samples of data extracted from 2-D-3C velocity fields (a) normalized streamwise velocity, $\boldsymbol{u'^*}$ (b) normal velocity, $\boldsymbol{v'^*}$ (c) root mean square of spanwise velocity fluctuations, w' (d) normal shear stress

3.3.2   Pressure Sensitive Paint

The paint used in this work is BUNC-12, which was provided by ISSI. BUNC-12 is a dual luminophore binary paint that is packed in aerosol form for ease of application. The paint emits a reference signal at 525 nm and a pressure signal at 650 nm. This signal can be acquired using a color camera with a filter wheel or a scientific color camera with a Bayer filter applied to the sensor. Acquiring the reference and pressure signals, allows the user to calculate the ratio of ratios and thus correct for temperature and model deformation effects resulting in more accurate data. Due to the lack equipment needed to

conduct binary PSP measurements, the paint was used as a single luminophore paint by employing a 620 nm high pass optical filter.

According to the manufacturer, this paint is ideally suited for measurements in isothermal environments (e.g. large metal models and temperature controlled tunnels) or where strong pressure gradients are present. The pressure sensitivity of the paint is 0.5% per kPa whereas its temperature sensitivity is 1.5% per °C. As such, this paint would not be an ideal choice for conducting experiments in low Reynolds flows or where temperature variations on the model surface are present. Another important attribute of this paint is its relatively fast photo degradation rate, being 1% per hour. Special care was taken to cover the model after the experiments to prevent paint exposure to light. This paint has nearly linear calibration curves at various temperatures as can be seen in Figure 28a. The excitation and emission wavelengths of the paints can also be seen in Figure 28.
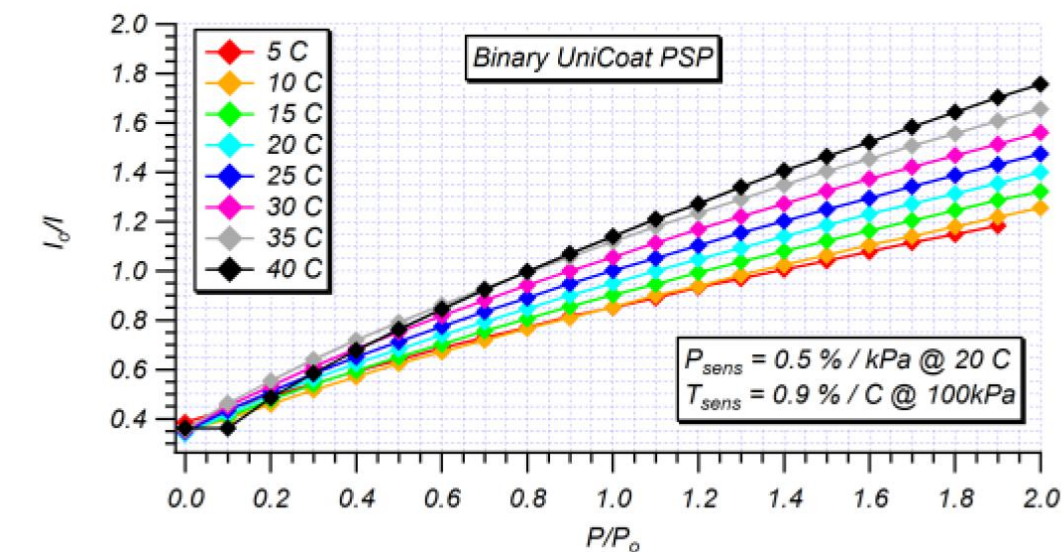
(a)
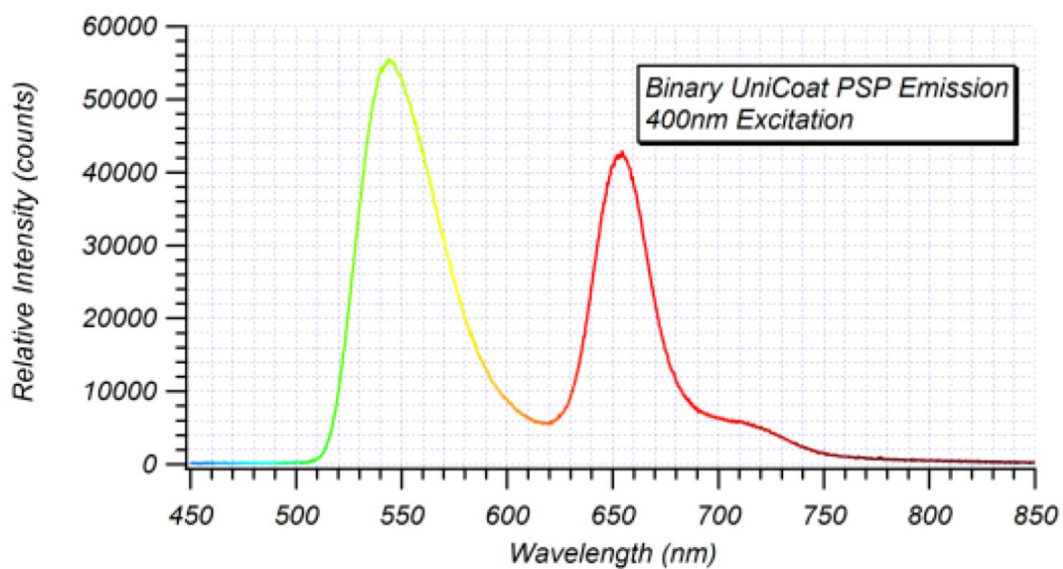
(b)

Figure 28. a) BUNC-12 binary paint calibration curves b) Emission and excitation

wavelengths of the paint

As mentioned previously, the BUNC-12 paint used in this project is provided in an aerosol can by ISSI. Since the paint is toxic, it was applied under a ventilation hood, and masks were put on for extra safety. Latex gloves were also used when applying alcohol based solvents to remove the paint. Per the painting instructions available on ISSI's website, seven to eight layers of paint can be applied to a model without applying a base coat and approximately 30 seconds is needed for the paint to dry so that the next layer can be applied. It was found that at a room temperature of approximately 73°F, longer wait times are required before the paint can be applied for additional coats. The "slippery finish" and curves of the highly-cambered airfoil lead to downward drooping of the paint film immediately after application. The initial results can be seen in Figure 29.

Non-uniformities in the paint were evident after a few minutes of drying. It was determined that the paint was slipping down the trailing edge of the airfoil as it was drying. To alleviate that problem, an additional foam piece was placed under the trailing edge to reduce the angle to the horizontal of the trailing edge. A special alcohol based paint remover was used to remove the PSP, and the model was masked with masking tape and painted again.
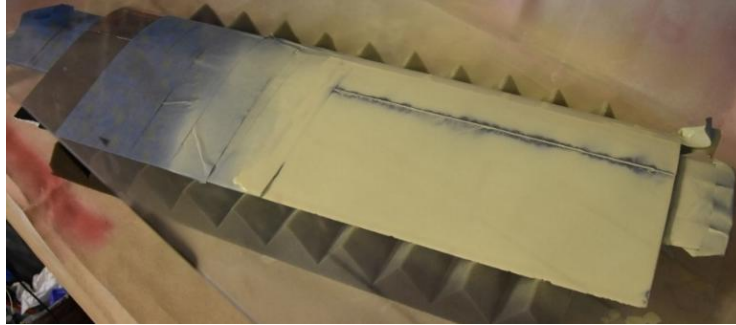
Figure 29. Non-uniform application of paint to the model

Eventually, it was decided to apply three to four layers of primer to provide the grit the PSP layers needed in order to stick to the surface. After removing the PSP, it was found that the solvent used attacks the airfoil paint, so the model was cleaned, sanded and painted so that it was ready for applying the primer. After applying four layers of primer, eight layers of PSP were applied to the model. The final result can be seen in Figure 30.
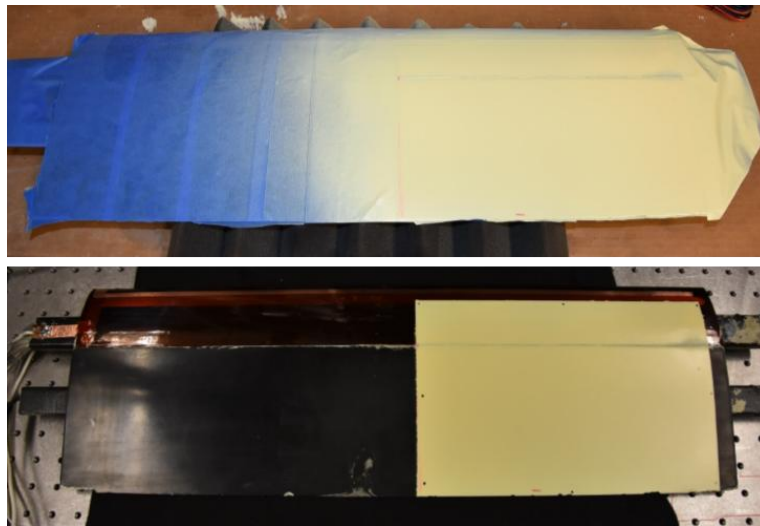
Figure 30. Surface finish after applying primer as base coat to prevent sagging and

drooping

Uniform model illumination is of prime importance if image intensity saturation to be avoided. Non-uniform model illumination, in addition to vibration and alignment issues, contributes significantly to uncertainty in PSP experiments. Achieving uniform model illumination can prove to be a challenging task depending on the test facility and optical access in that facility. Although the high subsonic facility in the GDTL provides ample optical access from sides, the optical access from above, as mentioned before, is somewhat limited due to the presence of a probe traversing mechanism. Initially, the UV LEDs were installed laterally. After examining the acquired images, the model illumination was deemed insufficient and local saturation of intensity proved to be an issue. The LEDs were originally placed laterally to illuminate the entire surface of the airfoil, but as measurements over the entire surface of the airfoil proved difficult to implement, the left LED was relocated to the top of the test section and closer to the airfoil surface. The camera was also moved closer to the model to increase the signal strength and the signal to noise ratio. The final configuration of the setup is depicted in Figure 31.

The LED on top of the tunnel was mounted on a traverse arm so that its position could be adjusted to achieve the best illumination possible. The LED array mounted on the side was installed on a custom-built mount which made adjustments in height, yaw, and pitch possible. The images seen in Figure 12 show different stages of adjusting LED positions until a uniform light distribution was obtained.
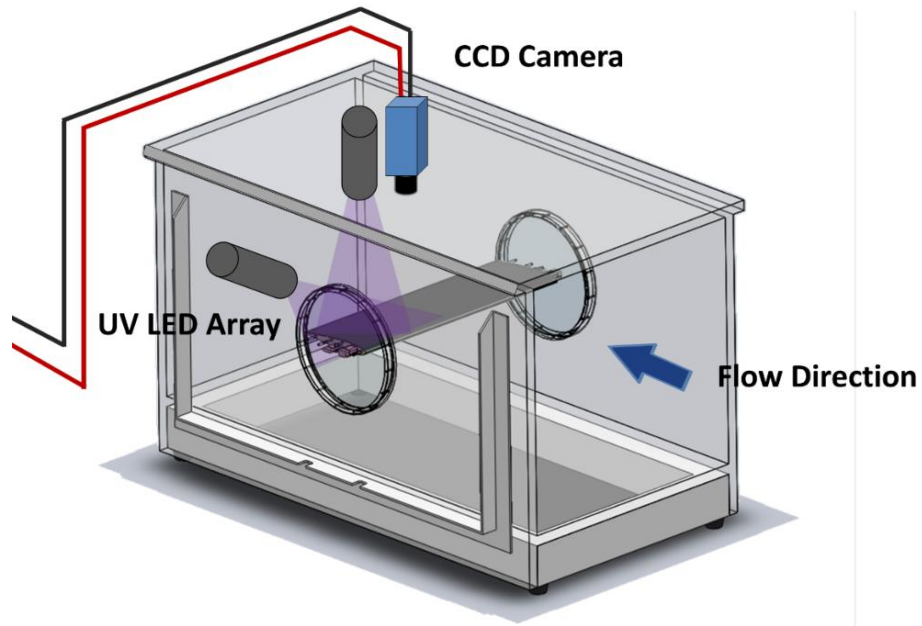
Figure 31. Schematic of the final setup
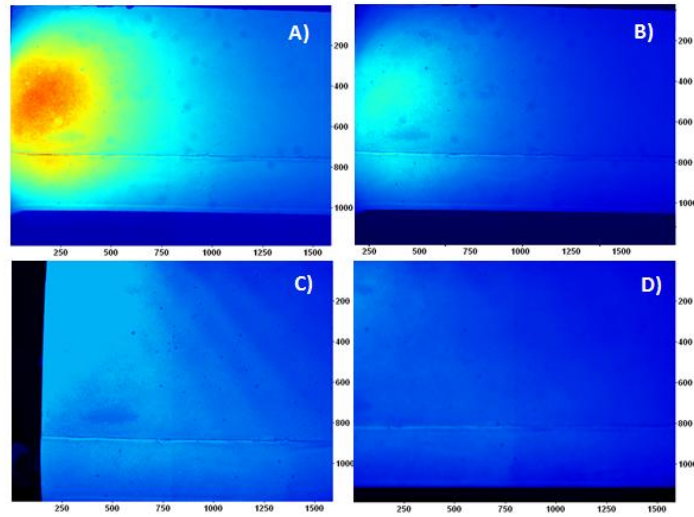
Figure 32: Achieving nearly uniform illumination after successive adjustments of camera

and LED arrays a) Original light position b) Rotated towards leading edge 5 degrees c)

Rotated towards leading edge 10 degrees d) Final light position

A 14-bit, 1600×1200 px PCO 1600 camera with a 35 mm f/1.8 lens was used to acquire the images. This initial combination of lens and sensor area proved to be unsatisfactory as a wider field of view (FOV) was needed to cover a greater area of the airfoil surface. Thus, several lenses with shorter focal lengths were tested. The first choice was a 28 mm f/1.2 lens and the second candidate was a 18 mm f/3.8 lens. Although the 18 mm lens provided a larger FOV, the amount of light entering the camera was not enough due to its smaller aperture size (f/ 3.8 vs/ f/1.2) and subsequently it was decided to use the 28 mm lens with an exposure time of 0.256 s.

It must be mentioned that the camera at its full bit depth was never saturated with the tested combination of illumination, exposure and aperture. Artificial adjustments of bit depth in the DaVis software package make it possible to spot non-uniformities in illumination but nevertheless, the camera is not saturated. Nevertheless, it seems that in some cases, due LED light reflections from tunnel's Acrylic walls, the paint is saturated. Model illumination by two 409 nm LED arrays and the green glow of the reference signal can be seen in Figure 33.

The following sections describe the steps that have been taken to acquire and reduce the PSP data. The flow field was assumed to be steady with negligible unsteadiness over time. A batch of 20 images were acquired at 5 Hz for each case (e.g. wind or wind off) using DaVis software package. The acquired images can then be averaged to account for variations in model illumination and movement over time and to obtain a better SNR. No dark images were acquired during the course of the experiments and consequently, no

54

image corrections were applied to the data using DaVis package. The acquired images were then converted to 16-bit TIFF files and imported in MATLAB and were saved in RAM as matrices. All of the intensity values were converted to double using `double()` commands. The data reduction code in Appendix C may be consulted for further insight. The diagram shown in Figure 34 shows the data acquisition and reduction flowchart.
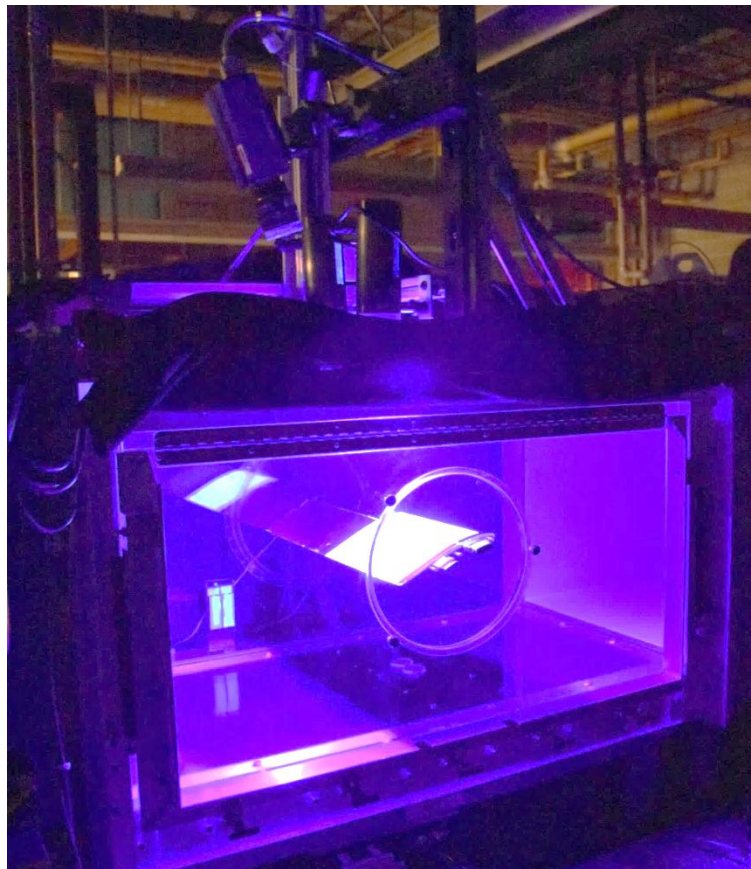
Figure 33: Model illumination by LED arrays. The green glow of the reference signal is visible
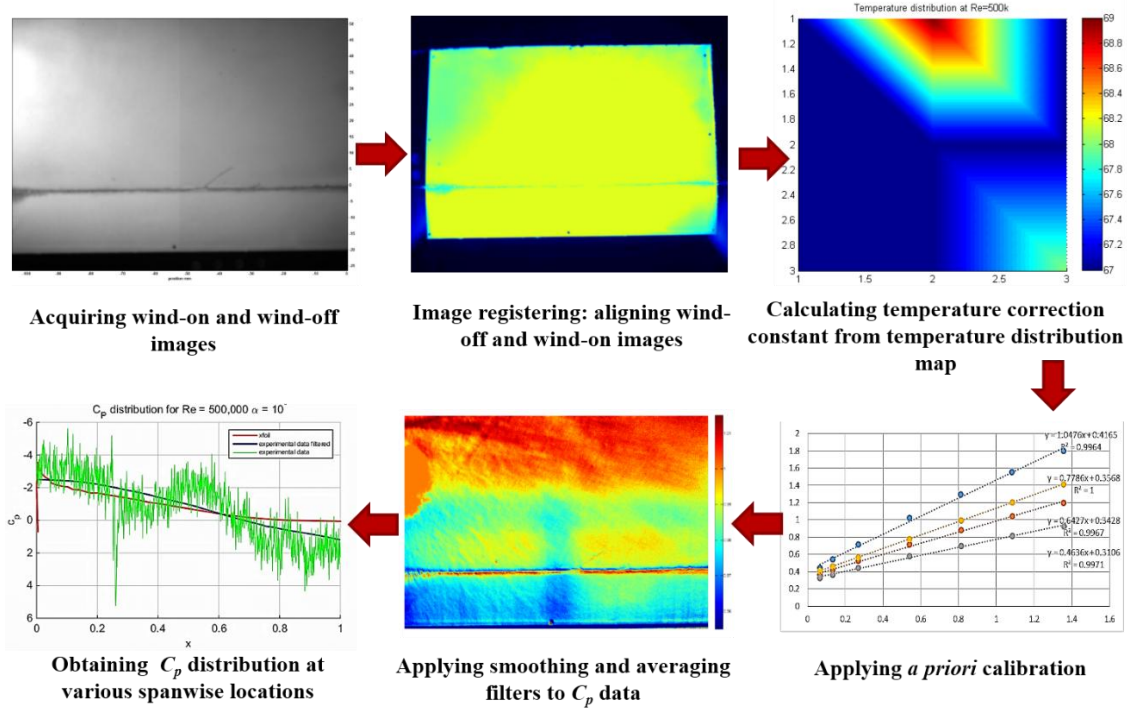
Figure 34. Summary of the steps taken to process the data

The effects of model deflection and rotation due to aerodynamic loads, specifically at higher Reynolds numbers, on intensity ratio maps must be corrected using image registration techniques. Figure 35 displays the raw wind on and wind off for Re = 10^6 at α = 10°. After the images were averaged, MATLAB's intensity-based `imregister` function is used for image registration. `imregister` transforms the averaged wind on image so it is registered with the averaged wind off image. Figure 36 displays the average wind-on and wind-off image. The output registered image is the new wind-on image. A transformation type, describing the model movement needs to be applied to the `imregister` function to create a new image.

56
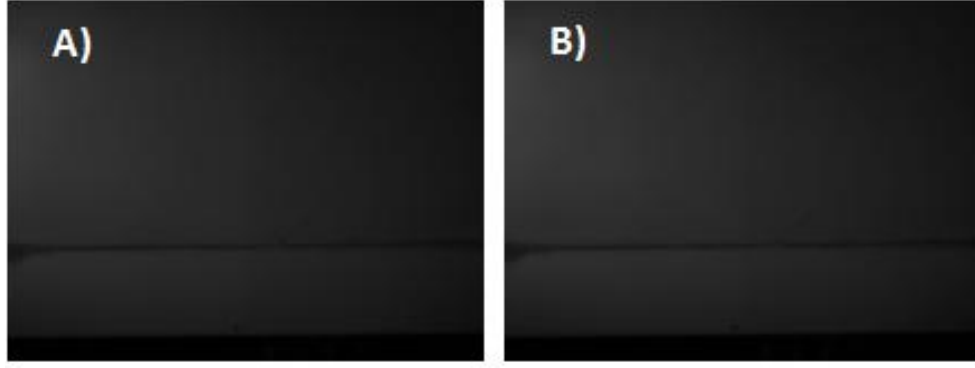
Figure 35. Raw intensity images for Re = 10^6 at α = 10° baseline case A) Wind on, B),

wind off
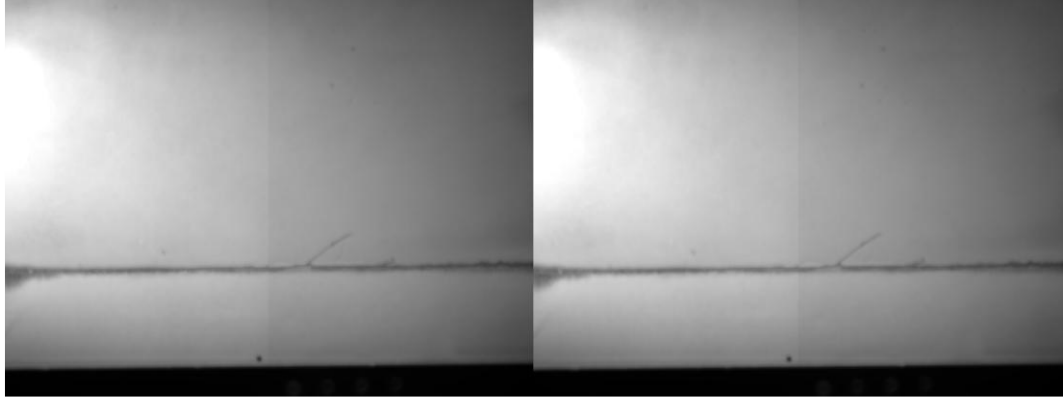
Figure 36. Averaged wind on and wind off Image for Re = 0.5 ×10^6 at α = 10°

At first it was assumed that the model movement between the wind-on and wind-off states can be attributed to only translation of the pixels. Using this logic, the model motion was treated as translation. The resulting image from this transformation type was not satisfactory. Consequently, the remaining two transformation types, namely *rigid* and *similarity* were explored. *Rigid* is a rigid transformation consisting of translation and

57

rotation, while *similarity* is a non-reflective similarity transformation consisting of translation, rotation, and scale. *Similarity* was the transformation type used to register the images for all of the cases. A sample intensity ration map obtained with this transformation is plotted in
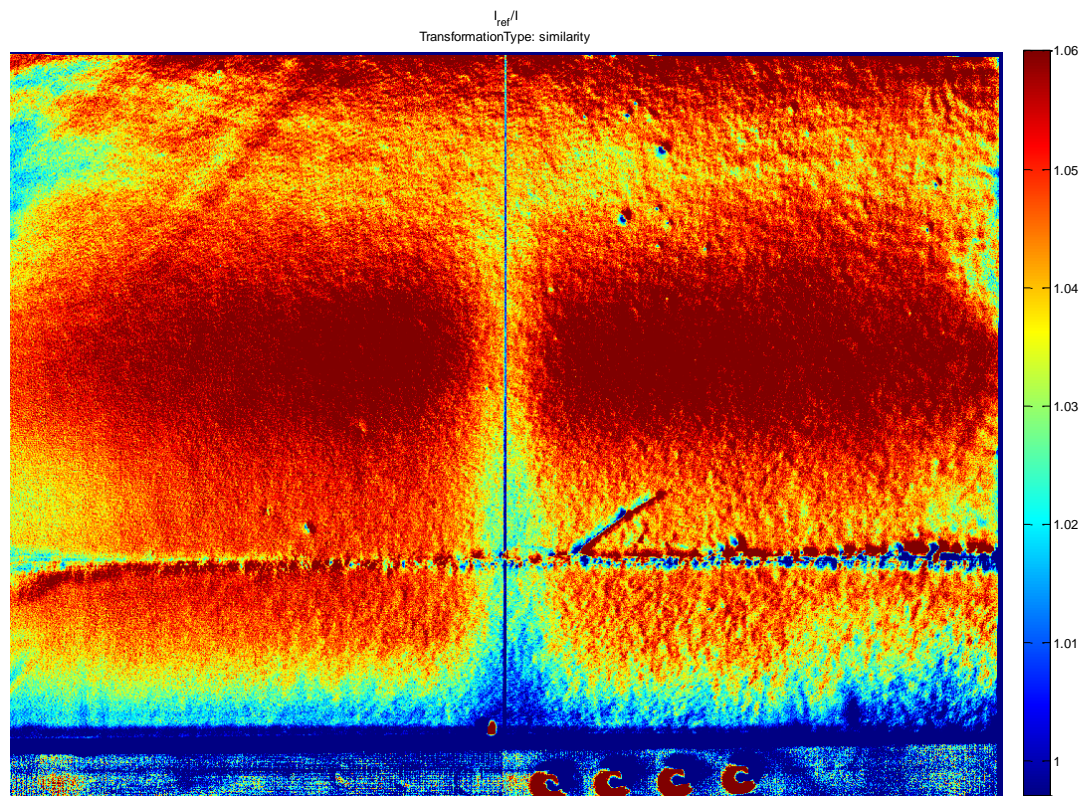
Figure 37. Intensity ratio map created using similarity transformation

After a registered wind on image was created using `imregister` the intensity matrix, $I_{ref}/_I$, where I_ref is the wind off image, was created by dividing the wind off image by the wind on. A filter was applied to the resulting matrix. The MATLAB function `imfilter` was used. It filters the intensity matrix with a user specified multidimensional filter. An averaging filter the size of the intensity matrix was used. Figure 38 shows a cropped unfiltered and filtered intensity image and Figure 39 shows a plot of the unfiltered and filtered intensity values at a spanwise location. The image was cropped to only include a region of the image with favorable translation, as well as remove the copper tape from the actuators, which produced a false intensity reading.
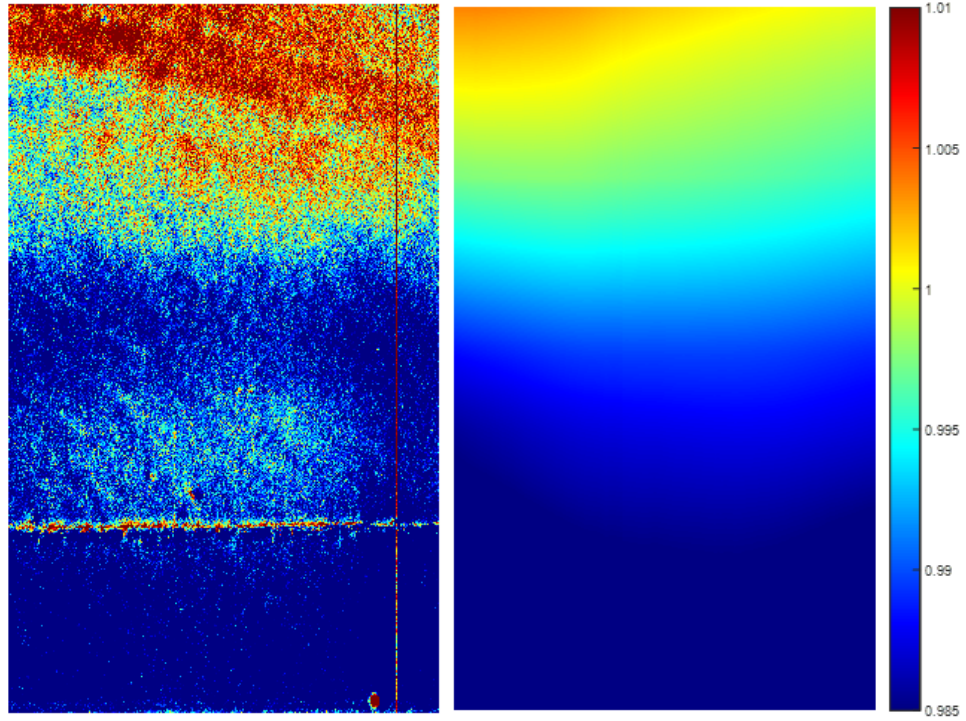
Figure 38. Unfiltered and filtered $I_{ref}/_I$ maps for Re $= 0.5 \times 10^6$ at $\alpha = 10°$

59
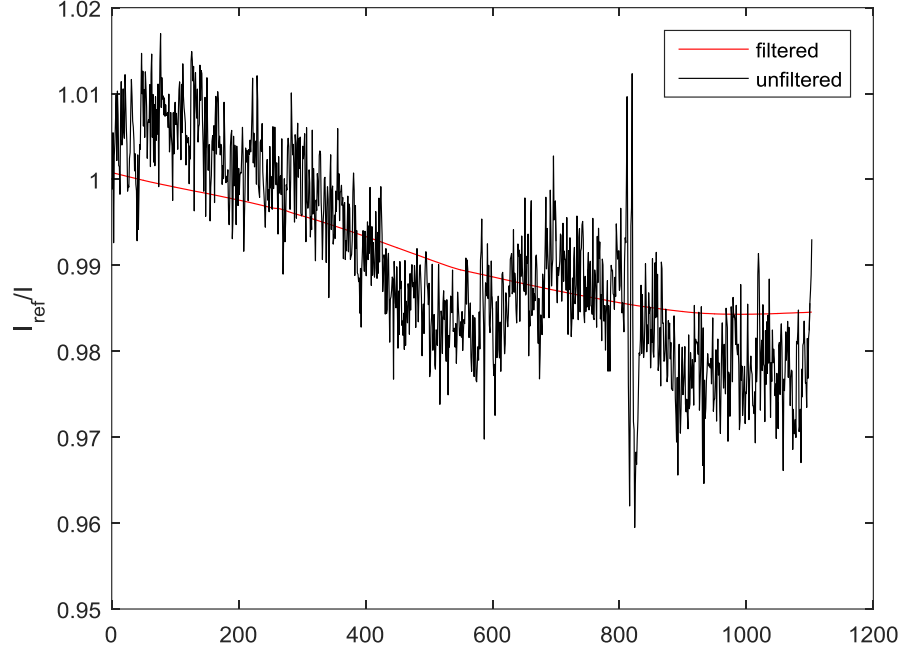
Figure 39. Unfiltered and filtered ${}^{I_{ref}}\!/_{I}$ at a spanwise location for Re = 0.5 × 10⁶ at α = 10°

Model surface temperature distribution was needed to apply temperature corrections and it was measured using a hand-held thermometer at two Reynolds numbers, namely 500k and 1000k. For each case the tunnel was brought up to speed and was run for about 20 minutes. The tunnel was shut off immediately at the 20-min mark and the side acrylic wall was removed to perform measurements. The measurements were carried out for a total of 9 points that have been marked previously on the surface of the model for image registration. The measurements were carried out only for the portion of the airfoil on which the PSP was applied. The results can be seen in Figure 40. The top side of the plot corresponds to the airfoil's LE and the tunnel wall is on the right side of the plot.

60
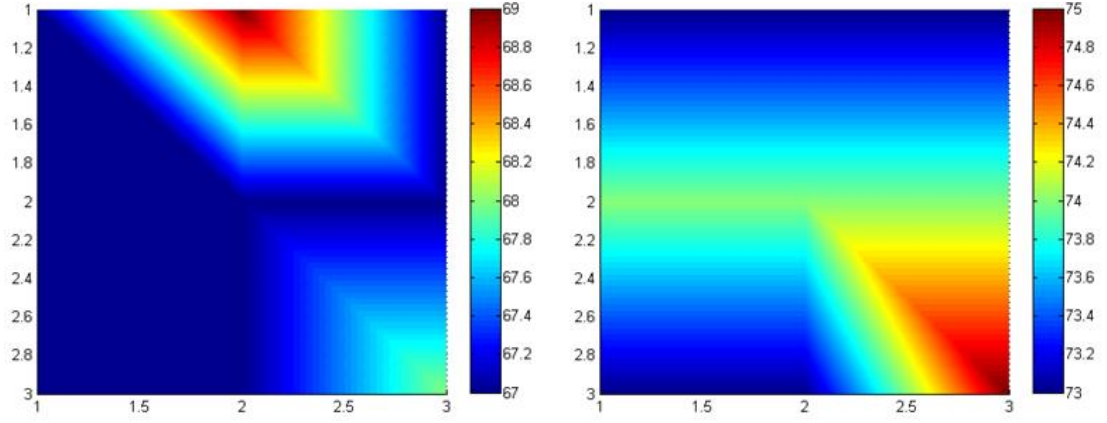
Figure 40. Temperature distribution on model at right) Re = 0.5 × 10⁶ and left) Re = 1.0 ×

10⁶

As can be seen in Figure 40, the portion of the model close to the TE and adjacent to the tunnel wall always experienced a higher temperature. This can potentially explain the suspicious pressure distributions that were obtained close to tunnel wall and TE. It was also observed that the average surface temperature is always much lower than the tunnel readout and that could have contributed to errors in PSP measurements. To account for these effects, a simple scheme, report by Bencic at NASA Glenn was adopted to obtain temperature corrected maps of intensity ratio distribution. The following steps were taken to apply a temperature correction to the data. First, an interpolation for the average surface temperature has to be carried out to obtain intensity vs. pressure ratio curve for a specific temperature. Then, the linear curve is collapsed on the reference temperature curve (at 298 K) using the following relation

$$\left(\frac{I_{ref}}{I}\right)_{Corrected} = (CT^2 + DT + E)\left(\frac{I_{ref}}{I}\right)$$

61

The constants C, D and E are obtained through the calibration curves that are presented in Figure 41. Bencic recommends that for the cases where the temperature gradients are not so severe, the intensity ratio correction are carried out first and then the *in situ* calibration, using surface pressure taps, be applied to the data. Once the intensity ratio matrix is formed, the calibration curve from Figure 25 can be applied at the corresponding surface temperature to achieve the pressure ratio. Data from Figure 25 is interpolated to create calibration lines at the surface temperatures achieved at the Reynolds numbers tested. A least squares linear fit is used to describe the reference curve at T= 298 K and P = 14.7 psia which has the following form

$$y = ax + b$$

where a = 0.6383 and b = 0.3469. The calibration curves at different temperatures can be seen in Figure 41. The temperature dependency of Stern-Volmer relation constants for BUNC-12 paint can be seen in Figure 26. The following relation was used to convert pressure values to pressure coefficients on top of the airfoil

$$c_P = \frac{p - p_\infty}{\frac{1}{2}\rho_\infty U_\infty^2}$$

where ρ_∞ is the ambient air density, p_∞ is the freestream static, U_∞ is the freestream velocity and p is the surface pressure. Unfiltered and filtered surface maps of the intensity ratio and pressure coefficient are shown in Figure 43 and Figure 44. Figure 45 shows the pressure coefficient values at a spanwise location.
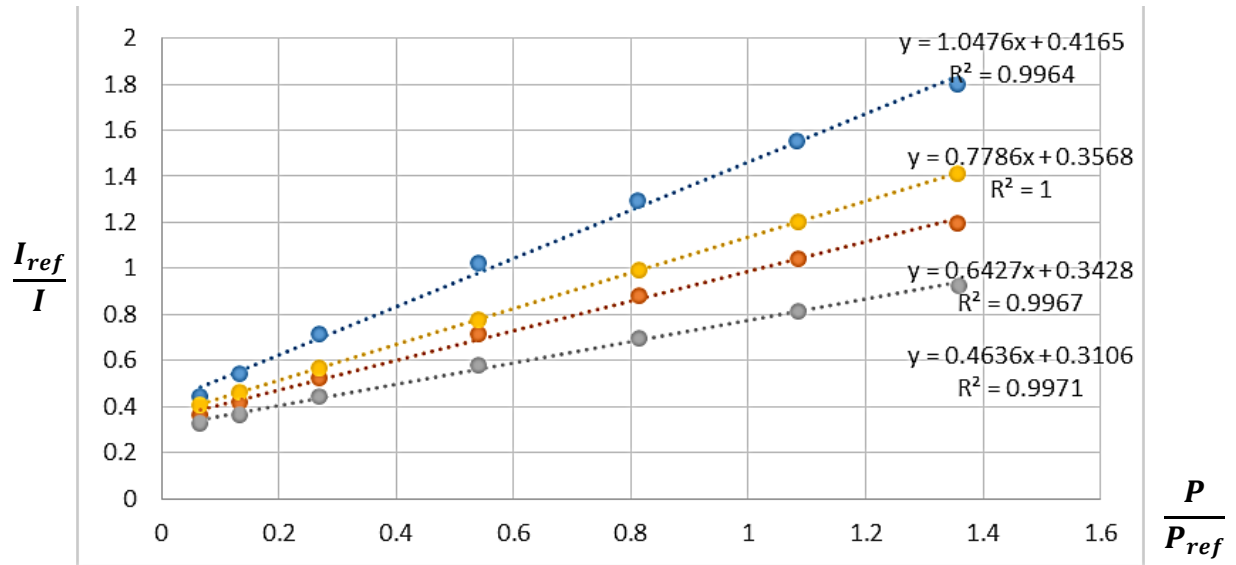
Figure 41. Calibration curves for various temperatures, binary BUNC-12 paint

M (T)

y = 0.0195x - 5.0831

B (T)

y = 0.0035x - 0.6953
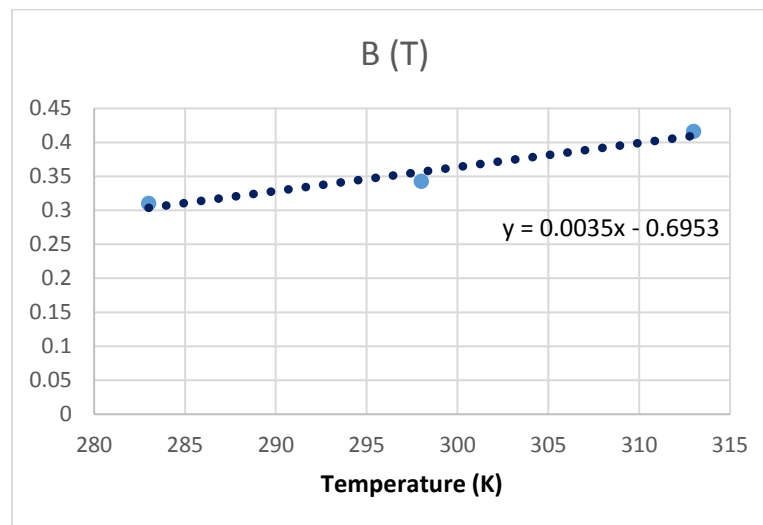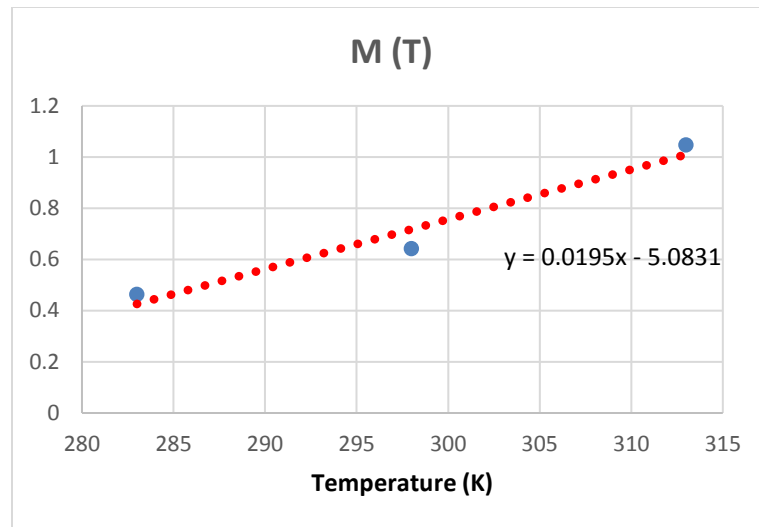
Figure 42. Temperature dependency of Stern-Volmer constants for BUNC-12 binary

paint
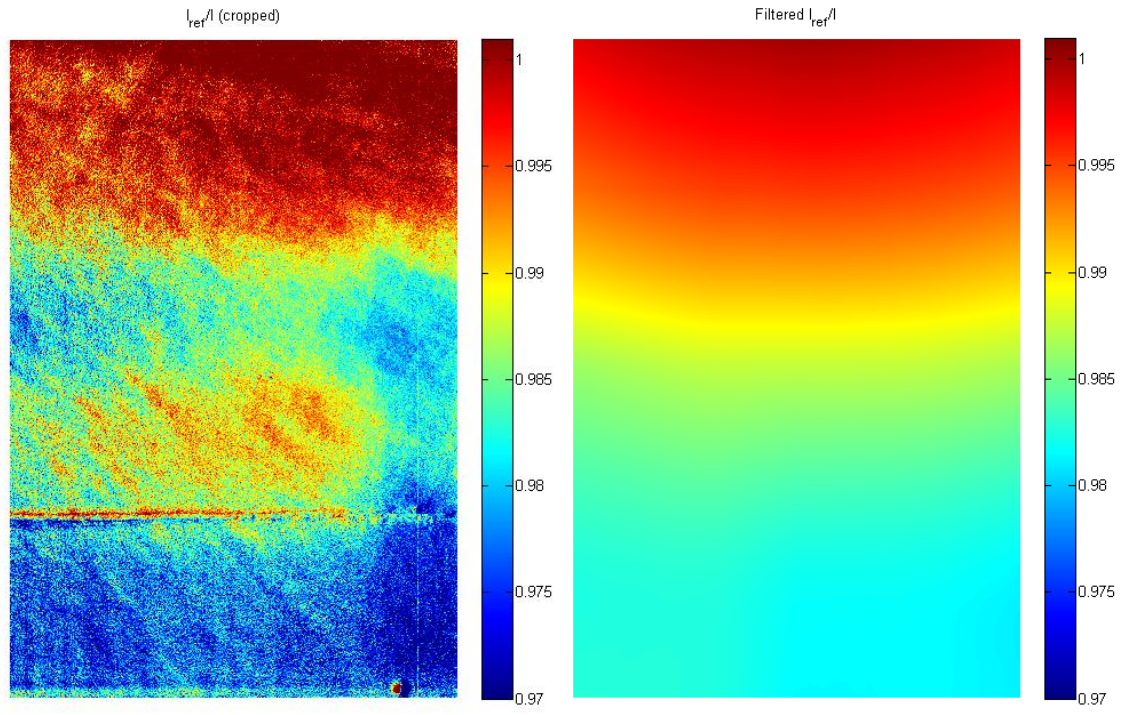
Figure 43. Unfiltered and filtered intensity ratio distribution for Re = 0.5×10^6 at α = 10°
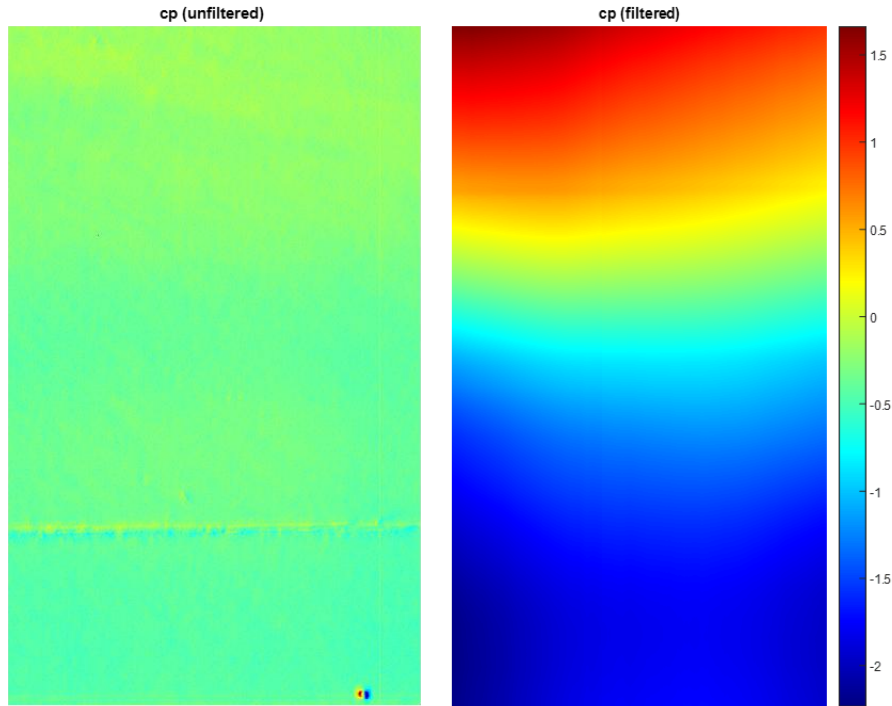
Figure 44. Unfiltered and filtered maps of C_p distribution for Re = 0.5×10^6 at $\alpha = 10°$
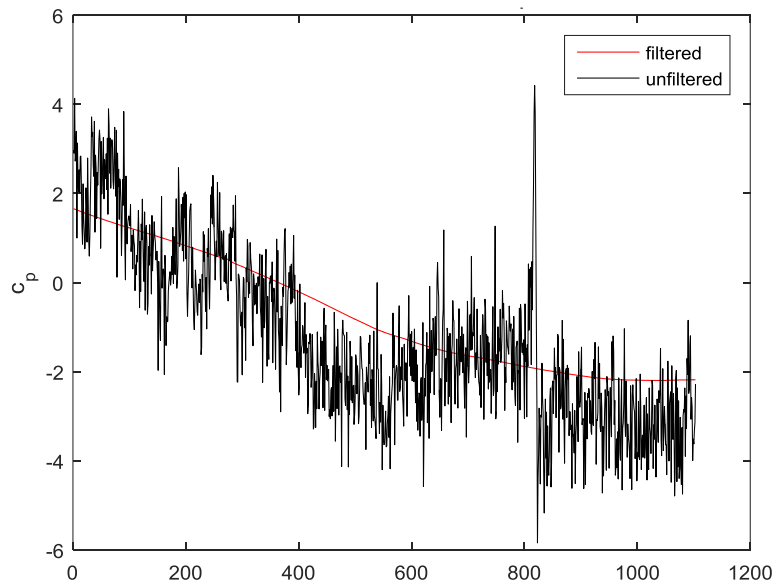
Figure 45. Unfiltered and filtered C_p at a 10% span location for Re = 0.5×10^6 at $\alpha = 10°$

A comparison between pressure tap data, numerical simulation data from XFOIL and PSP data for $Re = 0.5 \times 10^6$ and 1.0×10^6 at $\alpha = 10°$ can be seen in Figure 46 and Figure 47, respectively. As is evident by examining Figure 47 applying a filter to the data at Re $= 1.0 \times 10^6$ at $\alpha = 10°$ results in physically accurate data as only positive pressure coefficient values are obtained from applying calibration to intensity ratio data before applying a filter. It must be mentioned that a temperature correction factor was also applied to filtered data for both cases at Re $= 0.5 \times 10^6$ and Re $= 1.0 \times 10^6$ at $\alpha = 10°$. The numerical value of pressure coefficient obtained from intensity ratio maps was off by a considerable margin without applying a temperature correction.

The general trend and magnitude of the pressure coefficient curves obtained from PSP data agrees very well with surface pressure tap data. These data confirm the fidelity of the PSP measurements carried out in this work. As the fidelity of intensity ratio maps obtained is confirmed, only surface maps of intensity ratio will be presented for the flow control study.

67
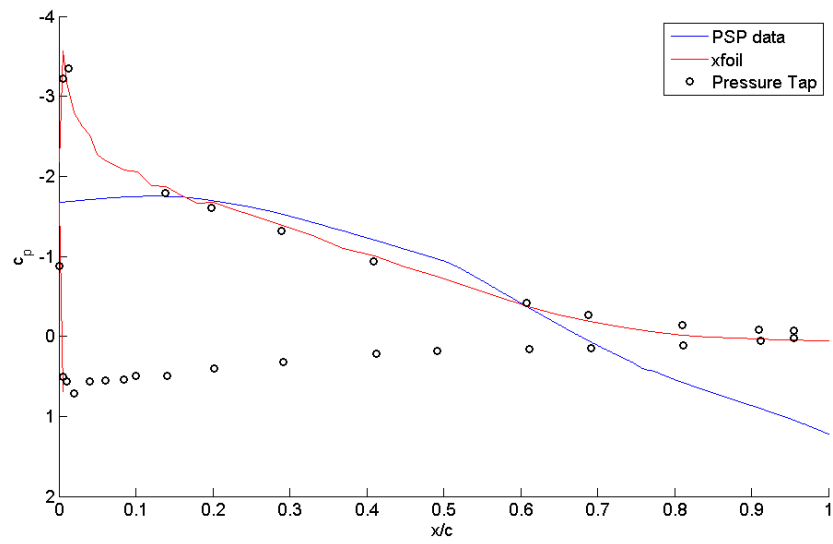
Figure 46. Comparison between pressure tap data, XFOIL simulation results and PSP

data for Re = 0.5×10^6 at α = 10°
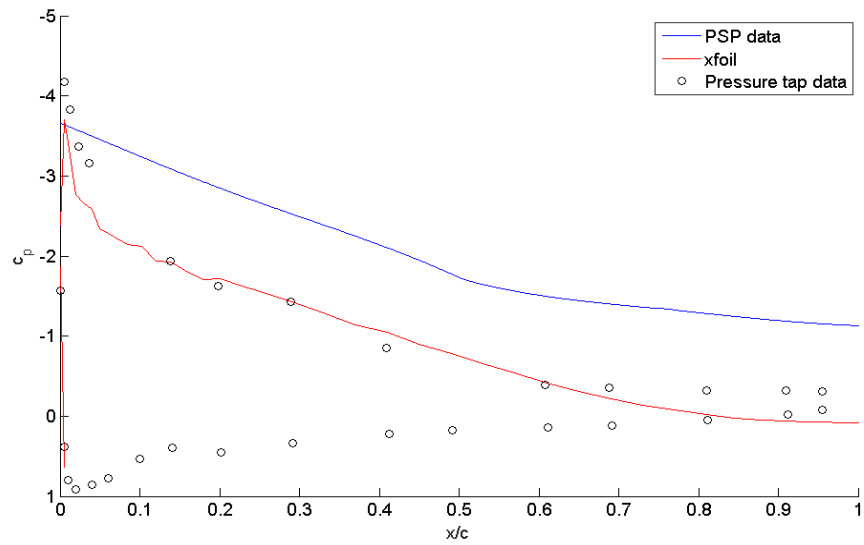
Figure 47. Comparison between pressure tap data, XFOIL simulation results and PSP

data for Re = 1.0×10^6 at α = 10°

3.3.3 Schlieren

To study the optical emissions and convection of the thermal hotspot generated by nanosecond discharges in actual wind tunnel experiments, an existing Z-type Schlieren system was modified to increase its sensitivity as the gradients of the flow features in a subsonic, low-speed flow are negligible and therefore hard to detect. The system has two main sections, namely the illuminator and the analyzer sections. The illuminator section relies on a Dragon HPLS-36DD18A high-power LED light source from Light-Speed Technologies for illuminating the flow. The light source can be operated in either continuous mode, for aiming and adjustments, or triggered mode with a minimum pulse width of 100 ns. The LED driver is powered by a DC power supply and the light intensity can be varied by adjusting the DC output voltage from 10 to 18 VDC. As the sensitivity of the system is inversely proportional to the dimensions of the light source[63], it is essential to have a "point source" for maximum sensitivity. A combination of a spherical condenser lens, with a focal length of 20 cm, and a 800 μm pinhole, seen in Figure 48 were used for this purpose. The available parabolic mirrors had 72" focal length which helps to increase the sensitivity of the system to small changes in refractive index. Due to the relatively long focal length of the parabolic mirrors and the limited available space in the tunnel infield, the beam had to be folded twice in the illuminator section of the system with the help of two square first surface mirrors. As the collimated beam passes through the test section, it is collected on the other side by the analyzer section of the system (Figure 49). The knife edge was mounted on a high-precision micro translation stage that would enable the user to "calibrate" the system by obtaining *Δx-I* curves (beam displacement vs. light intensity in the image). By applying the

69

calibration to the acquired images as described by Settles[63], [64] it is possible to quantitative data, such as maps of temperature and even velocity, from Schlieren images. A 14-bit, 2048×2048 Imager Pro X 4M camera, previously used in the PIV experiments, along with a 60-300 mm, f/4.5-6 variable focal length Nikon lens was used for acquiring the images. The use of this particular lens allows the operator to zoom-in on any desired part of the flow field and take advantage of the entire camera sensor surface area. Furthermore, the use of a camera compatible with DaVis facilitates the acquisition of images as the existing hardware for phase-locked PIV measurements can be used without any modifications. The LED can be triggered and controlled as a light source by DaVis and the camera gate trigger can be synchronized with the light source without using a delay generator. The camera and light source were triggered by the actuator excitation signal.

The light source trigger signal was found to be extremely sensitive a EMI from the tunnel fan. This issue was addressed with the use of a low-pass filter. The Acrylic tunnel windows also proved to be problematic. The striations and non-uniformities that existed in the Acrylic disks were easily detected by the sensitive Schlieren system and affected the quality of the acquired images. Another factor that influenced the quality of the images was the particularly long beam path of the collimated light. As the Schlieren system integrates all the density changes along the collimated beam path, the system was registering the changes in density caused by the draft created by the air conditioning system of the lab. These effects can be seen in a samples Schlieren images shown in Figure 50. Nevertheless, the system was able to register the compression waves and the thermal hotspot created by the nanosecond discharge at various tunnel conditions.
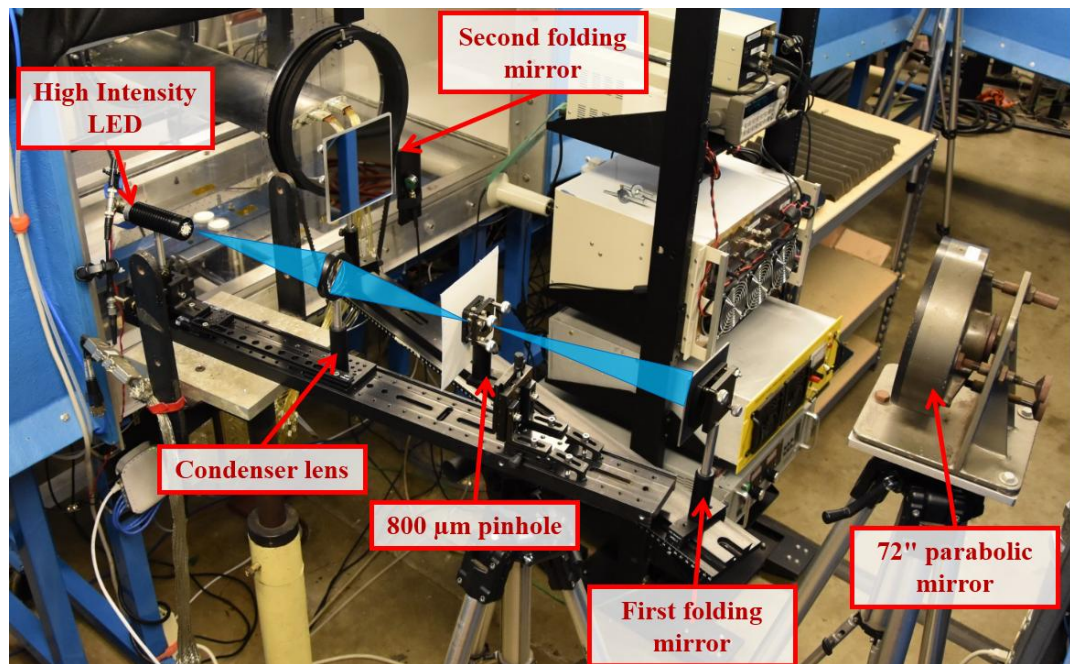
Figure 48. Illuminator section of the Z-type Schlieren system
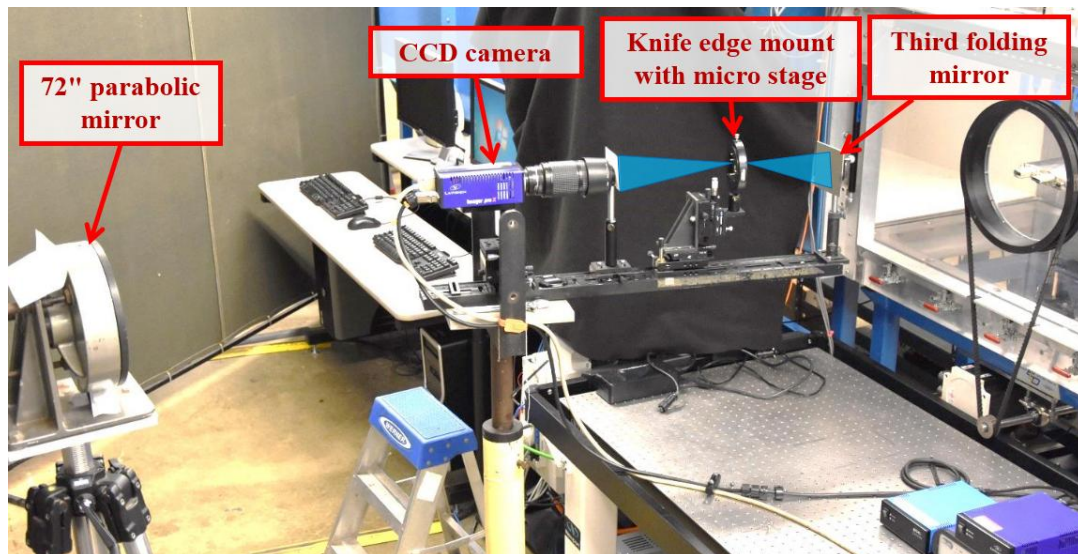
Figure 49. Analyzer section of the Z-type Schlieren system
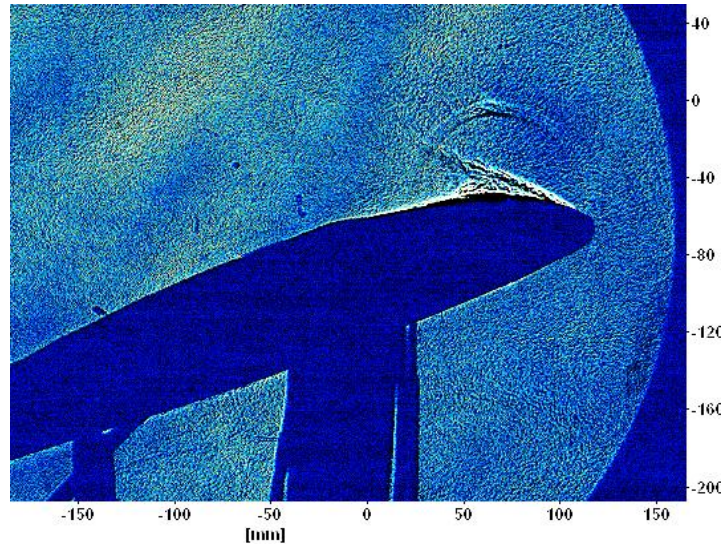
Figure 50. Sample Schlieren image depicting the compression wave and hotspot created by the discharge

Further details of the Schlieren system including component spacing and beam angles can be found in Appendix A.

3.4 Surface Oil Flow Visualization

3.4.1 Fluorescent Surface Oil Flow Visualization

Fluorescent surface oil flow visualization was employed to study the flow topology over the airfoil under various conditions. A mixture of 10,000 and 350 cSt silicone oil (3 parts 10,000 cSt oil and 7 parts 350 cSt oil) with a viscosity of approximately 1000 cSt was used to hold the fluorescent pigments. The viscosity of the oil was chosen in such a way to allow the observation of any unsteadiness in separation line location and at the same time, prevent excessive amounts of the mixture from flying off the model.

72

The UV pigments had an average diameter of 5 to 20 μm and could be excited by visible light. Two 1000 W LED flood lights were used to illuminate the mixture (as shown in Figure 51) in 10 s intervals. The procedure for acquiring the images was as follows: first the angle of attack was set and the tunnel was brought up to speed. As soon as the desired conditions were established in the tunnel, the actuators were turned on. The final pattern was usually established after 6 minutes of run time. Laboratory lights would then be turned off and a Nikon D7200 DSLR camera with an 18-300 AF lens would be used to acquire the images in low-light conditions. Various stages of the experiment are depicted in Figure 52. Finally, the acquired images were de-skewed, and plotted using MATLAB.
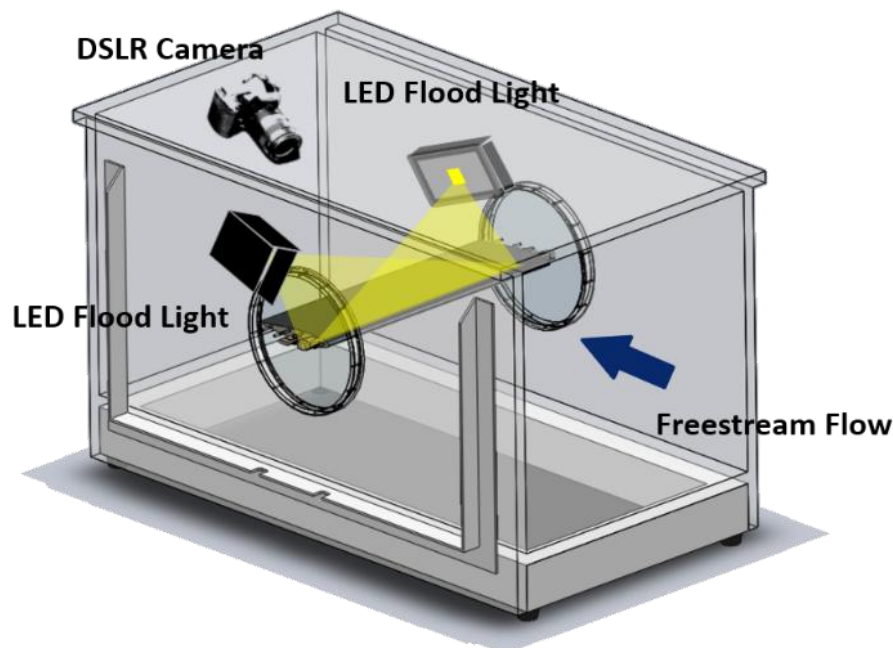
Figure 51. Fluorescent oil flow visualization setup
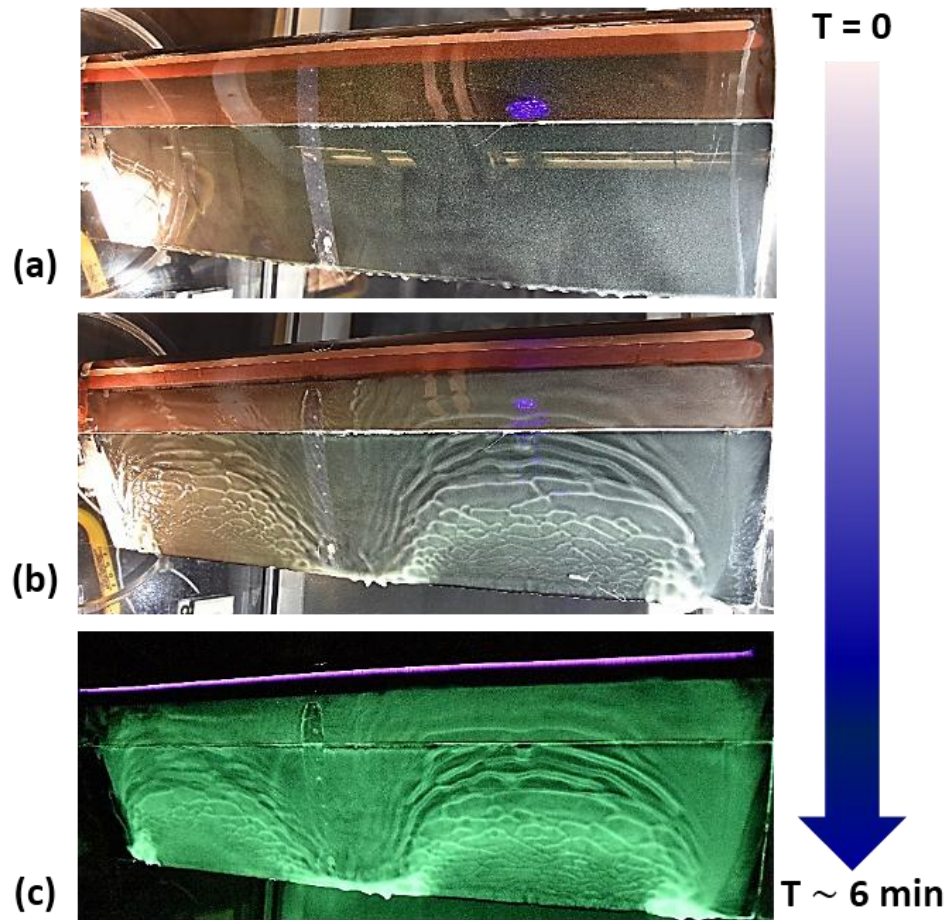
Figure 52. Unprocessed images depicting (a) model covered with a thin sheet of oil in quiescent flow conditions (b) illuminated model once steady flow is established (c) fluorescence emissions in the dark lab

3.4.2 Paint-based Surface Oil Flow Visualization

The application of the paint Surface oil f low visualization (SOFV) utilizes shear stress at the wall to distort a thin application of oil to indicate near-wall ow features. This makes it

useful for characterizing regions of separated ow, since the oil in the separated region will be either undisturbed or owing in the reverse direction. Titanium white oil-based paint was mixed with SAE 85W-140 gear oil at a mass ratio of 1:4. The mixture was spread thinly and evenly by hand in a roughly 50×100 mm rectangular patch at the ATE. The mixture was applied to the model surface using a paint brush which resulted in a very smooth finish. The mixture was applied off-center to avoid the static pressure taps (discussed in the next section). The wind tunnel was quickly brought to the desired ow velocity and allowed to run until the mixture had moved enough to clearly indicate separation. Photographs of the mixture were acquired with the tunnel in operation, then the tunnel was abruptly stopped (to minimize disturbance) and more closely examined.
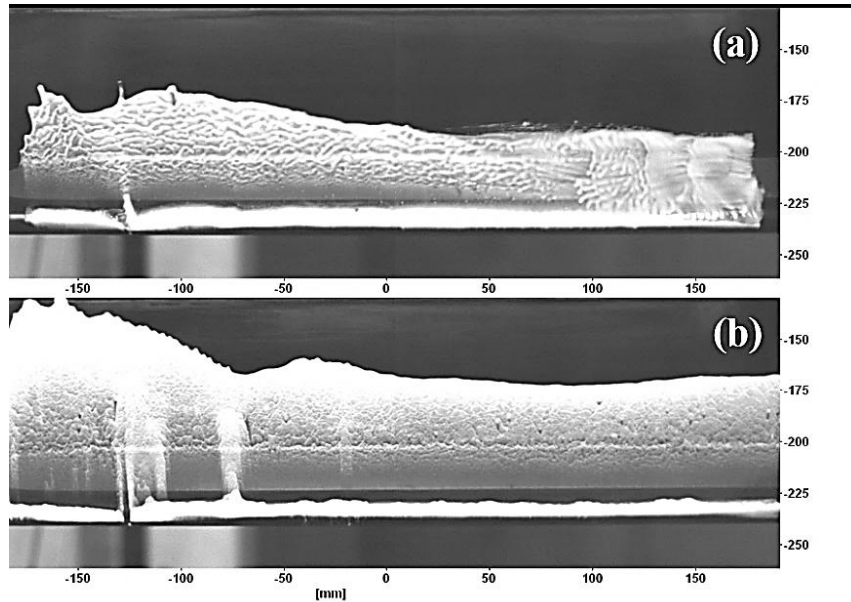
Figure 53. Sample oil flow visualization images showing the effect of Reynolds number on the size of the laminar separation bubble at α = 12° (a) $Re = 0.5 \times 10^6$ (b) $Re = 1.0 \times 10^6$

3.5 Static Pressure

3.5.1 Time-averaged Pressure Measurements

Static pressure measurements on the airfoil surface were acquired using three Scanivalve digital pressure sensor arrays (DSA-3217). A total of 35 taps are located on the surface of the airfoil and the tap distribution is shown in Figure 6. As indicated by the figure, 3 taps are covered by the plasma actuator. As such, data is from these three taps is ignored. The pressure coefficient, $C_p = (p - p_\infty)/q_\infty$, was averaged over 300 samples acquired at 1 Hz near the centerline, where p is the static pressure, p_∞ is the freestream static pressure, and q_∞ is the freestream dynamic pressure. The sectional lift coefficient C_L and drag coefficient C_D were calculated using the line integrals about the surface of the airfoil as shown by eqns. 3.2-3.4 where θ is the surface-normal angle and ds is the arc length.

$$C_L = -\int_{-1}^{1} C_p \sin\theta \, ds \qquad (3.1)$$

$$C_D = -\int_{-1}^{1} C_p \cos\theta \, ds. \qquad (3.2)$$

3.5.2 Unsteady Pressure Measurements

In order to study the time-dependent variations in surface pressure due to excitation at various regimes, the existing pressure data acquisition system was modified to allow for acquiring the pressure data at higher acquisition rates with smaller time delay. To reduce the time delay, the pressure sensor array was relocated closer to the test section and the

length of the pressure tubing was reduced from approximately 3m to 50 cm. The LabView data acquisition code was also modified at allow sampling the pressure data at 450 Hz. The modified LabView code can be coupled to the code that controls the automated operation of the tunnel although, as mentioned earlier, the tunnel control code proved to be highly sensitive to EMI-induced disruptions of the thermocouple signal which caused the control code to crash. This, in turn, terminated the pressure data acquisition sequence. Consequently, it was decided to run the pressure DAQ code independently. The MATLAB script used for processing and plotting the pressure data was also modified to accommodate sizeable arrays of time-dependent data. For excited cases, 4500 samples were acquired at each data point.
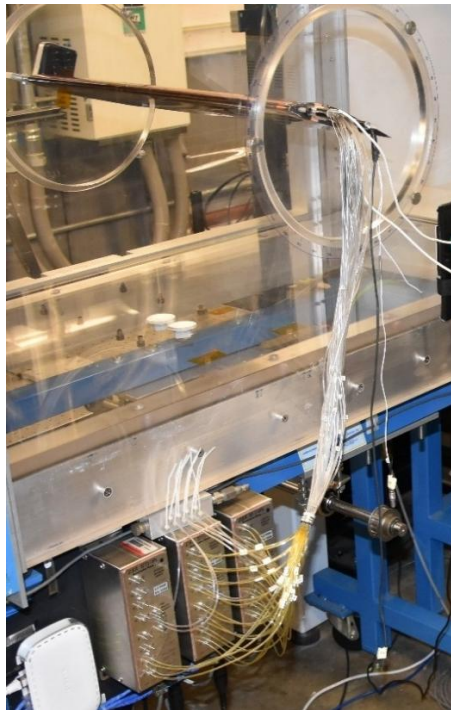
Figure 54. New arrangement for reducing the pressure tubing length
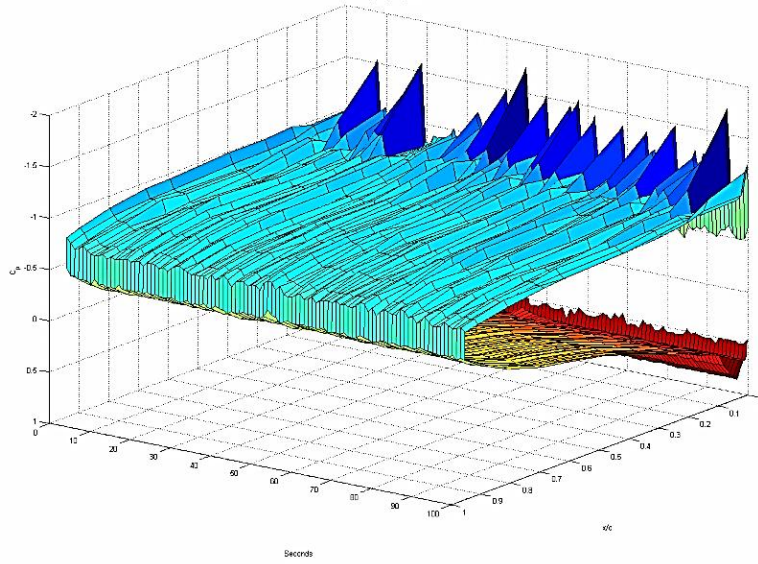
Figure 55. Sample data depicting the variations in pressure coefficient over time for an

excited case ($St_e = 0.6$)

3.6 Microphone Measurements

Pressure spectra were collected for the shear layer forming at leading edge using a microphone. The microphone was found to be much more EMI-resistant than dynamic pressure transducers or hot wire probes. Both baseline and forced pressure spectra were collected at a probe location of $x/c = 1.65$ and $y/c = 0.44$. This location is labeled as "D" in Figure 57 A Brüel and Kjær model 4939 microphone and a Nexus 2690 signal conditioner were used to acquire time-accurate pressure data. The sensitivity was set as 3.16 mV/Pa. The data was collected in 60 blocks of 2^{14} samples each at a sampling rate of 10 kHz with a frequency resolution bandwidth of 0.61 Hz. The power spectral density was calculated for each block before the blocks were ensemble-averaged. The power

spectral density was then converted into decibels using a reference pressure of 20 µPa. Strouhal numbers were calculated using the chord length of the airfoil, $St = fL/u_\infty$.

Figure 56. Positioning the microphone over the airfoil

$\frac{x}{L} = 1.65 \quad \frac{y}{L} = 0.44$

● D

$\frac{x}{L} = 1.00 \quad \frac{y}{L} = 0.32$

$\frac{x}{L} = 0.60 \quad \frac{y}{L} = 0.25$

$\frac{x}{L} = 0.20 \quad \frac{y}{L} = 0.17$

● B

● C

● A

y/L

x/L

L
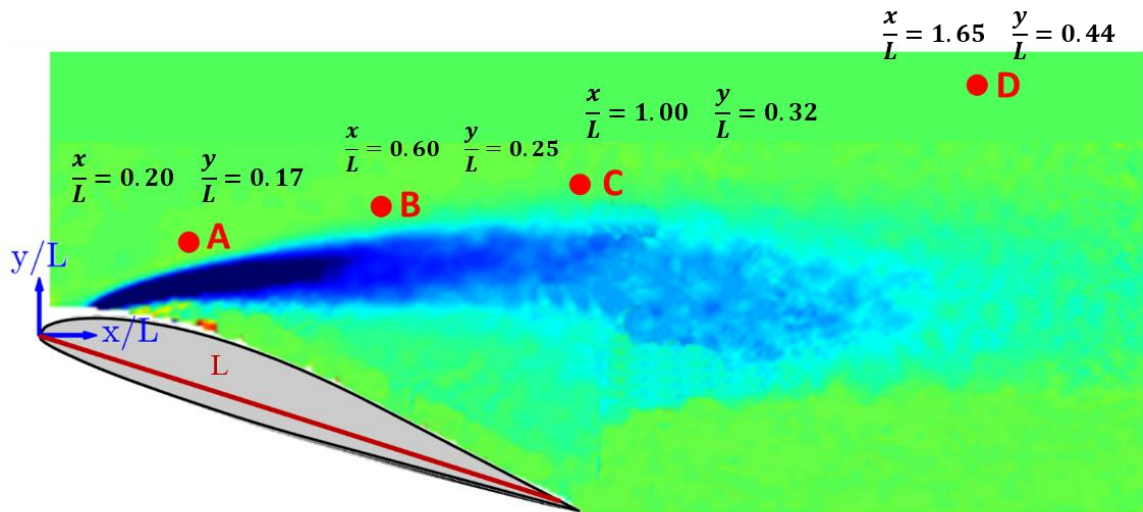
Figure 57. Map of vorticity distribution for the baseline case used for positioning the

microphone probe along the edge of the shear layer

3.7 Pulse Generator

The actuator is powered by a custom, in-house built pulse generator. The pulse generator utilizes a magnetic compression circuit to create the input waveform for the actuator. A DC power supply supplying 450 VDC is used to power the pulse generator. The specifics of the pulse generator are discussed in previous work by Little[15] and Takashima[24], [25]. Representative discharge characteristics were acquired for a ~570 millimeter long actuator driven at 100 Hz. Voltage and current traces are acquired using a LeCroy Wavejet oscilloscope (model 324A) simultaneously. A Tektronix high-voltage probe (model P6015A) is placed across the output terminals of the pulse generator and a Pearson current probe (model 2877) is placed on the ground output terminal of pulse generator (which is connected to the ground of the actuator). A total of 16 pulses were acquired and averaged. The voltage and current traces of this input waveform along with the power and instantaneous energy traces are shown in Figure 58. The peak voltage was 10 kV and the peak current was 36 A. The peak power consumption was 335 kW. However due to the narrow pulse width, the steady state energy consumption was 12.6 mJ per pulse. For the frequencies considered (less than 800 Hz), this corresponds to a time averaged power of 10 W. At the testing conditions, this corresponds to 3% of the freestream energy.
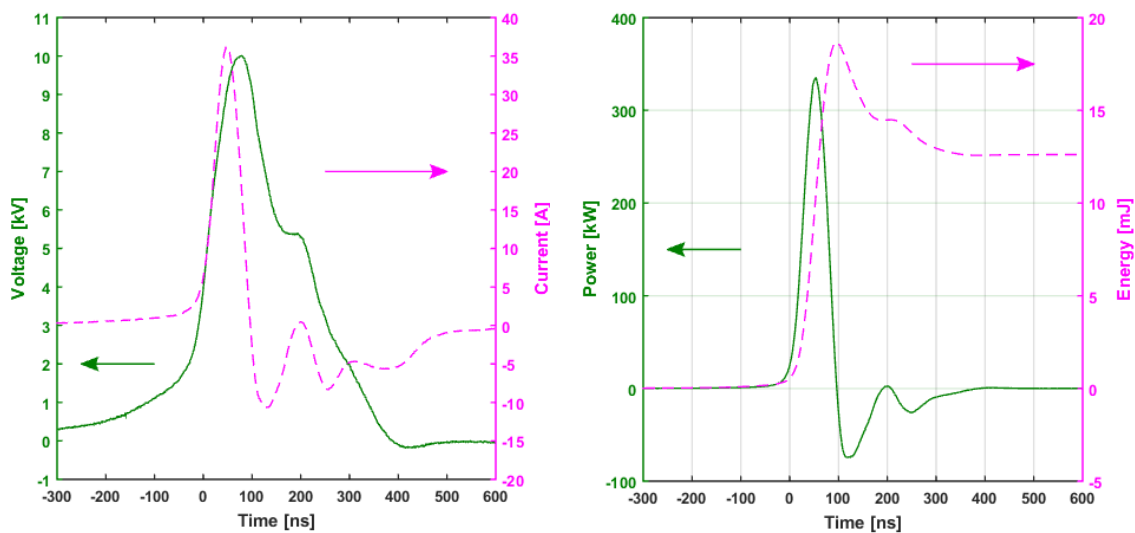
Figure 58. Traces of instantaneous (a) current and voltage (b) power and energy
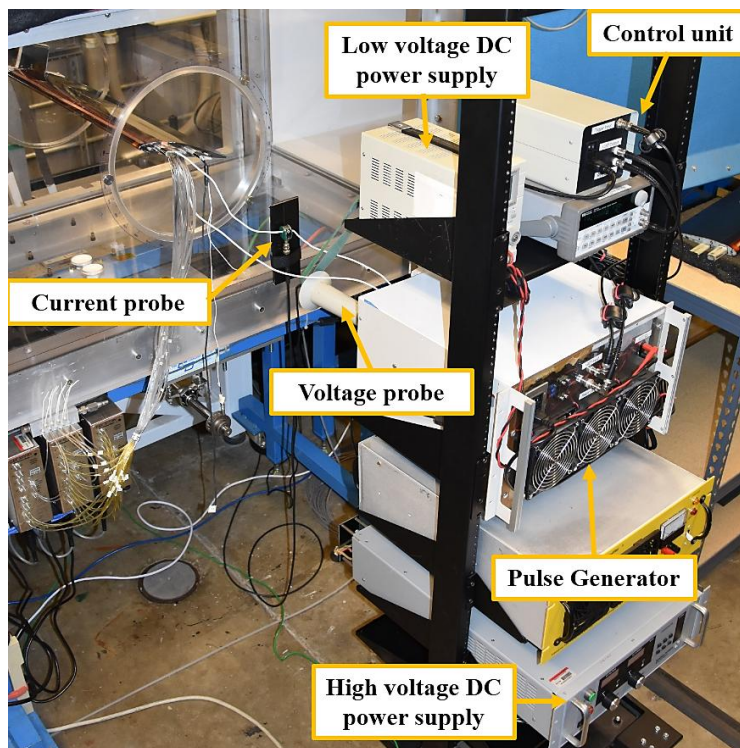
Figure 59. Pulser setup

Chapter 4: Results and Discussion

4.1 Baseline Characterization

A comprehensive characterization of the baseline airfoil was carried out to ascertain the behavior of the model at pre-and post-stall regimes. As the primary goal was to implement an actuator for separation control over the subject airfoil, particular attention was paid to determining the stall angle at various freestream velocities. The $C_l - \alpha$ curve presented in Figure 60 clearly demonstrates that this airfoil has a sharp drop in lift coefficient after the stall angle which is the known signature of airfoils with leading edge stall. Also, during the course of the experiments, it was noted that the stall angle would change in a narrow range between 15° and 17° when the experiments were repeated. This could be attributed to the unsteady nature of the stall on such an airfoil as reported by Greenblatt and Wygnanski [31]. It must be mentioned that the general trend of the $C_l - \alpha$ obtained at Re = 500,000 agrees favorably with the data reported by Mc Alister at *Re* = 120,000 [65].
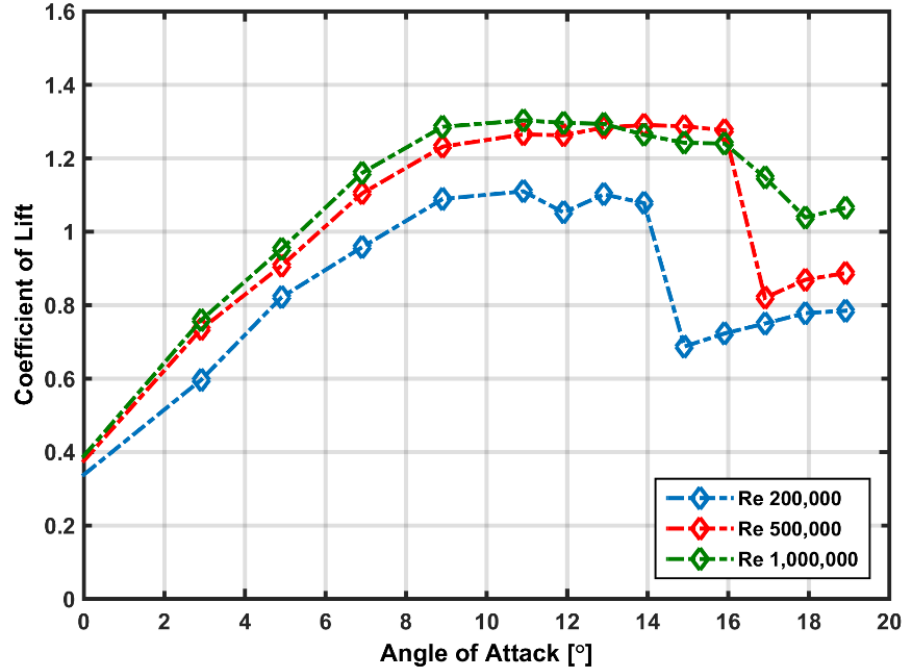
Figure 60. Variation of lift coefficient Cl versus angle of attack α for different Reynolds numbers

The stalling characteristics of the subject airfoil can be classified as trailing edge stall according to McCullough and Gault [39]. Massive separation on this type of stall is preceded by bubble-bursting37,38 where the laminar separation bubble grows right before the stall angle39,40. The presence of laminar separation bubbles at pre-stall angles of attack can be seen in surface oil flow visualization images presented in Fig.7. As is evident from examination of Figure 61, the length of the laminar separation bubble is smaller at higher Reynolds numbers and the reattachment location is further downstream at lower Reynolds numbers. At approximately %3 of the chord length at Re = 500,000 on the onset of stall, the laminar separation bubble on VR-7 airfoil at test condition is

83

certainly small but to install the actuators and examine the effects of flow control at pre-stall angles of attack (not reported here) it was decided to have the discharge, which forms at the edge of the exposed electrode, downstream of the reattachment location. Figure 61 (i) shows the case of separated flow over the airfoil. The separation location is approximately 3 mm downstream of the leading edge in this case.
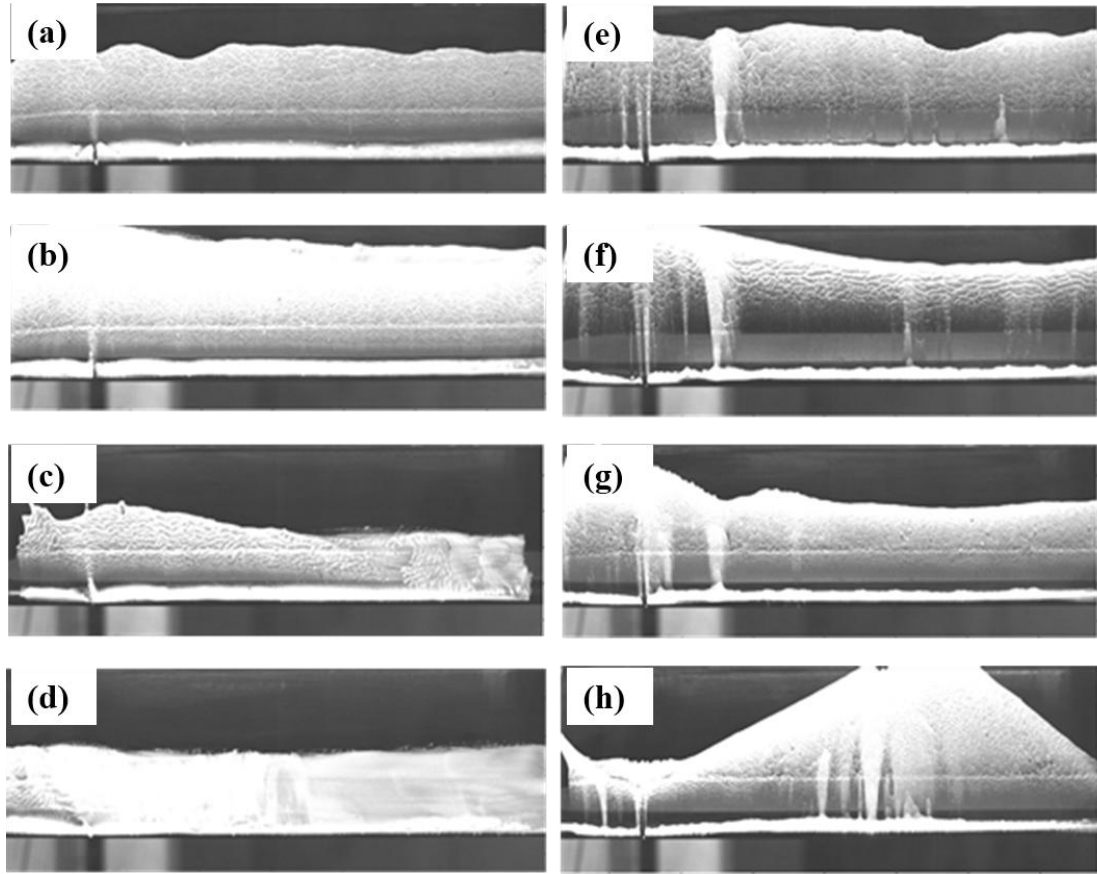
Figure 61. Surface oil flow visualization at $Re = 0.5 \times 10^6$ and (a) $\alpha = 10°$ (b) $\alpha = 12°$ (c) $\alpha = 14°$ (d) $\alpha = 16°$ - $Re = 1.0 \times 10^6$ and (e) $\alpha = 10°$ (f) $\alpha = 12°$ (g) $\alpha = 14°$ (h) $\alpha = 16°$
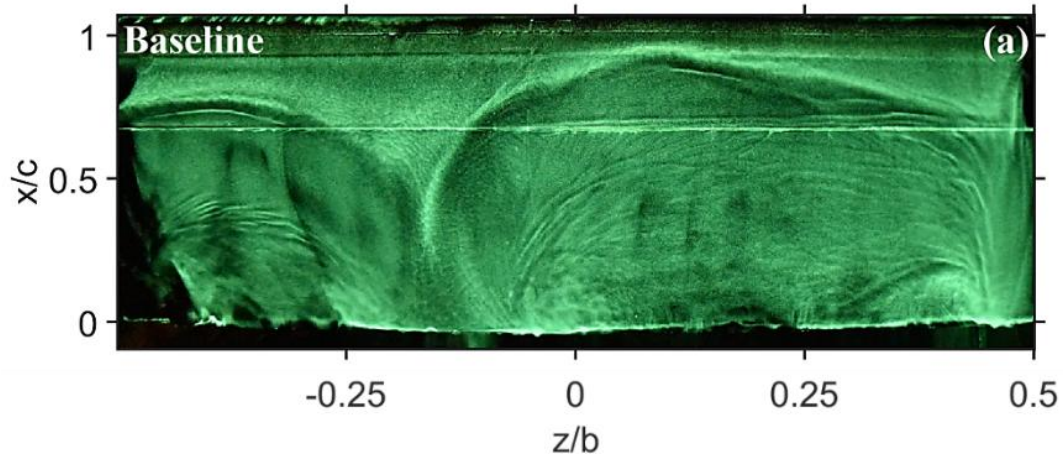
Figure 62. Fluorescent surface oil flow visualization at $\alpha = 19°$ and $Re = 0.5 \times 10^6$

Particle image velocimetry was used to obtain total velocity map over the stalled airfoil at $\alpha = 19°$. As is evident from the examination of Figure 63, at this this angle of attack and a flow Reynolds number of 0.5×10^6 the flow is completely separated and forms a wake the height of which is commensurate with the projected frontal area of the airfoil. Although from the careful examination of Fig. 6 one might arrive at the conclusion that flow separates downstream of the leading edge, surface oil flow visualization experiments point to the fact that flow separates right at the leading edge. The small disparity between separation location in Figure 63 and oil flow visualization data of Figure 62 can be traced back to perspective distortion which is an artifact of using a relatively wide angle lens (35 mm) so that a larger area of the flow may be examined.
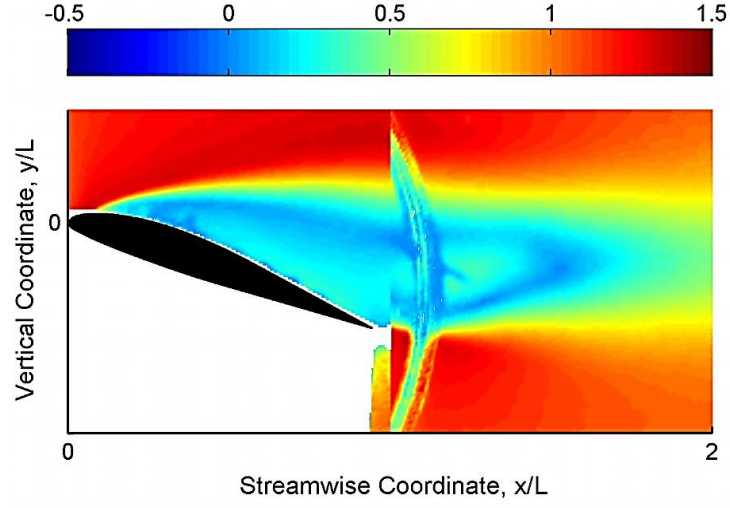
Figure 63. Map of total velocity distribution on a streamwise plane for the baseline case
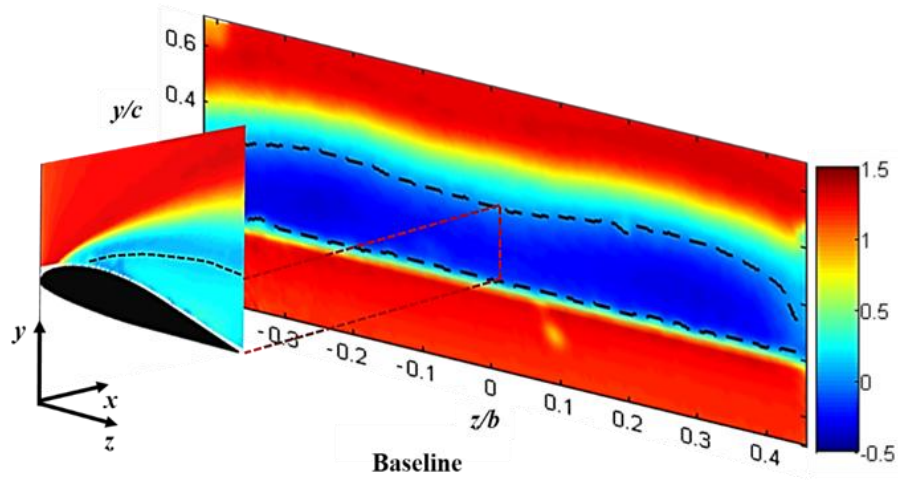
at α = 19° and $Re = 0.5 \times 10^6$

Figure 64. Comparison between maps of normalized ensemble-averaged streamwise

component of velocity u^* on a cross-stream plane at x/c =1.05 and total normalized

velocity U^* at a streamwise plane at z/b = 0.45 for α = 19° and $Re = 0.5 \times 10^6$. Dashed

black lines indicate zero velocity

86
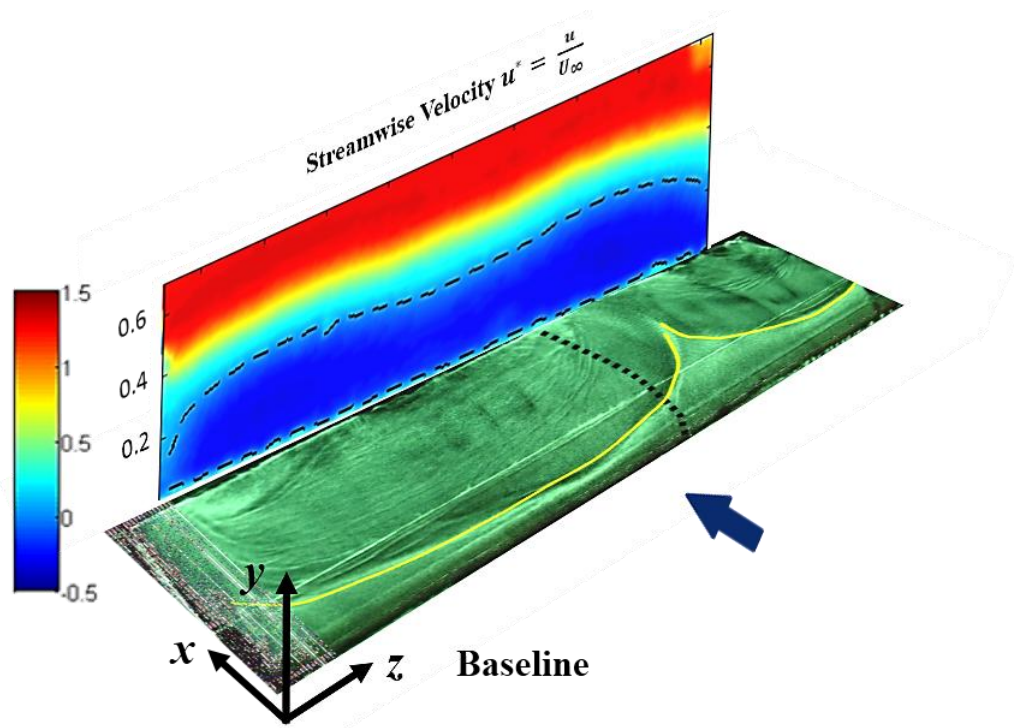
Figure 65. Comparison between maps of normalized ensemble-averaged streamwise component of velocity $u*$ on a cross-stream plane at $x/c =1.05$ and fluorescent surface oil flow visualization for $\alpha = 19°$ and $Re = 0.5\times10^6$

Microphone data were acquired with the probe located downstream of the trailing edge to characterize vortex shedding in the wake. A well-defined, narrow-band peak at $St = 0.6$ and a harmonic with a smaller amplitude at $St = 1.2$ can be readily seen in Fig. 8. The nature of peak observed at $St = 0.6$ points to the fact that at the test conditions, strong and coherent vortices are shed into the wake with the corresponding natural shedding frequency of 109 Hz. This is can also be confirmed by examining swirling strength plots obtained by pressure-based phase-locked PIV data. To illustrate the development of coherent structures and merging, high-resolution phase-locked data was acquired for the baseline case at 12 phases. A microphone is placed in the wake (as done for the fluctuating pressure spectra) to be used as a reference for the phase-locking. Figure 67 shows the non-dimensionalized swirling strength for the baseline case. As indicated in the figure, there is clear vortex shedding at the trailing edge. There are structures formed at the leading edge, but these structures are nearly not as dominate as the trailing edge structures. Although not immediately clear, there is vortex merging seen at $\phi = 0 °$, 30° and 60°.
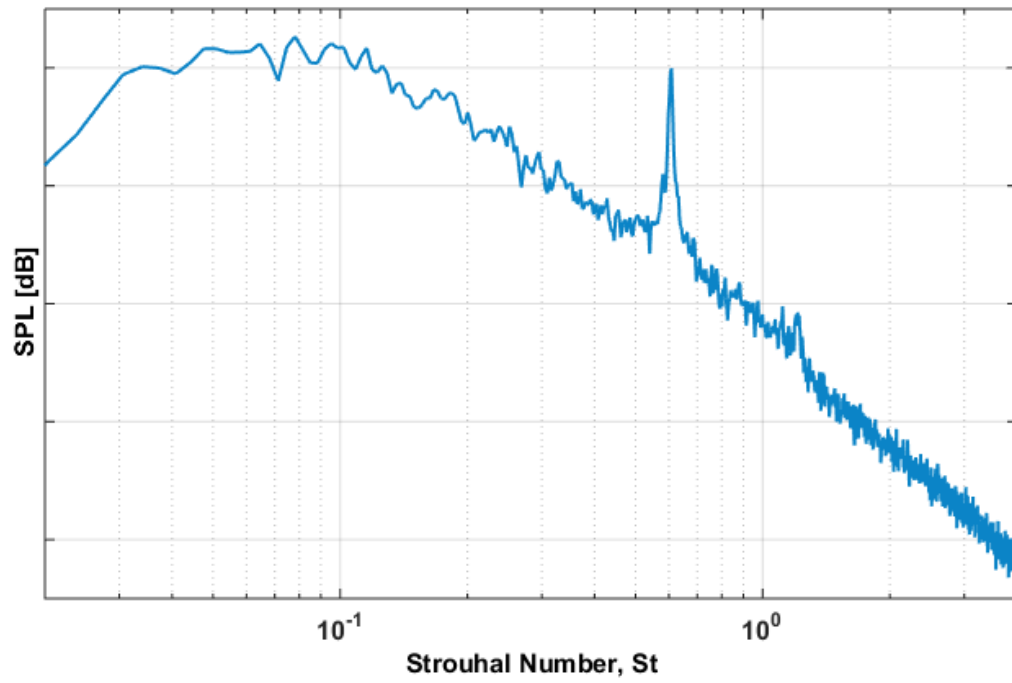
Figure 66. Wake frequency spectrum for the baseline model at α = 19° and $Re = 0.5 \times 10^6$
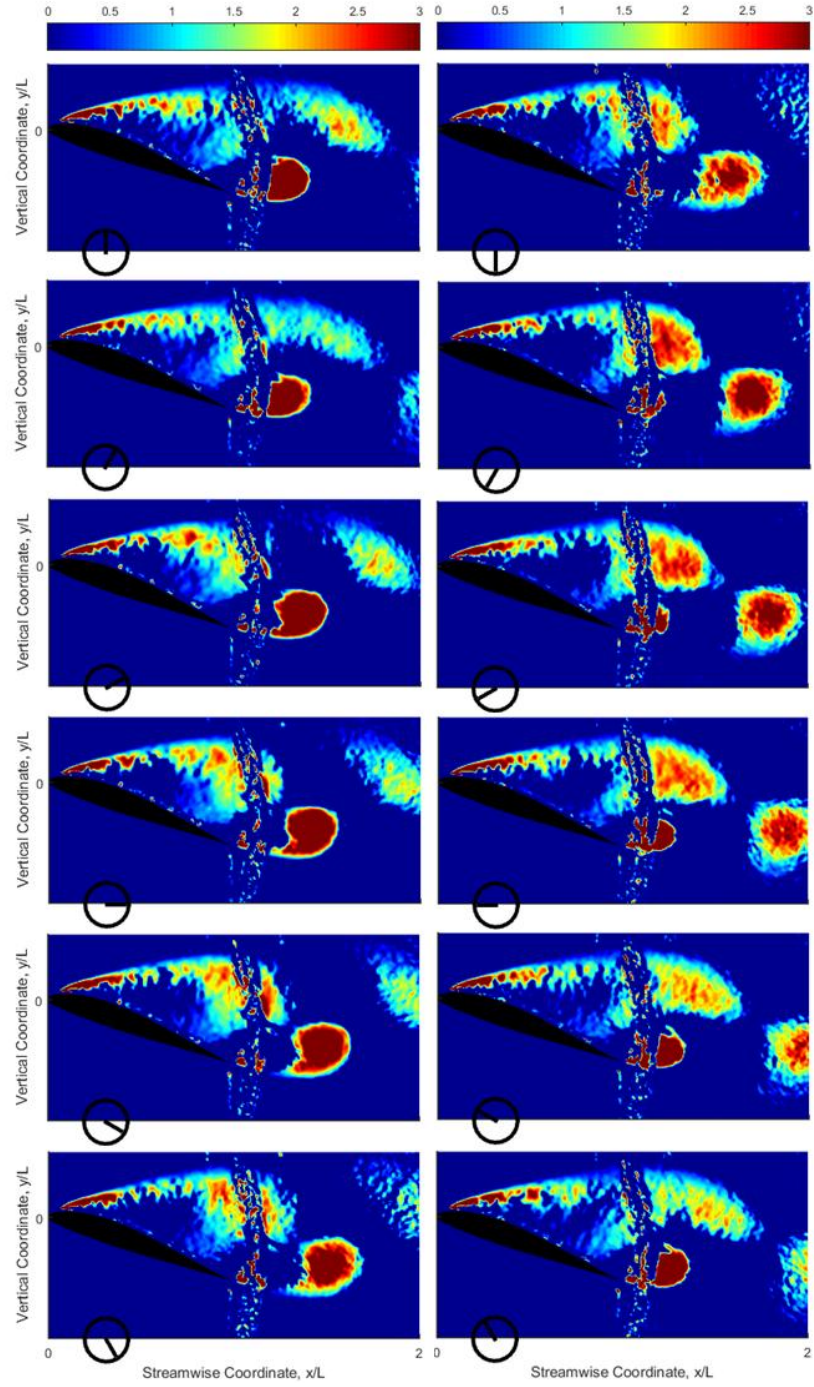
Figure 67. Non-dimensionalized swirling strength, λ_{ci}* for $St_e = 0$ (baseline) – phases

ordered from top to bottom

In contrast to the excited cases where the roll-up and downstream convection of the spanwise coherent structures is registered by the pressure taps, the roll-up of the separated shear layer at the trailing edge, as seen in Figure 67, is not registered by the pressure taps close to the leading edge in the time history of pressure coefficient plotted in Figure 68. There are, however, some minor variations in pressure coefficient along the chord in time that can be attributed to the streamwise convection of smaller structures. The signature of these structures has been registered as a peak around $St_e = 1.2$ in the pressure spectra of Figure 66.
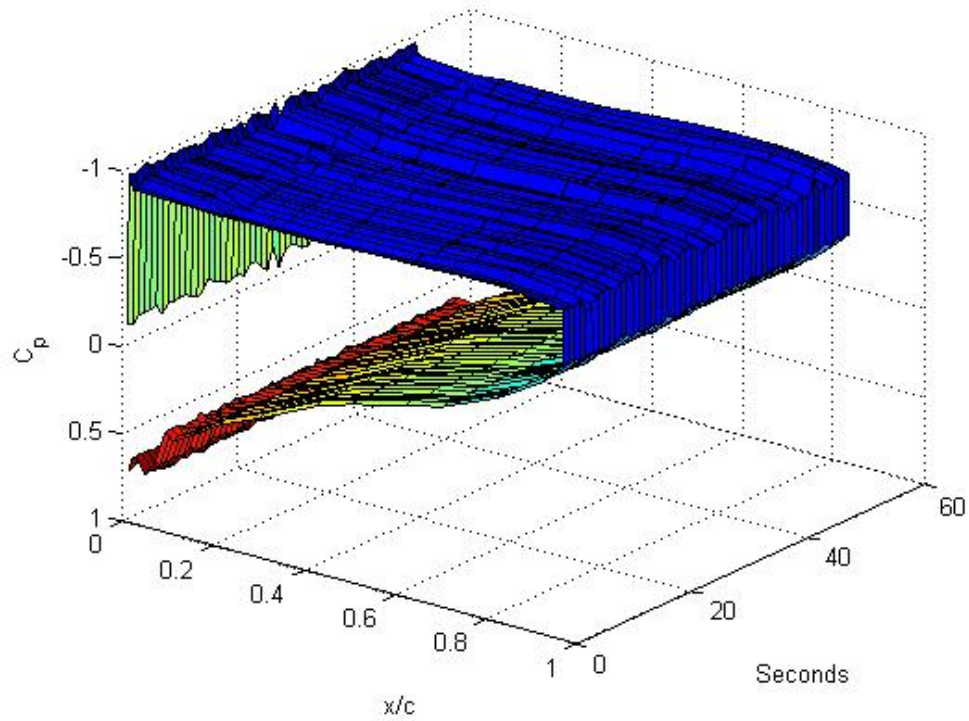
Figure 68. Variations in pressure coefficient for the baseline case in time

91

4.2 Effects of Low vs High-Frequency Excitation of the Flow

As was mentioned earlier, one of the main goals of this study is to investigate the flow response to excitation at higher Strouhal numbers than reported in the literature on NS-DBD actuators and ascertain whether the same effects reported by Amitay and Glezer [33] and Glezer et al. [34] could be achieved on a thin airfoil. The flow response to a wide range of excitation Strouhal numbers was explored using optical diagnostics, surface pressure measurements and wake spectra from microphone measurements. Due to the different effects observed at different ranges of excitation frequencies, these regimes are broken into the following categories:

    a. Low-frequency excitation regime ($St_e < 2.0$) where the flow field is relatively two-dimensional in the spanwise direction and the airfoil experiences unsteady loads due to shedding of dominant, large-scale coherent structures.

    b. Mid-frequency excitation regime ($2.0 < St_e < 6.0$) where some of the distinct features of the low-frequency excitation regime, such as generation and shedding of coherent structures, although smaller in size, are still present but some of the defining hallmarks of the high-frequency excitation regime, namely the progression of the separation line in the downstream direction and emergence of the three-dimensional flow features, are starting to emerge.

c. High-frequency excitation regime ($St_e > 6.0$) where three dimensional features in the form of well-defined stall cells are present. The spanwise rollers observed in the low-frequency excitation regime are no longer generated and are in fact, replaced by numerous small-scale structures that play the same role. The separation line is pushed further back in the streamwise direction and the airfoil no longer experiences unsteady loads due to periodic shedding of coherent structures into the wake.

To explore and contrast the excitation regimes delineated above, the data will be presented in the following order. First, streamwise time-averaged velocity fields and the data extracted from those distributions, for baseline and various excited cases will be presented. Then, phase-locked PIV data acquired in streamwise and spanwise planes, depicting the development of coherent structures and separation line unsteadiness or lack thereof, will be presented. Finally, wake spectra obtained from microphone measurements and surface pressure data will be examined to complete the picture. The three-dimensional flow features, mentioned earlier, will be addressed in a separate section.

4.2.1 Time-averaged Flow Field Data

Time-averaged total velocity fields over the airfoil and in the wake region under the effect of excitation are compared with the baseline flow field in Figure 69. As mentioned by McAlister[66] and McAlister and Tung[67] , the VR-7 airfoil, despite being

considered a thin airfoil, demonstrates a trailing edge separation. The separation line progressively moves upstream as the angle of attack is increased beyond the stalling angle of 16° at $Re = 0.50{\times}10^6$. The 3-D separation front for the baseline case, as seen in the oil flow visualization data , is approximately located at $x/c = 0.2$.   The reduction in separation size with an increase in forcing frequency is readily evident in Figure 69b to f. as the separation line is pushed back to $x/c = 0.5$ for $St_e = 4.27$. It is interesting to note that forcing at $St_e > 0.78$, would confine the low-speed recirculating flow region close to the airfoil surface. This can be attributed to better momentum transfer across the separated shear layer, brought about by numerous small-scale structures, as a result of excitation at relatively higher frequencies which effectively reduces momentum deficit in the wake. Exciting the flow at natural shedding frequency brings about the most noticeable reduction in the cross-stream extent of the wake.

Increasing the excitation frequency to $St_e = 2.06$ and 4.23 progressively moves the separation location further downstream as the frequency is increased. The regions with darker shades of red close to the leading edge for these excitation frequencies (Figure 69e and f) indicate that flow is highly accelerated in this area. Given the centrifugal acceleration needed to attach the flow around a leading edge with a small radius of curvature[31] it seems that excitation at $St_e = 2.06$ and 4.23, regardless of its mechanism, has resulted in generation of enough momentum in the leading edge area to bring about flow reattachment.

As will be shown in section 3, another side effect of increasing the excitation frequency beyond $St_e = 2.04$ is the emergence of 3-D features over the airfoil in the form of stall cells. The stall cells become more defined and the separation front pushed downstream as the excitation frequency is increased but the effect saturates at $St_e = 6.0$ and further increases in frequency, up to $St_e = 14.52$ seem to have no discernable effect on the flow field.

Time-averaged plots of vorticity concentrations are presented in Figure 70.
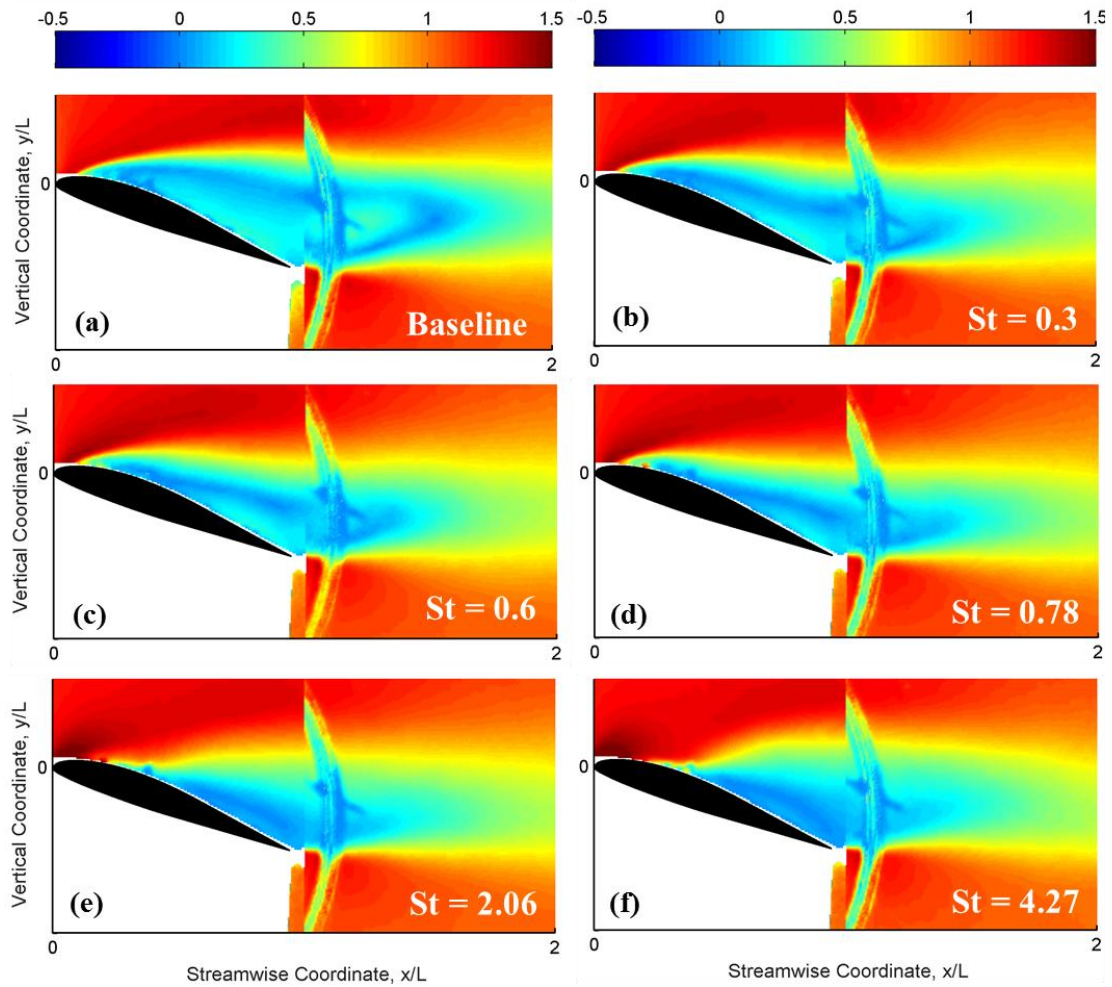
Figure 69. Time-averaged normalized total velocity at α = 19° and Re = 500,000 (a)

baseline (b) St_e = 0.3 (c) St_e = 0.6 (d) St_e = 0.78 (e) St_e = 2.06 (f) St_e = 4.27

Figure 70. Time-averaged plots of non-dimensional vorticity $\boldsymbol{\omega}^*$ at $\alpha = 19°$ and Re = 500,000 (a) baseline (b) $St_e = 0.3$ (c) $St_e = 0.6$ (d) $St_e = 0.78$ (e) $St_e = 2.06$ (f) $St_e = 4.27$

For the baseline case at test conditions, where strong coherent structures are shed into the wake, concentrations of CW vorticity above leading edge, where the shear layer separates, and downstream of the trailing edge are noticeable but there no vorticity concentrations immediately adjacent to airfoil surface. It should be noted that the well-defined CW vorticity layer extends far downstream even beyond the airfoil trailing edge which indicates vortices convected downstream maintain their coherence well beyond the trailing edge and breakdown at a location downstream of the trailing edge. As the flow is forced at the sub-harmonic of the natural shedding frequency ($St_e = 0.3$) the concentration of CW vorticity begins to move closer to the airfoil's surface.

This is best illustrated by comparing the vorticity plots for the baseline case and forcing at the natural shedding frequency. As mentioned before, these observations can be explained through the mechanism of forcing at Strouhal numbers of $O(1)$. Forcing at such frequencies triggers flow instabilities that generate large scale structures that are effective in bringing thick concentrations of CW vorticity closer to the airfoil surface.

As such, it is evident that forcing at $St_e = 0.3$, 0.6 and 0.78 tilts the separated shear layer towards airfoil surface as expected and previously reported in a broadly similar configuration by Amitay and Glezer[33]. It is also interesting to note that forcing at $St_e = 2.06$ and 4.27 leads to shedding of smaller CCW vorticity concentrations into the wake and weakening of CW vorticity concentrations downstream of the leading edge. This indeed might be the reason for the phase lag that is observed in phase-locked data and time-averaged total velocity plots.

In conclusion, it seems that forcing at frequencies higher than natural shedding frequency would lead to weakening, loss of coherence and early breakdown of spanwise oriented vortices generated downstream of leading edge. Another notable aspect is the persistence of diffuse CW vorticity concentrations into the wake when flow forced at $St_e = 2.06$ and 4.27 which again is indicative of better mixing in these conditions as a result of early breakdown of coherent structures. It is also interesting to note that the cross-stream width of the separated shear layer decreases as the excitation frequency is increased and the outer edge of the shear layer becomes almost parallel to the incoming free-stream flow. Glezer et al.[34] believe that this condition marks the absence of oscillations due to shedding of large-scale structures.

4.2.2   Phase-locked Flow Field Data

In order to illustrate the development of coherent structures and merging under the effect of actuation by NS-DBD actuators, phase-locked data were acquired for the baseline and various excited cases in streamwise and spanwise planes. Phase-locked data for the baseline case was presented in section 4.4.1. For the excited cases, the actuator signal is used as the trigger signal. The period between excitation pulses in broken down into 8 or 12 phases in what follows.

When the flow is excited at the low-frequency excitation regime, not only the development of the coherent structures is expedited due to injection of energy but also their strength is increased as well. This can be seen in plots of swirling strength for various excitation frequencies at $\varphi = 0°$ in Figure 71. Compared to the baseline case, the shear layer starts to roll-up earlier upstream and the strength of the vortices has significantly increased. The wavelength and spacing of the vortices decreases continuously as the excitation frequency is varied between $St_e = 0.6$ and $St_e = 6.0$. When the flow is excited at $St_e = 0.6$, only one rolled up vortex can be seen over the airfoil but excitation at the second harmonic of the natural shedding frequency ($St_e = 1.20$), generates two vortices over the airfoil with their cores located at $x/c = 0.3$ and 0.7. These observations clearly demonstrate how doubling the frequency halves the wavelength of the generated structures. The same trend continues with forcing at $St_e = 2.4$ with the vortex cores located at $x/c = 0.1, 0.3, 0.6$ and 1.0, respectively. By stepping into the high-frequency excitation regime via increasing the excitation frequency to $St_e = 6.0$, the

100

structures become so small that it would be difficult to resolve and differentiate them from background noise.

The expedited development and eventual breakdown of the coherent structures has important implications for separation control. The earlier breakdown of vortical structures as is seen in Figure 71c at $x/c = 0.7$, means that the coherent structure is no longer capable of harvesting momentum from the freestream downstream of the breakup point and as a result flow reattachment would not be possible downstream of the breakup point. By examining Figure 71d closely, one would notice from the vortex trajectory that the flow remains attached up to $x/c = 0.4$, which is consistent with time-averaged velocity maps of Figure 69e and f. As mentioned earlier, injecting energy into the flow expedited the development of coherent structures. This is quite evident from the recession of the breakup point in the upstream direction starting with $x/c = 1.0$ for $St_e = 0.6$ and going all the way back to $x/c = 0.4$ for $St_e = 6.0$. The implication would be that excitation at the low-frequency regime would create modest suction peaks over the entire chord of the airfoil due to the convection of the coherent structures over the airfoil whereas high-frequency excitation would lead to creation of strong suction peaks only close to the leading edge due to the early breakup of small-scale vertical structures. These effects are also reflected in surface pressure data and will be further discussed in section 4.2.4s.
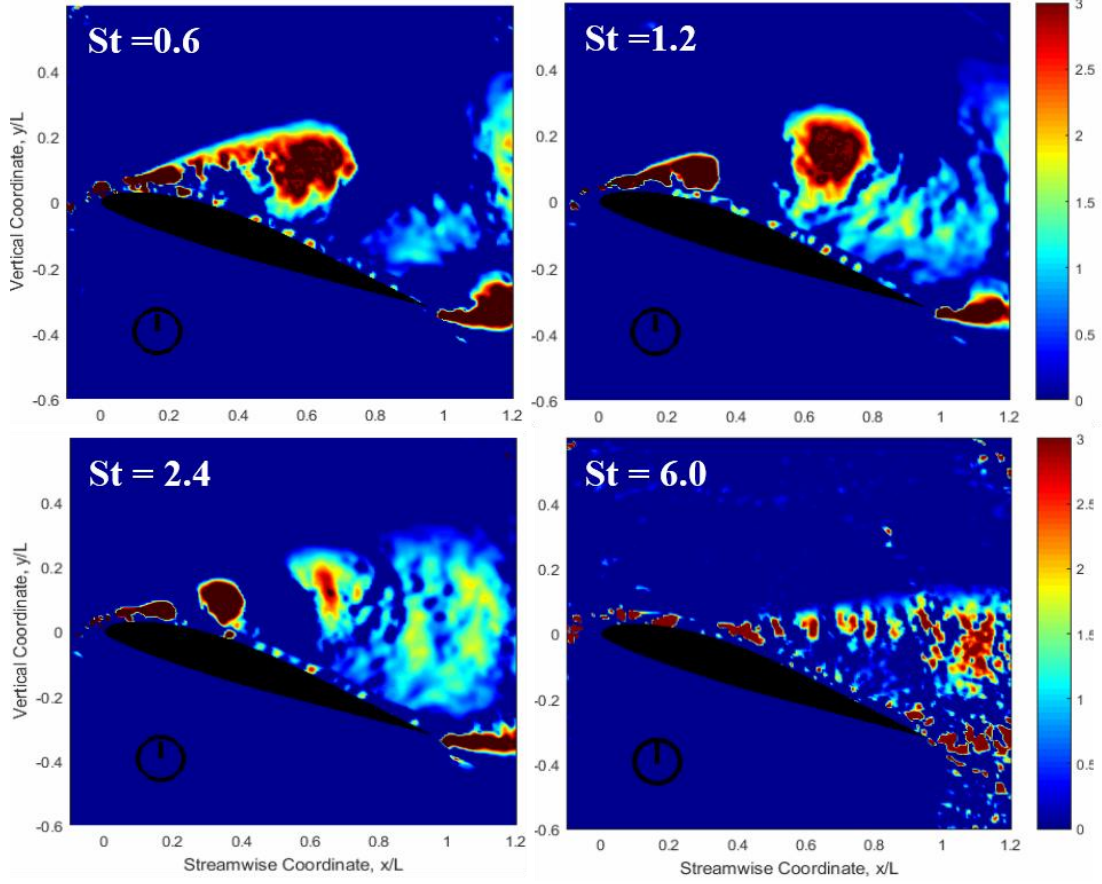
Figure 71. Reduction in the size of coherent structures as a result of increase in excitation

frequency at α = 19° and Re = 0.5×10⁶

In order to highlight the differences between the two excitation regimes explored in this paper two specific cases, namely St_e = 0.6 and St_e = 6.0, representing each excitation regime will be presented and studied in detail. Figure 73 depicts the phase-locked data acquired for St_e = 0.6 at a streamwise plane while Figure 74 shows the data acquired for the same case in a spanwise plane downstream of the trailing edge. Compared to the baseline case presented in Figure 67 the shear layer rolls up earlier and the vortices start

to disintegrate upstream of the trailing edge due to energy injection. The white line, seen in Figure 73, corresponds to zero velocity and its intersection with the airfoil surface denotes the separation line location. It would be interesting to note that the separation line moves progressively in the downstream direction as the leading-edge vortex convects downstream (Figure 73, $\varphi = 0°$ - 225°). Once the vortex moves past the trailing edge and is shed into the wake, however, the separation location retreats in the upstream direction (Figure 73, $\varphi = 270°$). As is the case in this excitation regime, the periodic shedding of large-scale structures would apply unsteady loads to the airfoil which might lead to fatigue in the long term. This process can be further illustrated by examining the maps of normal velocity distribution acquired in a spanwise plane downstream of the trailing edge.

Examining $\varphi = 0°$ - 180° in Figure 74, one can notice the lighter shades of red and blue indicating momentum diffusion and transport across the separated shear layer due to the downstream convection of strong, spanwise rollers. The same time, the separation height, inferred from the dotted lines indicating zero velocity, is progressively reduced until $\varphi =$ 180°. As the spanwise roller passes through the laser sheet at $\varphi = 225°$ (Figure 73 and Figure 74, the magnitudes of the in-plane, total velocity vectors suddenly increase. This is further corroborated by spanwise maps of the normal component of velocity in Figure 75. Comparing the streamwise data of Figure 73 with Figure 75, it is readily evident that the light shades of red indicating the concentrations of weak normal velocity components are actually due to the roll-up and shedding of vortices from trailing edge. As the trailing

vortex is convected downstream (φ = 0° - 135°), the large-scale structure that has rolled up close to the leading edge starts to approach the laser sheet at x/c = 1.05 and as a result, the magnitude of the normal component of velocity keeps increasing until the vortex comes right through the laser sheet at φ = 225°. Immediately after that, as the separation line begins to retreat in the upstream direction (φ = 270° - 315°), the magnitude of the normal components begins to subside.

As will be shown in the following section, surface oil flow visualization results indicate that under excitation at St_e = 0.6, two asymmetric stall cells are present on the suction side of the airfoil. That, normally, indicates that the velocity distribution across the span might not be two-dimensional. As can be seen in Figure 74, that is not the case as a nearly two-dimensional distribution exists above the airfoil throughout the excitation cycle. This can be explained if one considers the possibility of an interaction between strong spanwise rollers and the streamwise vortex lines, the signature of which was recorded by SOFV. It is possible that the streamwise vortex lines, responsible for distorting the spanwise velocity distribution, have been pushed down by the shedding and convection of strong coherent structures that are generated by low-frequency excitation. This point will be further examined in section 4.3.
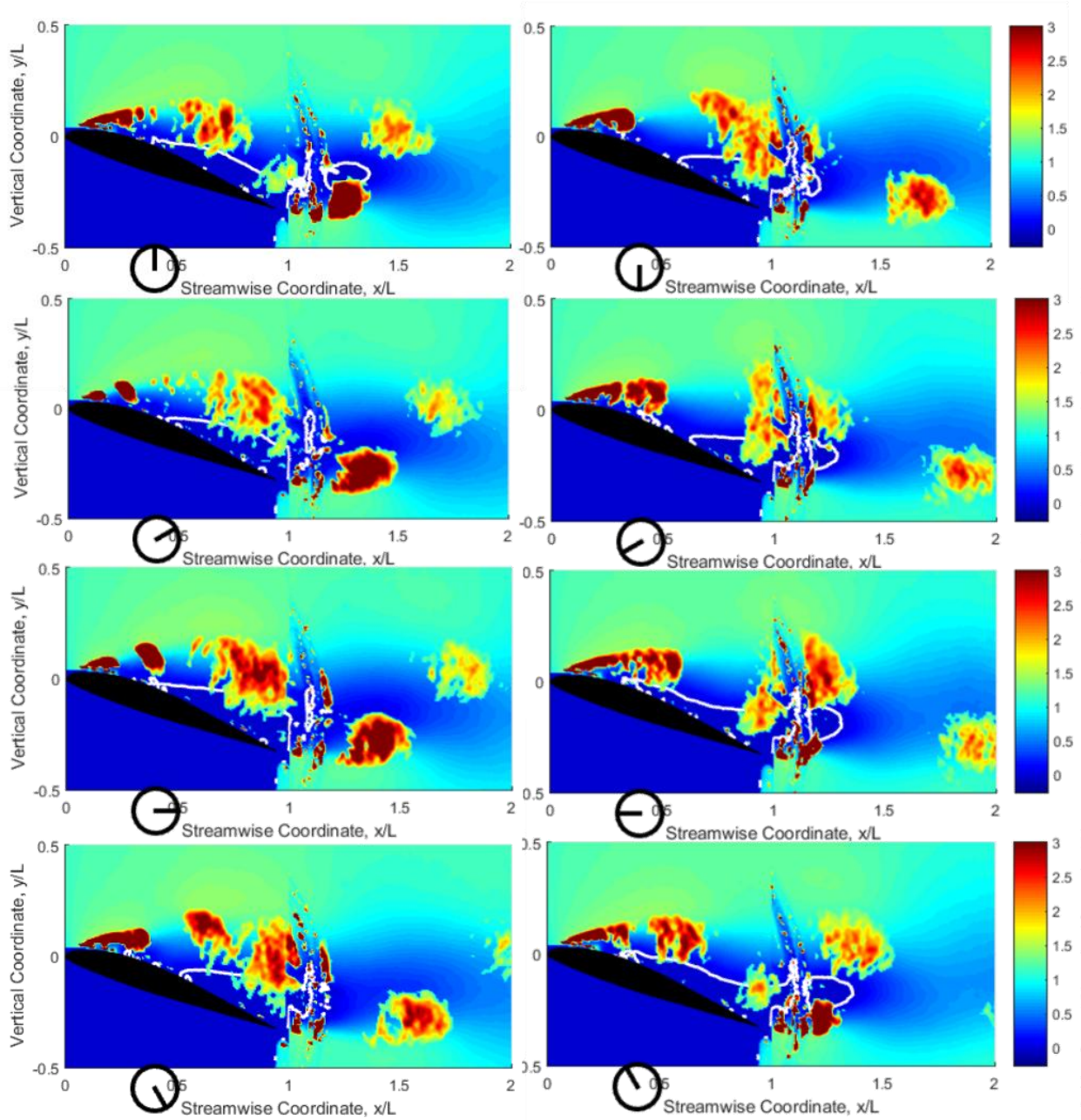
Figure 72. Iso-lines of zero velocity plotted over normalized streamwise velocity and swirling strength, λ_{ci}^* maps for excited flow ($St_e = 0.6$) at $\alpha = 19°$ and Re $= 0.5 \times 10^6$
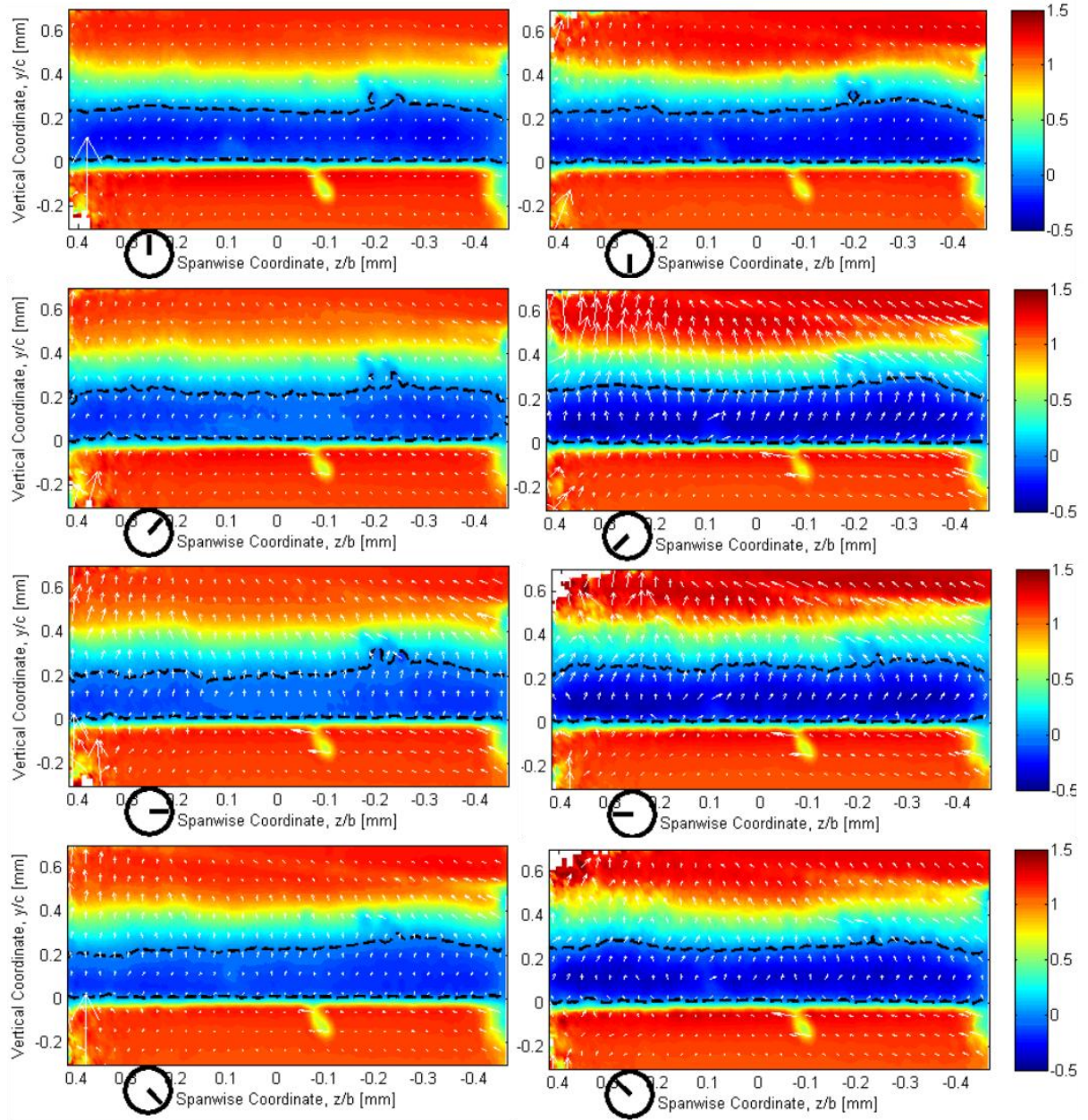
Figure 73. Color maps of normalized phase-averaged streamwise component of velocity on a cross-stream plane at x/c =1.05 superimposed on total, in-plane velocity vectors for α = 19° and Re = 0.5×10⁶ at St_e = 0.6 acquired in 8 phases φ during excitation period.

Total in-plane velocity vectors are plotted over color maps normal velocity magnitude in Figure 75. Upon examining Figure 75, it is readily evident that the light shades of red indicating the concentrations of weak normal velocity components are actually due to the roll-up and shedding of vortices from trailing edge. As the trailing vortex is convected downstream ($\varphi = 0°$ - $135°$), the large-scale structure that has rolled up close to the leading edge starts to approach the laser sheet at $x/c = 1.05$ and as a result, the magnitude of the normal component of velocity keeps increasing until the vortex comes right through the laser sheet at $\varphi = 225°$.

The position of the vortex passing through the light sheet agrees with the streamwise data of Figure 73. Immediately after that, as the separation line begins to retreat in the upstream direction ($\varphi = 270°$ - $315°$), the magnitude of the normal components begins to subside. At the same time, the separation height, inferred from the dotted lines indicating zero velocity, is progressively reduced until $\varphi = 180°$. As the spanwise roller passes through the laser sheet at $\varphi = 225°$ in Figure 74 and Figure 75, the magnitudes of the in-plane, total velocity vectors suddenly increase.
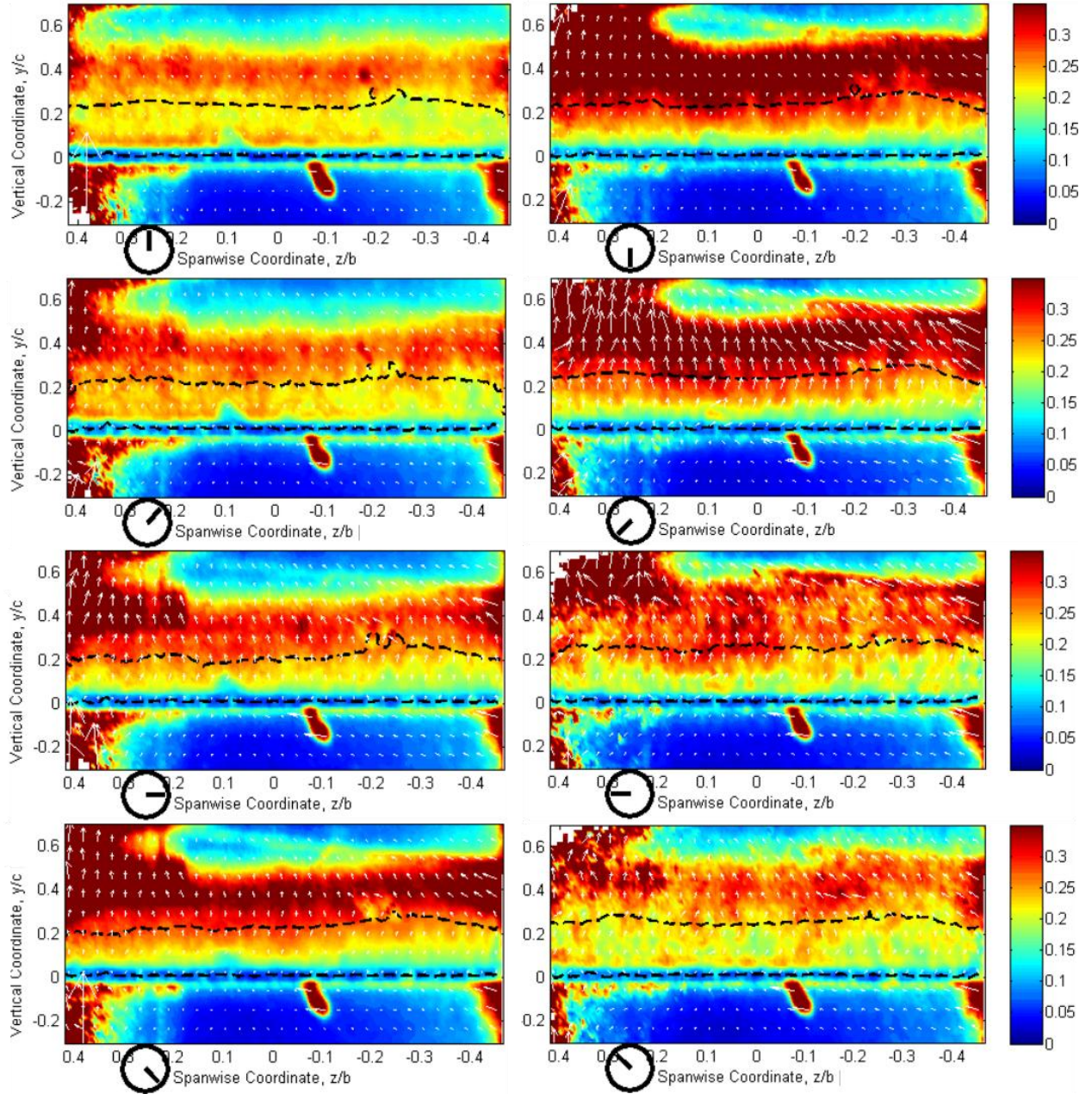
Figure 74. Color maps of normalized phase-averaged normal component of velocity on a cross-stream plane at x/c =1.05 superimposed on total, in-plane velocity vectors for α = 19° and Re = 0.5×10^6 at St_e = 0.6 acquired in 8 phases φ during excitation period.

The phase-locked maps of swirling strength, depicting the development of flow field under the effect of excitation at the high-frequency excitation regime, are plotted in Figure 76. Due to the smaller size of the structures generated due to excitation, a longer focal length was used in order to increase magnification and use as much of the sensor area as possible to resolve the small-scale structures. The small size of the structures, however, means that it is difficult to track and resolve individual vortices using the 4-megapixel camera used in experiments reported in this work. As can be seen, in contrast to the low-frequency regime, the separation line inferred from the intersection of zero velocity line with the airfoil surface remains stationary between individual pulses. This can largely be attributed to the absence of large, coherent structures. The absence of unsteadiness at high-frequency excitation regime indicates that unlike lower frequency excited cases, the airfoil will not experience unsteady loads and periodic separation and partial reattachment.

The spanwise data of Figure 77 confirm that the flow field under excitation at high frequencies would be time invariant. The time-invariant interaction between the actuator and the flow at the high-frequency excitation regime leads to what Glezer et al. refer to as virtual shaping[37]. Spanwise colormaps of normal velocity with overlaid total, in-plane vector fields are presented in Figure 78. The magnitude of the normal velocity component in addition to separation height across the span are constant between individual pulses and no significant changes in either direction or magnitude of the in-plane vectors can be seen. The shape of the zero-velocity line suggests that two well-defined stall cells are

109

present over the airfoil at $St_e = 6.0$, as was mentioned before, and it appears that the shape of the cells does not vary within the excitation cycle.

No significant vortex shedding can be detected in the data due to the early breakdown of the small-scale structures further upstream. As before, a significant level of background noise due to laser reflections from the acrylic sidewalls is present in the data (from $z/b = 0.2$ to 0.4) that could not be removed despite applying various filters to the data.
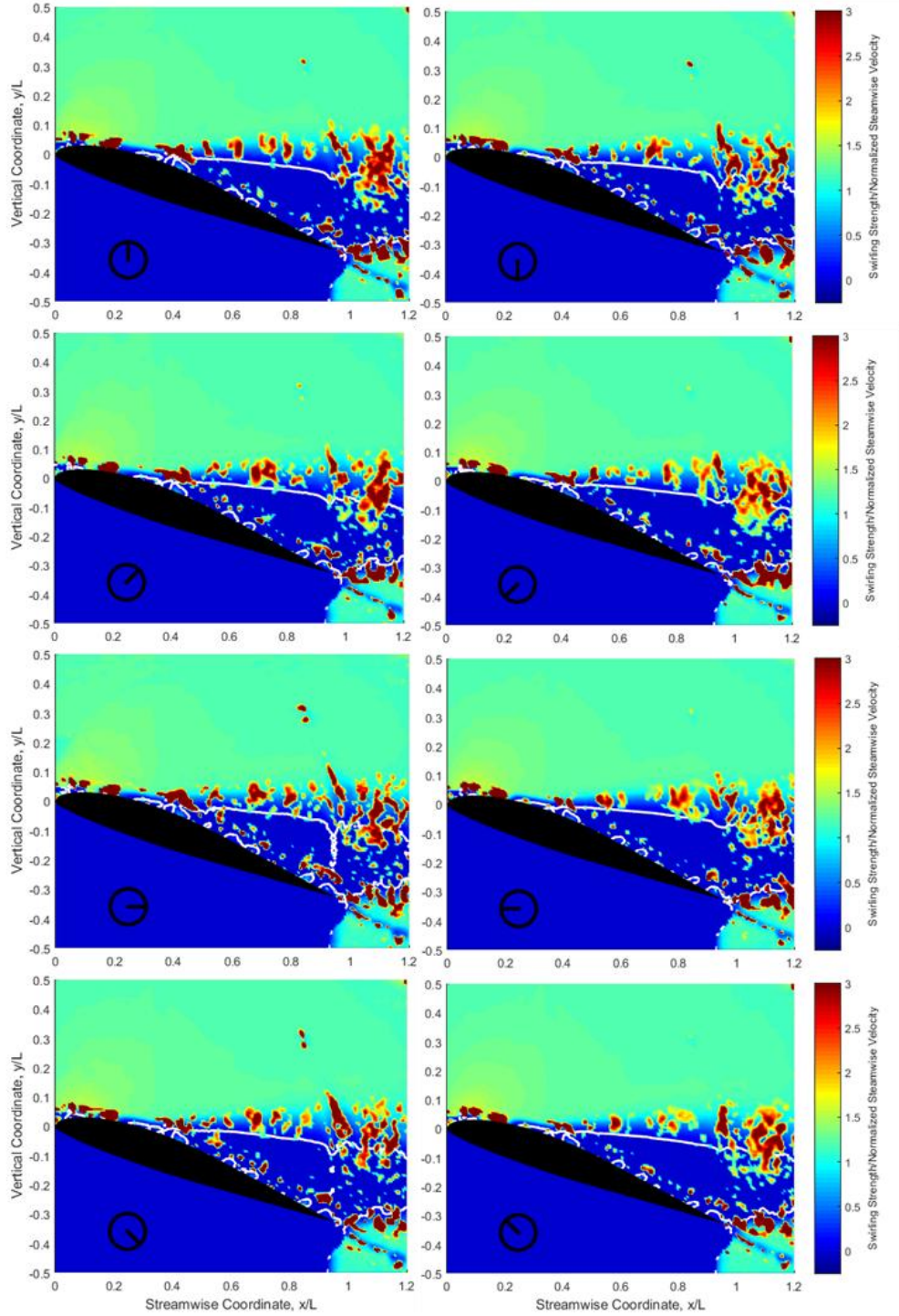
Figure 75. Iso-lines of zero velocity plotted over normalized streamwise velocity and swirling strength, λ_{ci}^* maps for excited flow ($St_e = 6.0$) at $\alpha = 19°$ and Re $= 0.5 \times 10^6$
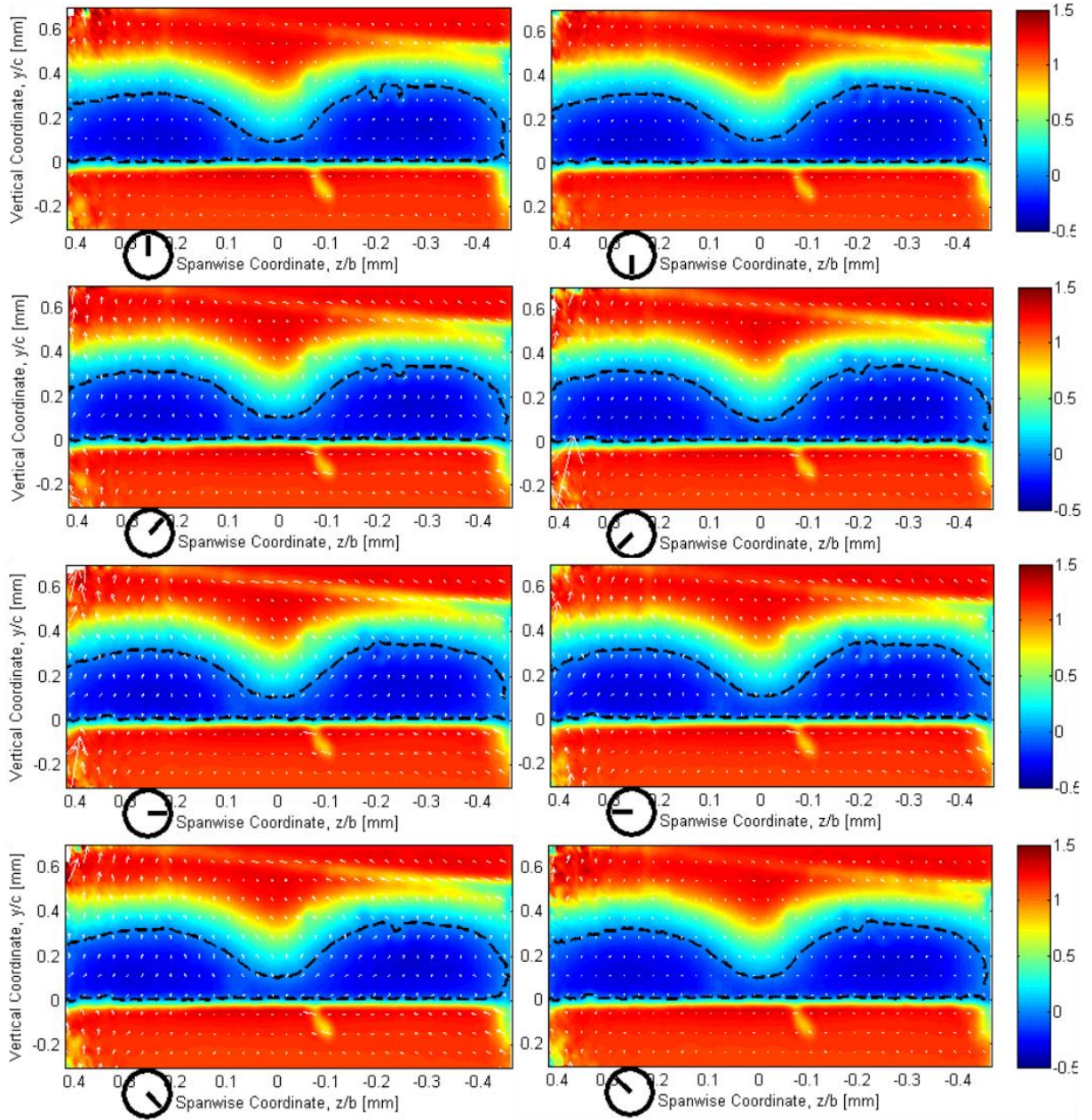
Figure 76. Color maps of normalized phase-averaged streamwise component of velocity   on a cross-stream plane at x/c =1.05 superimposed on total, in-plane velocity vectors for α = 19° and Re = 0.5×10^6 at St_e = 6.0 acquired in 8 phases φ during excitation period.
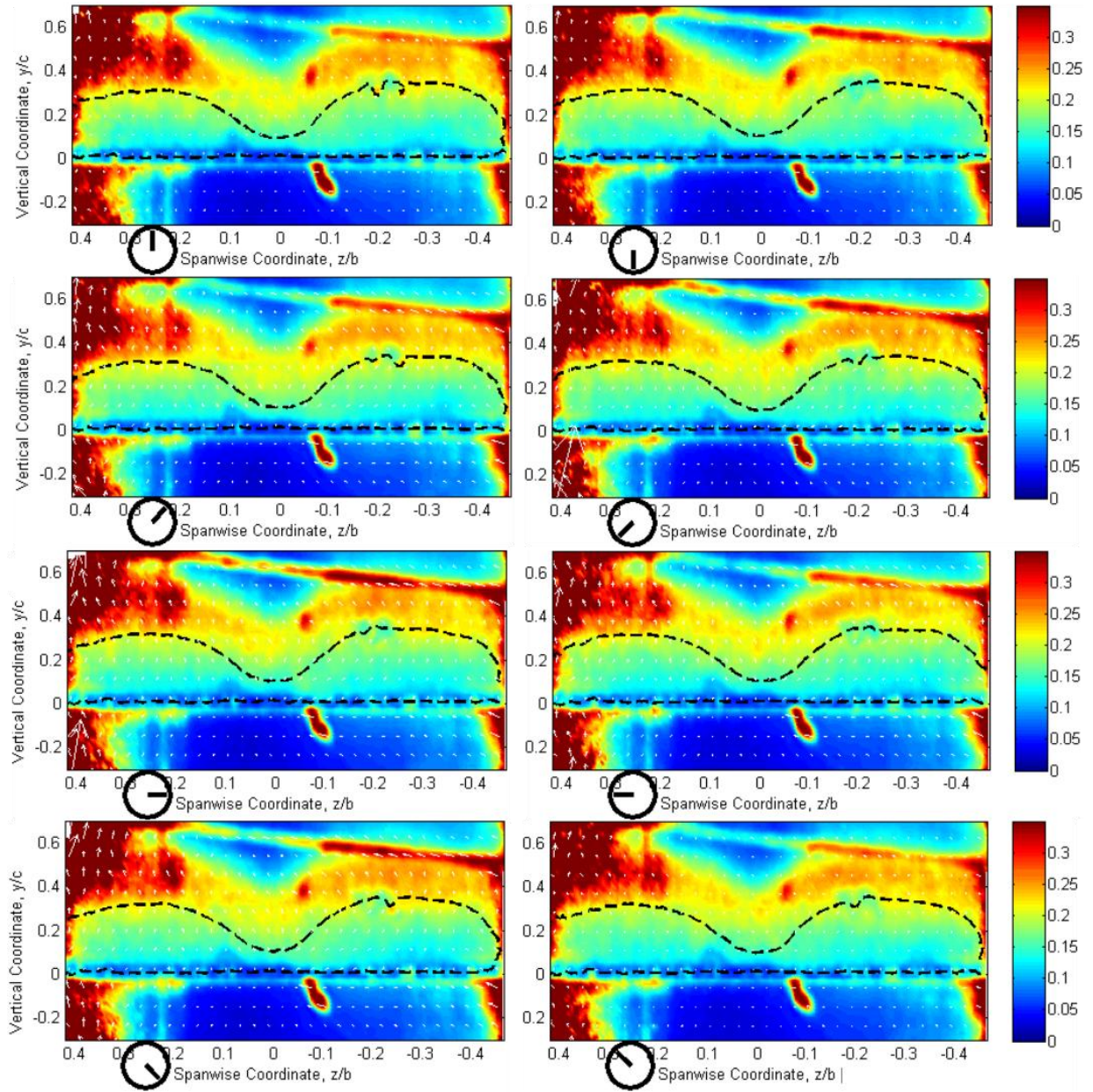
Figure 77. Color maps of normalized phase-averaged normal component of velocity on a cross-stream plane at x/c =1.05 superimposed on total, in-plane velocity vectors for α = 19° and Re = 0.5×10^6 at St_e = 6.0 acquired in 8 phases φ during excitation period.

Amitay and Glezer[33], while studying the role of actuation frequency for separation control, noted a significant decrease in the time rate of variations in the net vorticity flux shed into the wake of an airfoil with an increase in actuation frequency. A similar correlation with the excitation frequency was observed in the present work. This point can be illustrated by examining Figure 79. Here, phase-locked plots of vorticity for two phase during the shedding (baseline) or excitation cycle are presented. As the total flux of vorticity into the wake is directly proportional to the circulation around the airfoil, variations in vorticity flux during the shedding or excitation cycle would be indicative of unsteady loads. As before, concentrations of blue in the color maps indicate negative (clockwise) vorticity while positive (clockwise) vorticity is marked by red concentrations. For the baseline case, the variation in the net vorticity flux between two sample phases (φ = 150° - 330°) is small. Exciting the flow field at St_e = 0.6 leads to the coupling between excitation and the flow field and unsteady ejection of vorticity into the wake during different phases of the excitation cycle as can be seen in two phases presented in Figure 79 for St_e = 0.6. The total vorticity flux at φ = 150° has a positive value whereas the positive flux at φ = 330° is partially cancelled by the negative concentrations. In contrast, the total flux of vorticity shed into the wake of the airfoil when the flow is excited at St_e = 6.0 is time-invariant as depicted in Figure 79. As a result, the airfoil will not experience cyclic unsteady loads as was the case with low-frequency excitation. As the excitation at higher frequencies is effectively decoupled

from global effects[33] it is expected that any subsequent increase in excitation amplitude, would have minimal effects on the global flow field.
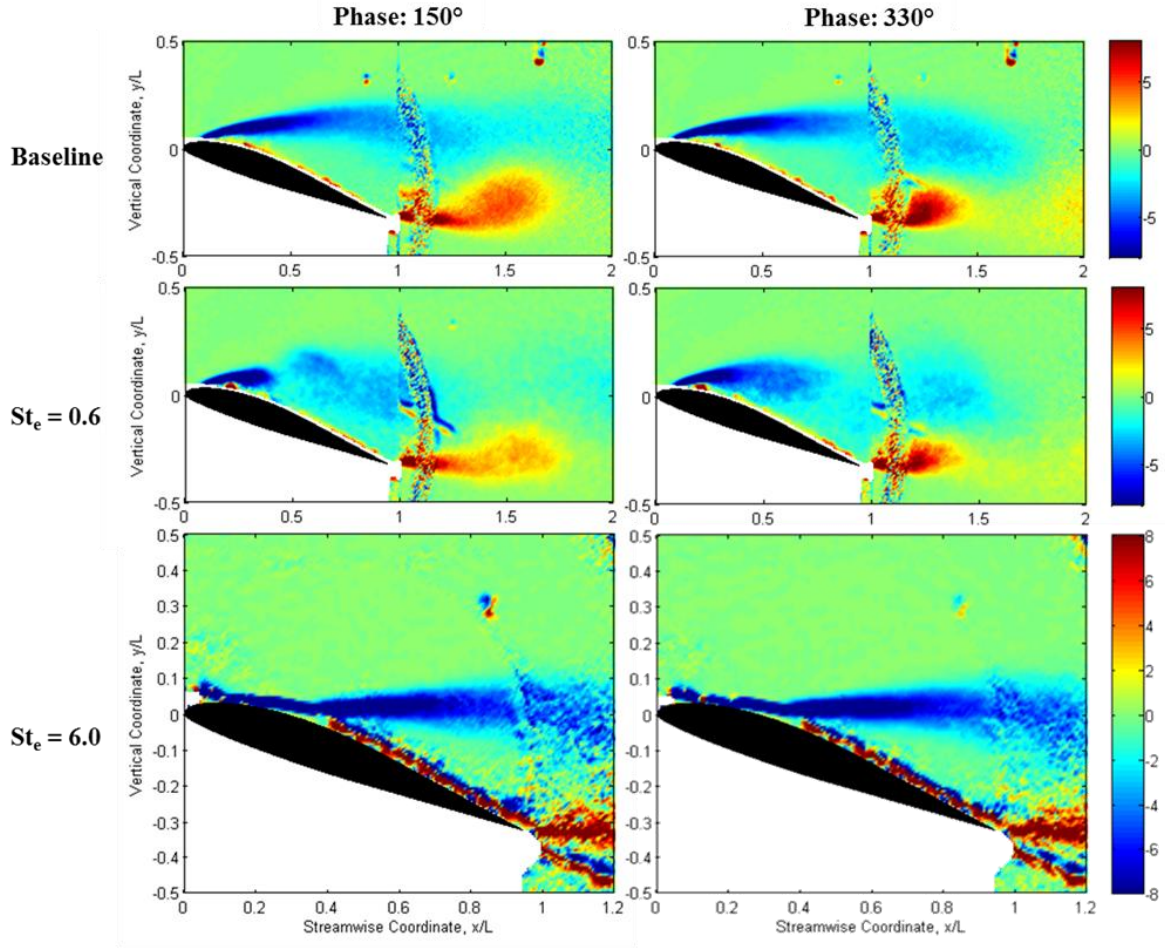
Figure 78. Phase-locked vorticity concentrations for baseline and excited

flows at different phases

4.2.3   Wake Pressure Spectra

Fluctuating pressure spectra for various low-frequency excitation cases were acquired to determine the strength of the vortex shedding, concentrations of the energy within specific frequency bands and the state of the separated shear layer. A map of vorticity distribution for the baseline case was used to determine the coordinates of points, along the edge of the shear layer, that were needed for positioning the microphone. The spatial distribution of these points can be seen in Figure 79.
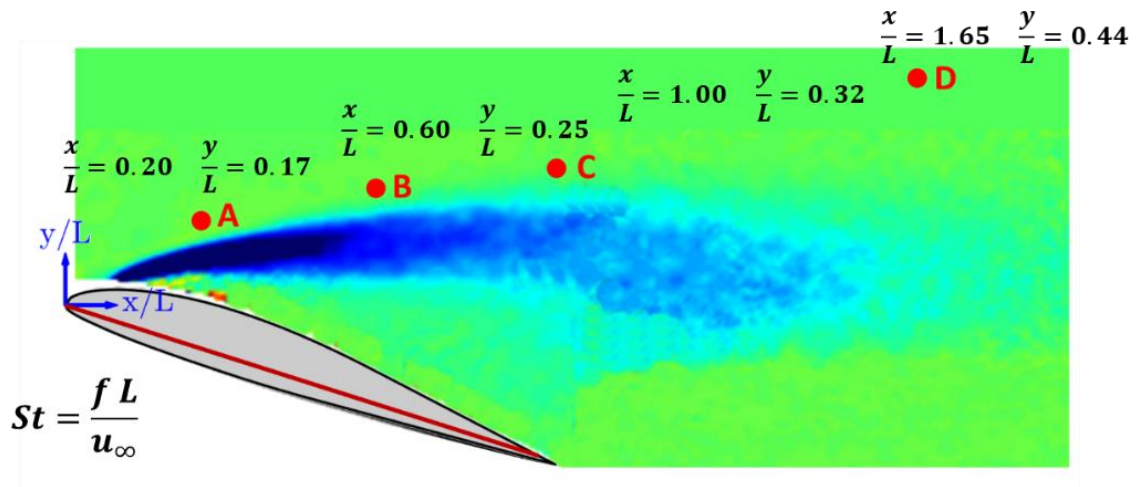
Figure 79. Microphone locations for measurements along the edge of shear layer

To study the shedding of vortices into the wake due to excitation, the microphone was positioned at point D (*x/c*=1.65 and *y/c* = 0.44) and data were acquired for various excitation regimes. The low to mid-frequency spectra are presented in Figure 80.
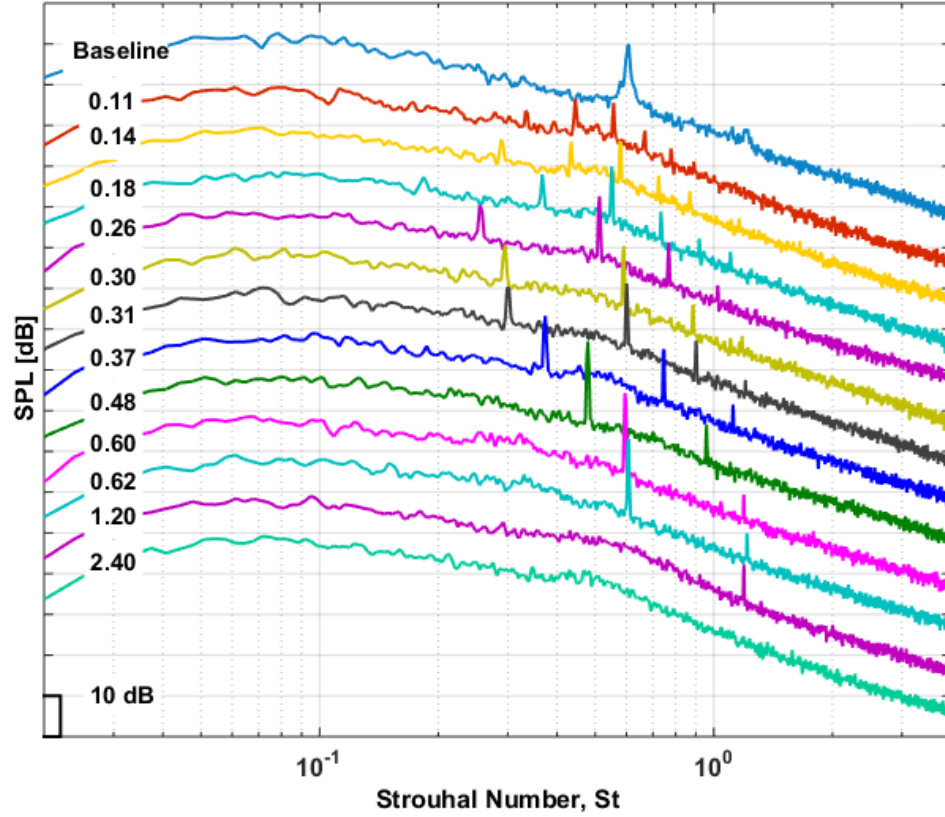
Figure 80. Wake fluctuating pressure spectra for baseline and low-frequency excitation regime at $\alpha = 19°$ and $Re = 0.5 \times 10^6$

Each spectrum presented in the figure has a label on the left, which indicates the excitation Strouhal number and is separated by 10 decibels from the curve above it for

117

clarity. This figure does not provide absolute magnitude data and thus serves for comparison purposes only. A well-defined peak with a relatively broad base for the baseline case indicates that most of the energy is concentrated in a range of frequencies centered around the natural shedding frequency which corresponds to a Strouhal number of 0.6. When the flow is forced at any Strouhal number below 2.4, not only a peak at the forced Strouhal number is observed but also, in most of the cases, several harmonics are generated as well. It must be noted that in every case, the harmonic that is closest to St = 0.6 has the largest amplitude as this is the most amplified frequency. Case in point is forcing at St_e= 0.18. Although the actuator excites the flow at St_e = 0.18, due to the amplification of disturbances, the energy removed from the freestream is put into a shedding frequency that is closest to natural shedding frequency. For excitation at St_e = 0.18, this frequency is 0.54 which is the third harmonic of the excitation frequency. In other words, the energy injected by the actuator helps to amplify the disturbances that remove even more energy for the freestream flow as can be inferred from the magnitude of the peaks.

The receptivity of the airfoil's wake and separated shear layer can be seen in Figure 80 as well. Moving down from top to bottom, it is readily evident that a band of frequencies centered about the natural shedding frequency have the largest amplitude and the other peaks located outside of this band possess a significantly smaller amplitude peaks. It is interesting to note that forcing at St_e = 0.60, 0.62 and 1.20 generates broadband peaks at

St = 0.30, 0.31 and 0.60 respectively. This confirms the existence of merging events downstream of the TE.

It must be noted that as the excitation in the low-frequency regime generates large-scale structures with a significant pressure signature, the amplitudes of the peaks in the low-frequency regime spectra are considerably higher than those of the mid to high frequency regimes where due to early breakdown of the structures, their signature cannot be registered at point D which is located downstream of the trailing edge. As a result, starting with St_e = 2.04 in Figure 80 and continuing on to higher excitation frequencies, the spectra of the excited flow become markedly different from those of the lower frequencies. A less defined and broad peak developed around St = 0.50 suggests that the vortices shed into the wake are less coherent at this excitation frequency. This point is further supported by the vorticity plots of Figure 70. The same trend was observed when the flow was forced at Strouhal numbers of $O(10)$ with the difference that the spectral peaks around St = 0.5 become slightly stronger and more defined as the forcing frequency increases.

4.2.4   Static Surface Pressure

The surface pressure data presented in Figure 81 are last segments of the data acquired to characterize the flow field response to low and high-frequency excitation. Surface pressure data were obtained from 30 uncovered pressure taps as 3 pressure taps were

covered due to the presence of the actuator. The loss of the pressure taps near the leading

edge affects the accuracy of the lift predicted as most of the lift is generated close to

leading edge in the VR-7 airfoil. With the loss of these pressure taps, the coefficient of

lift and coefficient of drag were calculated to be 0.31 and 0.84 for the baseline airfoil.

Given that the flow is fully separated, the loss of pressure taps is of little consequence in

the baseline case. However, in excited cases, due to the increased suction peak close to

the leading edge, the coefficient of lift would be underestimated. The coefficient of

pressure distributions for the baseline and excited cases are shown in Figure 81.
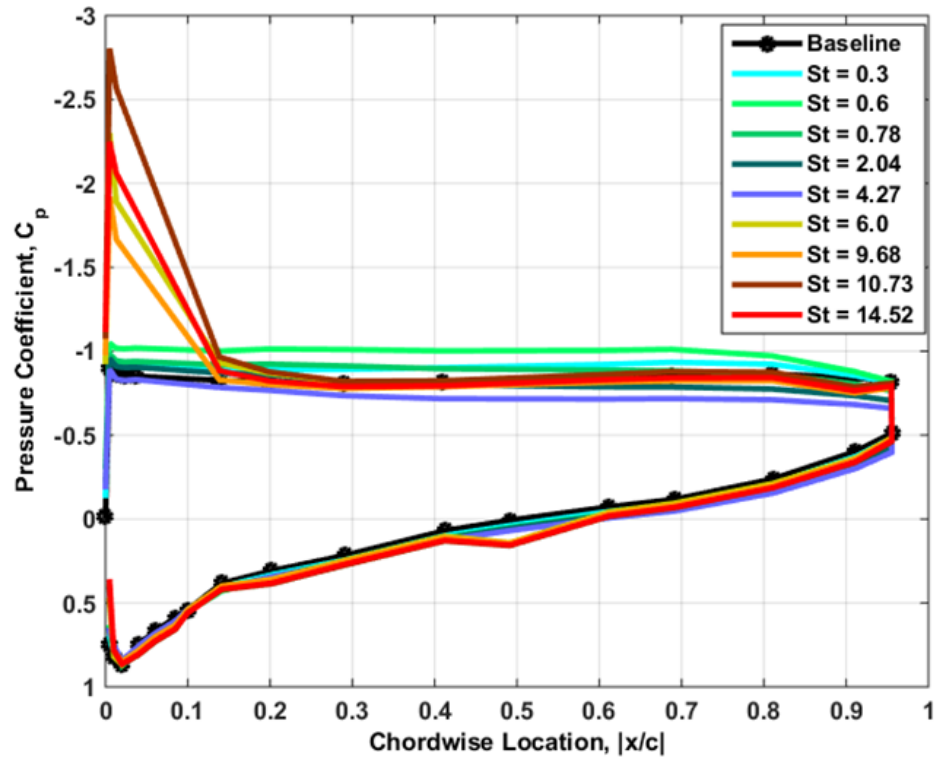
Figure 81. Pressure coefficient distribution for baseline, low- and high-frequency excited

cases at $\alpha = 19°$ and Re $= 0.5\times10^6$

For $St_e = 6.0$, which is coincident with the natural shedding Strouhal number, the coefficient of pressure on the suction side has decreased significantly, which suggests that the flow has been accelerated compared to the baseline case. As can be seen in Figure 81, low-frequency excitation leads to a nearly uniform increase in suction over the airfoil. This is to be expected since, according to phase-locked PIV data presented in section 4.2.2, low-frequency excitation leads to the generation of large-scale coherent structures that bring the free-stream momentum close to the airfoil surface and hence, accelerate the flow. This explains the observed increase in suction over the airfoil. It is interesting to note that exciting the flow at $St_e = 0.6$ leads to the biggest increase in suction in the low-frequency excitation regime. Nevertheless, the coefficient of pressure is nearly constant over the suction side and thus the flow remains separated which is, again, confirmed by time-averaged maps of total velocity in Figure 69. As can be inferred from velocity distribution plots of Figure 69, exciting the flow at $St_e = 2.04$ and 4.22 leads to considerable acceleration of flow which is expected to result in the appearance of a suction peak close to the leading edge. Unfortunately, the loss of pressure taps in the leading edge means that the effect of partial reattachment of the flow in this area cannot be registered by pressure sensors. Had the pressure taps been available, based on PIV data, a significant suction peak around the leading edge would have been observed.

The surface pressure distributions for high-frequency excitation cases are also presented in Figure 81. Here, in contrast to low-frequency excitation results the control effects are

121

manifested in the form of suction peaks close to the leading edge of the airfoil. Firstly, the fact that these peaks have been registered by the pressure transducers suggests that the suction peak has been shifted forward, where the pressure taps are not covered by the electrodes, in high-frequency excitation cases. This, in turn, indicates that the flow is highly accelerated by numerous small-scale structures, seen in Figure 76, that are generated as a result of high-frequency excitation. Secondly, the control effects are only observed in the leading-edge area from $x/c = 0$ to $x/c = 0.3$. This is in line with the previously-observed breakdown of small-scale structures (as seen in Figure 82) which means they are no longer able to mix the free-stream momentum and bring it close to the airfoil surface. Hence, the pressure distribution from mid-chord to trailing edge remains unchanged compared to the baseline case. The comparison between surface pressure data and PIV data as seen in Figure 82 further corroborates the above observations as the sudden drop in suction at $x/c = 0.3$ is at the intersection of the zero-velocity line and airfoil surface.

The coefficient of lift and drag (not shown here) can be computed from pressure coefficient distributions via integration. It is observed that the coefficient of lift and drag mirror one another very well – both attain a maximum when the actuators are excited at the natural Strouhal number. This is due to the fact that the mechanism through which the flow is influenced directly connects the changes in lift and drag together. The energy injected into the flow by the actuator excites natural instabilities that generate coherent structures. These structures remove energy from the freestream flow that results in an

122

increase in drag. At the same time, the generated coherent vortices promote momentum exchange with the freestream flow, which accelerates the flow and amplifies the lift generated by the airfoil. As can be seen, the efficiency of this mechanism is directly dependent on the amplification of natural flow instabilities. That's the reason why forcing at natural shedding frequency ($St_e = 0.6$) not only accelerates the flow, but also removes energy from it.
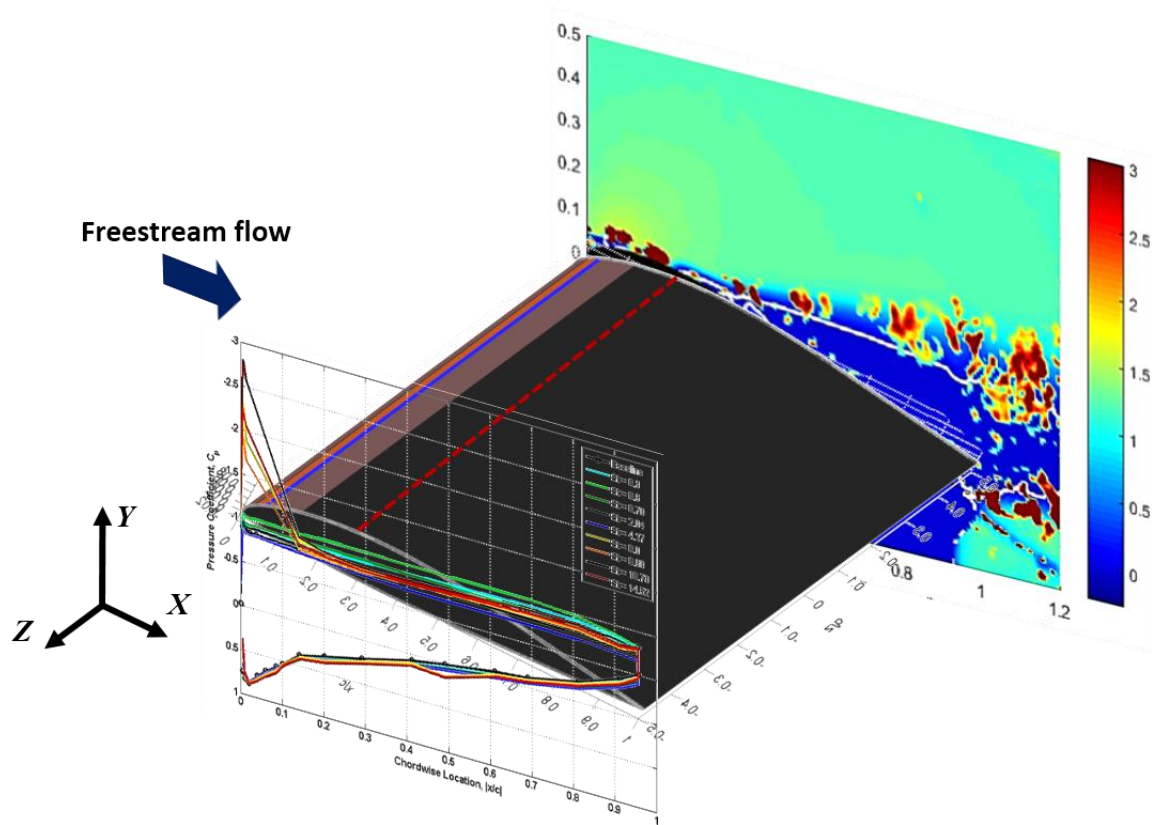
Figure 82. Comparison between flow reattachment point at $St_e = 6.0$ obtained from PIV and surface pressure data for the high-frequency excitation regime

123

The flow unsteadiness due to roll-up and shedding of coherent structures, registered in phase-locked PIV and microphone measurements, can also be seen in the surface pressure data. Time histories of pressure coefficient for various excited cases are plotted in Figure 83. Two blocks of 22,500 samples were acquired at a sampling rate of 450 Hz for each case since operating the nanosecond pulser for extended periods of time would lead to excessive heating of the IGBT switches. The data set presented here were acquired using a LabView code that synchronized the operation of the actuator and acquisition of pressure data, i.e. the DAQ board started sampling the pressure data as soon as the actuators where turned on.

The marginal increases in strength of the structures shed from leading-edge at $St_e = 1.2$, compared to $St_e = 0.6$, and also the reduction of their wavelength explains the noticeable increase in the number of suction peaks for the $St_e = 1.2$ case. As the excitation frequency is increased, the number and amplitude of the suction peaks decreases, presumably due to the lower swirling strength of the smaller structures. As the signature of these structures decay exponentially with distance, the amplitude of the pressure fluctuations also decreases further downstream as can be seen, for example, in the $St_e = 10.37$ case. Increasing the excitation frequency to $St_e = 2.65$ and beyond leads to the emergence of a particularly interesting feature in the form of suction "spikes" at the beginning of each acquisition interval. The amplitude of these suction "spikes" are lower than the peaks observed in the low-frequency excited cases, suggesting that the strength of the structures

124

generated due to the perturbation of the flow at higher frequencies is lower than their low-frequency counterparts, an observation which has been made previously when examining Figure 71 and Figure 76.

The amplitudes of the suction peaks, which last for 2 to 3 seconds after the discharge initiation in the actuator, in medium- to high-frequency excited cases are not in agreement with the observed peaks in the time-averaged pressure data but the plateaus in the pressure distribution from $t = 3$ to $t = 50$, unlike the periodic peaks observed throughout the acquisition period for low-frequency cases, suggest that no periodic shedding and therefore, unsteadiness in present in high-frequency-excited cases. Since no correction has been applied to the pressure data to account for the reduction in amplitude and phase lag introduced by the pressure tubes, it is likely that the discrepancies observed are a mere artifact of the differences in the length of the pressure tubes. Nevertheless, the time histories of the pressure data further confirm the trends observed in phase-locked PIV data in that high-frequency excitation would not introduce periodic variations in pressure and load distribution while low-frequency excitation will do so.
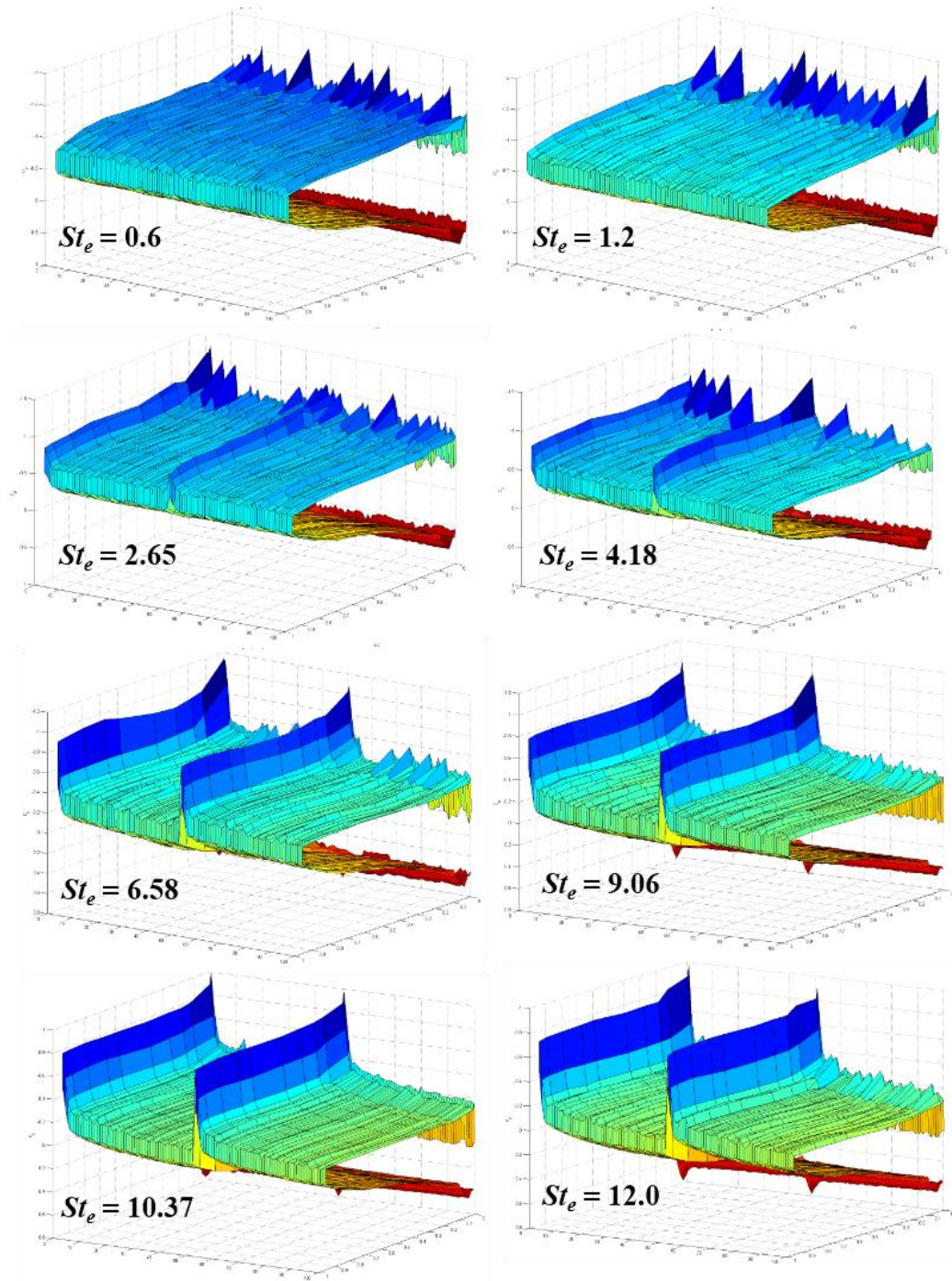
Figure 83. Time traces of pressure coefficient for low- and high-frequency excited cases

at α = 19° and Re = 0.5×10⁶

126

4.3 Investigating Flow Three-dimensionality at Low to High-Frequency Excitation Regimes

In the course of investigating the effects of excitation frequency on the flow field, discrepancies between surface pressure and planar streamwise PIV data, obtained at different spanwise locations, were discovered. Based on the previous experience of the author, this gave rise to the idea that three-dimensional features might be present over the airfoil and the two-dimensional flow assumption might not be representative of the actual flow field. A limited series of surface oil flow visualization experiments confirmed this hypothesis. To understand how changes in excitation regime affect the flow and under which conditions three-dimensional flow features emerge an extensive experimental campaign was carried out. Spanwise stereo PIV was used to map the velocity distributions along the span of the airfoil while fluorescent surface oil flow visualization and pressure sensitive paint were used to record the surface signature and topology of three-dimensional features. Furthermore, to understand the role of excitation signal in the emergence of three-dimensional features, a high-frequency carrier wave (2 kHz) was modulated at several low Strouhal number excitation frequencies and was fed to the actuator. The flow response to such an excitation was then recorded using spanwise stereo PIV and surface pressure measurements. In what follows, the documented flow response to various excitation regimes and signal modulation will be presented.

4.3.1 Time-averaged Flow Field Data

The variation in lift coefficient of the baseline model (with actuators installed but deactivated) with respect to angle of attack and Reynolds number is shown in Figure 84. Spalart[40] in his analysis of stall cells using lifting line theory claims that the destabilizing interaction between the wing and trailing vortices leads to the appearance of stall cells when $\frac{dc_l}{d\alpha} < 0$. This claim agrees with early observations of Yon and Katz[46] on a thick NACA 0015 airfoil where a two-cell pattern was formed at shallow post-stall angles. Disotell and Gregory[72] also observed that stall cells are typically formed at shallow post-stall angles on thick airfoils, as confirmed by earlier studies of Broeren and Bragg[47].

Examining the data points presented in Figure 84, it is evident that the stall angle for the VR-7 airfoil at a Reynolds number of 0.5×10^6 is 16°. The airfoil demonstrates the typical stalling behavior expected from thin airfoils[31], [39], specifically, a rapid drop in lift coefficient C_l due to abrupt leading edge flow separation is observed at all tested Reynolds numbers, although the effects are less severe at $Re = 1.0\times10^6$. All the experiments in this report were conducted for the airfoil in deep-stall at $\alpha = 19°$ and $Re = 0.5\times10^6$ where $\frac{dc_l}{d\alpha} > 0$. Compared to the findings of Yon and Katz[46] for a NACA 0015, this is well outside the angle of attack region in which the emergence of stall cells is expected. Also, according to Spalart's analysis[40], wing-vortex interactions are self-

correcting for spanwise variations in this region and, as a result, appearance of stall cells is not likely.
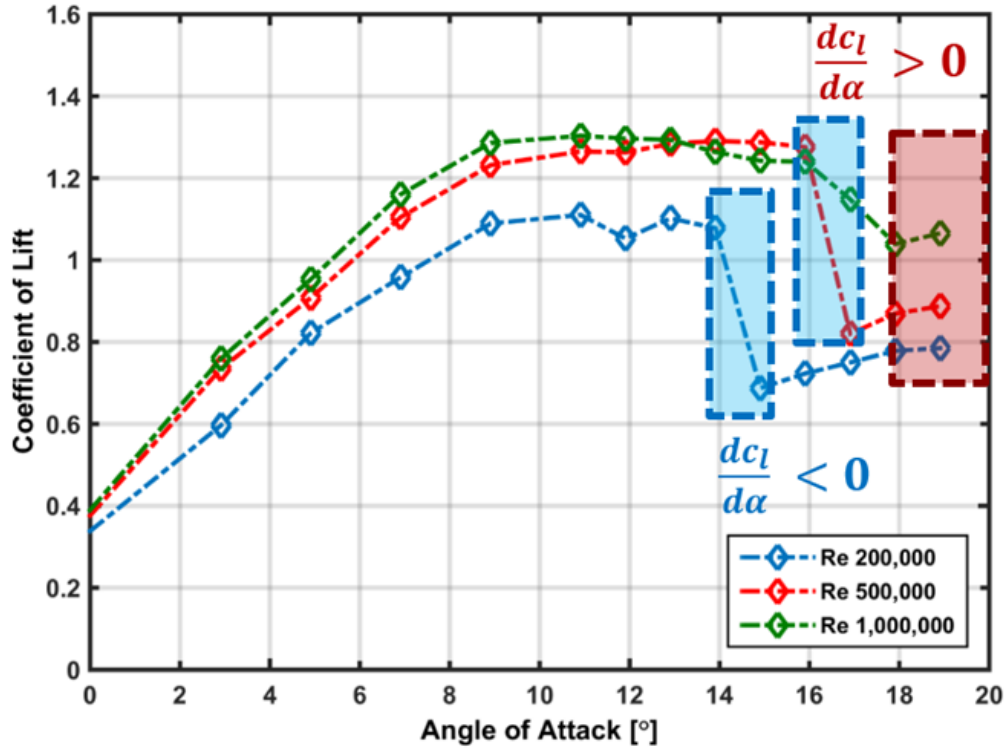
Figure 84. Variation of lift coefficient C_l versus angle of attack α for different Reynolds numbers – blue: previously reported stall cells presence, red: stall cell presence in current experiments

Despite all this, an examination of the normalized PIV and FSOFV data for the baseline airfoil presented in Figure 64 and Figure 65 indicates that a 3-D separation front exists over the model. Such separation fronts were observed by Disotell and Gregory[72],

DeMauro et al.[50] and Dell'Orso et al.[56] and were suggested to be precursors to the development of well-defined mushroom-shaped structures. Very weak spiral nodes at z/b =10% and 50% may be present in the FSOFV image of the baseline model in Figure 85a. The rounded edges of the dashed zero-velocity line, at z/b =-0.4 and 0 (as seen in Figure 86a) may indicate the presence of streamwise vortices embedded within the shear layer that are bending and distorting the shear layer according to Manolesos and Voutsinas[12] and more recently Ragni and Ferreira[41].

As mentioned previously, the main objective of this work is to explore the effect of perturbations, generated by nanosecond discharges, on the development of the surface topology and stall cells over a thin airfoil in deep stall. These effects are discussed in the following sections. The asymmetric surface pattern of the baseline develops into two asymmetric, well-defined, mushroom-shaped stall cells as the flow is excited at $St_e = 0.6$ (Figure 85b). The streamwise map of total velocity for $St_e = 0.6$, presented in Figure 86b, indicates that excitation at this frequency accelerates the flow near the leading edge, reduces the separation height by bringing the zero-velocity line closer to the airfoil surface and reduces the magnitude of the reversed flow in the separation zone. This reduction is due to the increased mixing caused by the generation and downstream convection of large-scale structures due to low-frequency excitation mentioned in our previous publication[73]. In contrast, high-frequency excitation has been observed to lead to the generation of small-scale structures that disintegrate quickly.

The reduction in the size of the separation zone is also evident in the FSOFV image of the $St_e = 0.6$ case in Figure 88b where the separation line has moved further downstream. The spiral nodes are now clearly visible under the effect of excitation at $St_e = 0.6$. While spanwise PIV data does not indicate the presence of stall cells, this discrepancy between the SOFV and PIV is discussed and explained later in this paper. At this time, suffice it to say that the authors are confident stall cells have formed under these conditions. The reduction in the size of the reversed flow region and stall cells due to excitation leads to a decrease in drag coefficient C_d.

Increasing the excitation frequency to $St_e = 4.27$ leads to the spanwise modulation of streamwise velocity, as reported by Spalart[40], and emergence two well-defined asymmetric stall cells, as can be seen in Figure 85c and Figure 86c. This change in flow topology begins to occur at an excitation frequency of $St_e = 2.04$, therefore, excitation frequencies above this value will subsequently be referred to as "high", while those below it will be referred to as "low". It should be emphasized that this distinction is made by the flow behavior, rather than from a first-principles standpoint. The separation height, measured at $z/b = 0$ is also significantly reduced compared to the baseline case (Figure 86c). The streamwise 2-D-2C and stereo PIV clearly demonstrate the changes in the global flow field due to excitation by NS-DBD actuators. The streamwise map of total velocity and FSOFV data for $St_e = 4.27$ indicate that the flow velocity over the leading edge has significantly increased compared to the baseline and low-frequency excitation cases. The magnitude of the minimum velocity in the reversed flow region in the stall

cells, however, has increased compared to the low-frequency excitation case, due to the generation of small structures which reduce shear layer mixing and momentum transport.

Finally, it is interesting to note that increasing the excitation frequency to $St_e = 10.73$ further bends the shear layer, compared to $St_e = 4.27$, as can be deduced by comparing the zero velocity lines in Figure 86 and Figure 88. Two spiral nodes at $z/b = -0.4$ and -0.1, seen in the FSOFV image of Figure 85c, are the footprints of streamwise vortices, embedded in the shear layer, that are responsible for this effect as mentioned by analysis of stereo PIV data in Ragni and Ferreira's work[41] .

It is worth mentioning that stall cells have not been observed over thin airfoils in post-stall conditions previously. We believe their presence in our experiments can be explained by the fact that the appropriate disturbance environment is introduced by excitation. We thus postulate that whether the airfoil is thick or thin does not play as important a role in the emergence of stall cells as the presence of the appropriate disturbance environment. As stall cells have not previously been reported to emerge over thin airfoils in deep stall, their spatial organization, and how it compares to typically observed stall cells, is of significant interest. Various authors have proposed empirical relations for determining the number and wavelength of stall cells on thick airfoils in shallow post-stall angles. Weihs and Katz[44] suggested that the number of stall cells can be predicted using equation (1).

$$n = \frac{AR}{2.8} \qquad (2)$$

132

Boiko et al.[45] proposed the following formula for the number of stall cells:

$$n = \frac{AR}{17.2 \times k \times \tan\alpha_V} \qquad (3)$$

Where k is the chord-normalized distance between the separation line and focal point of the spiral nodes and α_V is the angle at which flow separation is observed for the first time. The lifting line analysis of Gross et al.[74] gave the following relation between the wavelength of stall cells and the airfoil chord:

$$\frac{\lambda_c}{c} = 2.1 \qquad (4)$$

Disotell's analysis[72], based on the low-frequency unsteadiness observed in the stall cells yielded the following expression for the number of stall cells:

$$n = \frac{U_\infty}{U_c} \frac{St \times AR}{\sin\alpha} \qquad (5)$$

Where U_c is the average convective velocity of eddies in the separated flow region and St is defined as follows:

$$St = \frac{U_\infty}{U_c} \frac{c}{\lambda_c} \sin\alpha \qquad (6)$$

While using equations 1 to 3 closely predicts the wavelength of stall cell pattern observed in the baseline airfoil, none comes close to predicting the number of observed stall cells or their wavelength λ_c in excited cases. The expression offered by Disotell[72] overestimates the number of stall cells (2.40) which does not agree either with the

133

baseline case or the excited flows. It appears that none of these equations accurately predict the stall cells emerging due to excitation.
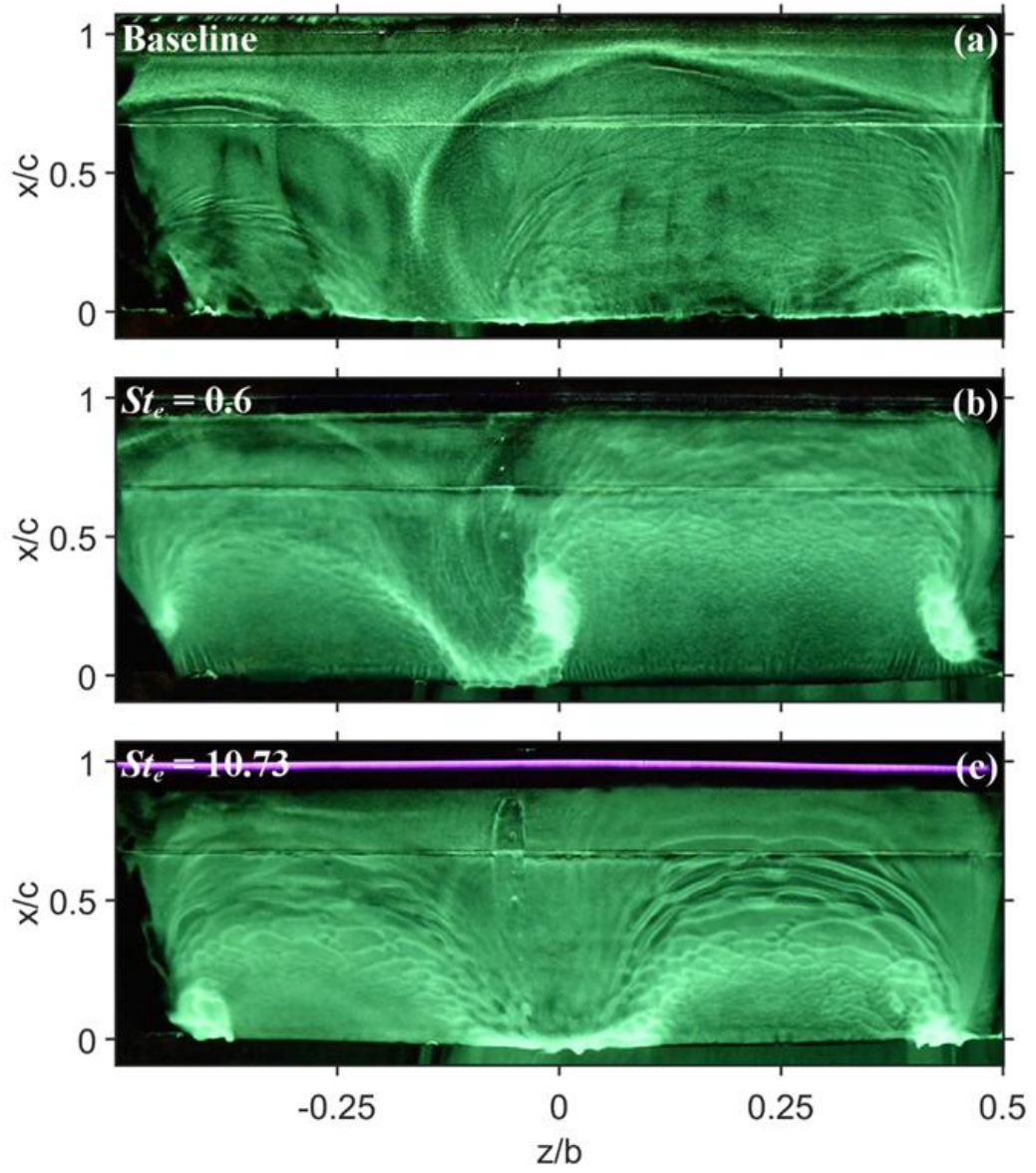
Figure 85. Fluorescent surface oil flow visualization at α = 19° and Re = 0.5×10^6 (a)

baseline, (b) St_e = 0.6 representing low-frequency regime and, (c) St_e = 10.73

representing the high-frequency excitation regime
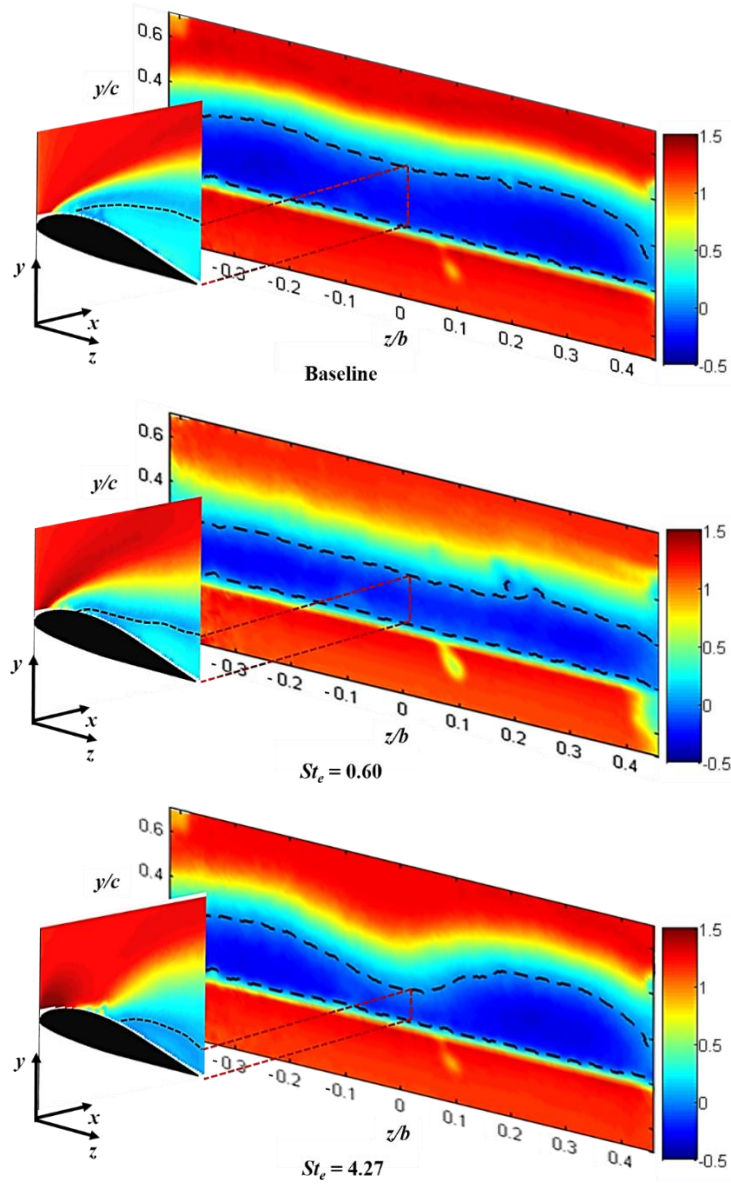
Figure 86. Comparison between maps of normalized ensemble-averaged streamwise component of velocity u^* on a cross-stream plane at x/c =1.05 and total normalized velocity U^* at a streamwise plane at z/b = 0.45 for α = 19° and Re = 0.5×10^6 at various excitation S

136
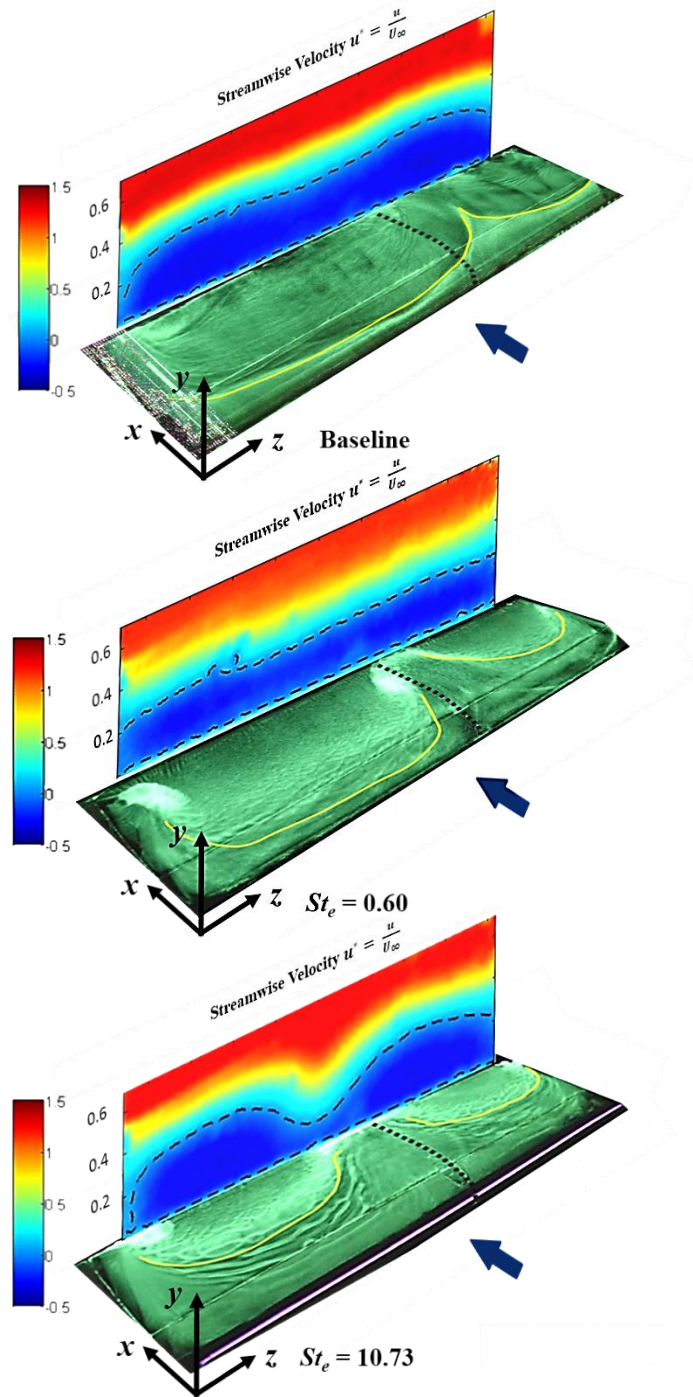
Figure 87. Comparison between maps of normalized ensemble-averaged streamwise

component of velocity u^* on a cross-stream plane at x/c =1.05 and fluorescent surface oil flow

visualization for α = 19° and Re = 0.5×10^6 at various excitation Strouhal numbers.

Another important aspect of the overall flow field in the presence of stall cells is the pressure distribution over the airfoil. The effect of stall cells on the accuracy of 2-D assumptions by virtue of which the pressure data acquired at mid-span is applied to the entire airfoil is examined. Keeping in mind that the VR-7 airfoil is a thin airfoil which generates most of its lift close to the leading edge, the presence of stall cells close to the leading edge is likely to introduce spanwise variations in the wing loading. However, if the stall cells contract away from the leading edge, the airfoil will not likely experience large spanwise variations in loading. As such, calculating drag and moment coefficients for the entire airfoil based on mid-span measurements is likely to introduce errors, but the level of error will depend on the extent of separation over the airfoil and the existence of stall cells. For example, the location of surface pressure taps is indicated by black dotted lines in the FSOFV images of Figure 88. While the pressure taps are well within the separated flow region in the baseline case, they are situated between the stall cells when the flow is excited at either $St_e = 0.6$ or $St_e = 4.27$ and therefore miss the true extent of the separation.

In order to further study the development of flow topology over the airfoil under the effect of excitation, qualitative maps of surface pressure distribution were obtained using pressure sensitive paint. No calibration was applied to the intensity ratio maps that were obtained through the procedure outlined in section 3.3.2. Maps of intensity ratio, proportional to pressure via calibration constants, for two excited cases are compared to the surface topology obtained from surface oil flow visualization experiments in Figure

88. Here, darker shades of red indicate lower pressure while dark blue indicates higher static pressure. Due to the flow unsteadiness in the $St_e = 0.6$ case, one cannot clearly see a well-defined separation line in either the flow visualization or PSP data yet still regions of attached and separated flow, marked by low and high pressures respectively, can be discerned in the intensity ratio map. In contrast, the excited case $St_e = 10.73$ clearly shows the separation line and the fluorescent surface oil flow visualization and pressure sensitive paint data are in complete agreement. While the attached flow outside the stall cell is accelerated, resulting in a low static pressure, the pressure in the separated region inside the cell is higher as indicated by light blue concentrations. While the flow outside a stall cell is no necessarily attached, according to Manolesos[49], [75], the PSP data indicate that this indeed is the case when the flow is excited at $St_e = 10.73$.

The validity of PSP data can be further corroborated by comparing the flow features form the surface maps to streamwise 2-D PIV data as seen in Figure 89. Regions of accelerated flow close to the leading edge under excitation at $St_e = 4.27$ result in a low static pressure distribution which is registered by the paint and can be seen in the form of a bright red distribution downstream of actuator. The higher pressure of the separated, recirculating flow inside the stall cell also registered by the paint and is marked by light blue concentrations behind the 3-D separation line for both excited cases. Approximate separation lines obtained from the intensity ratio maps agree well with the location of zero-velocity line intersection with the surface obtained from streamwise PIV data.
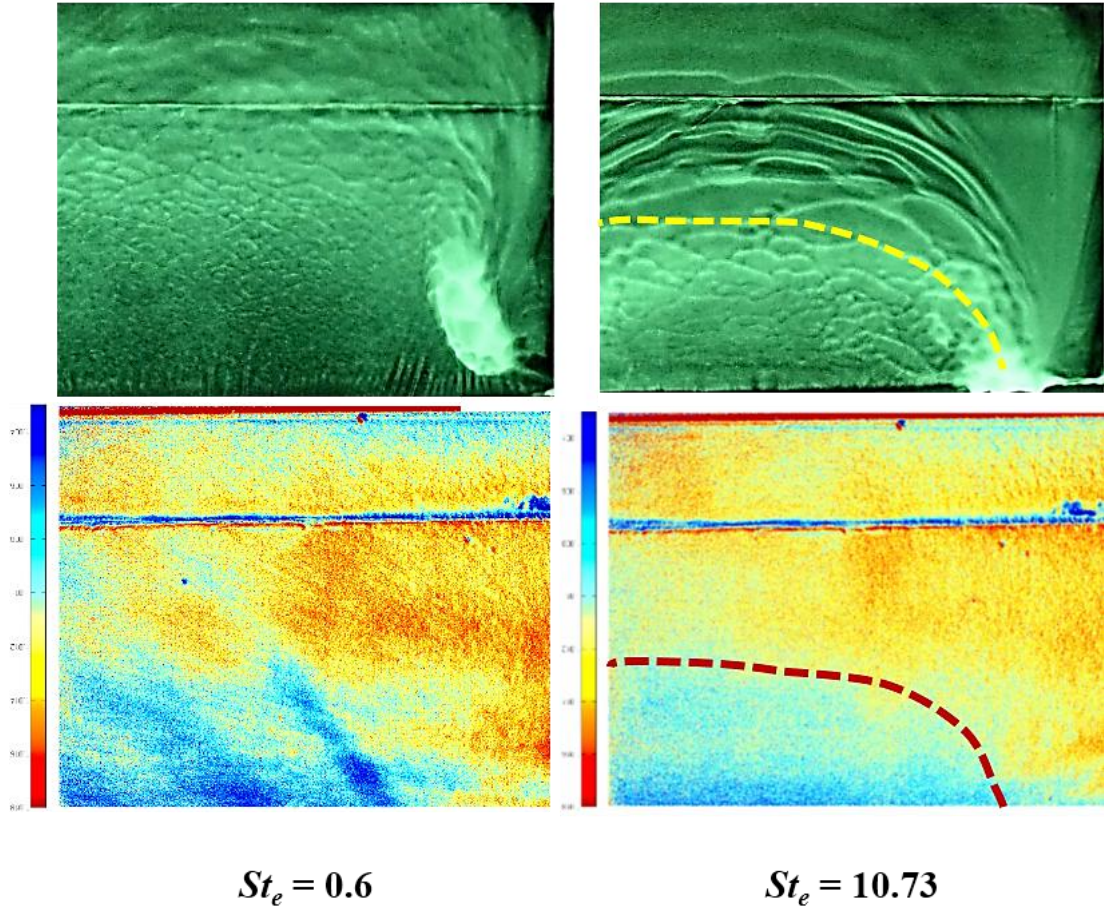
Figure 88. Comparison between PSP intensity maps and SOFV for two excited cases at α
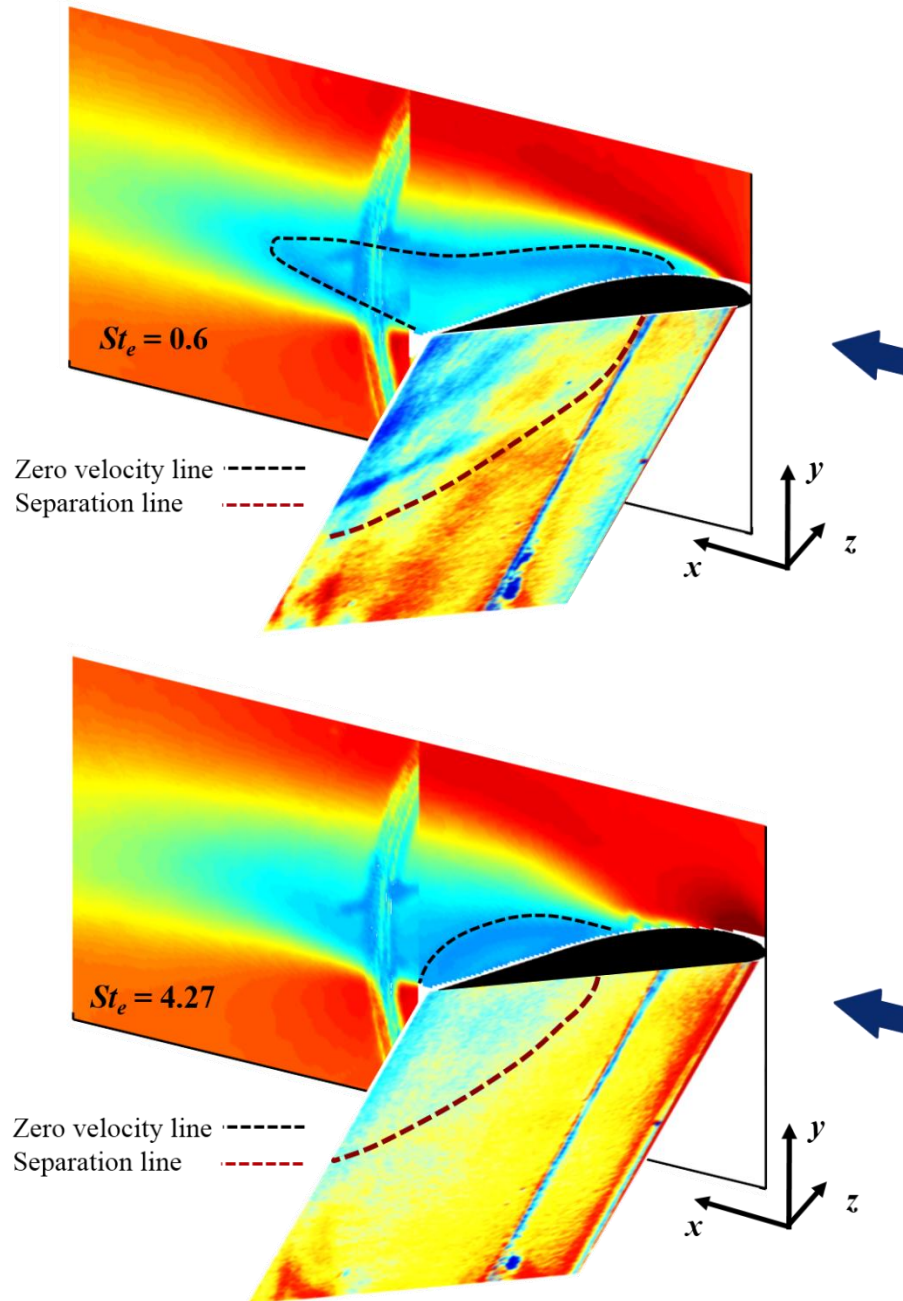
= 19° and Re = 0.5×10⁶

Figure 89. Agreement between PSP and PIV data for two excited cases at α = 19° and Re

$= 0.5 \times 10^6$

An experiment was conducted to study the flow field development after the actuator was turned off. Since the aim was to observe the changes that would happen to a well-defined stall cells, the excited flow field at $St_e = 10.73$ was chosen as the baseline. Once a steady freestream flow in the tunnel was established, the actuator was turned on and the tunnel was run for approximately 6 minutes so that a well-defined, steady pattern would emerge on the surface of the airfoil. The first image was acquired just before the actuator was turned off at $T = t_0$ (Figure 90a.) and subsequent images were taken in 10 s intervals. At $T = t_0 + 10$ (Figure 90b), the strength of the vortex node impinging at $z/b = -0.1$ is significantly increased and the node shifts to the left close to $z/b = 0$. Simultaneously, the size of the stall cell on the left half of the airfoil is significantly reduced. This trend is reversed in Figure 90c-f where the stall continues to grow and the separation line continues to move upstream and is finally stabilized at $T = t_0 + 40$. At the same time, the size of the bigger cell on the right continues to diminish and finally returns to its original shape at $T = t_0$. At $T = t_0 + 30$ (Figure 90d), a relatively strong vortex node starts to appear at $z/b = 0.4$ and moves to the right while deforming and slightly moving upstream. A stable surface pattern that strongly resembles the initial surface topology at $T = t_0$ emerges at $T = t_0 + 50$ (Figure 90f).

It appears that turning the actuator off has an initial disrupting effect on the flow field but eventually, after approximately 40 seconds, the flow reverts to nearly its original equilibrium state that was established due to excitation. The experiment was repeated with the same result. Even long after the actuator is turned off, the surface topology does

not indicate the presence of a quasi-3-D separation front that was seen in the baseline case (Figure 85a), rather the signature of the stall cells remains clearly visible. This seems to suggest that with the presence of large separated flow and stall cells, the flow has become self-sustaining and absolutely unstable, similar to other self-sustaining flows such as a resonating cavity [76]. This means that the initial perturbations provided by the actuation grow and roll up into large-scale structures due to instability of the shear layer over the separated region, they interact with the surface due to the presence of stall cells and generate perturbations of the same frequency, which travel back to the actuation location and perturb the shear layer. With this arrangement, when the actuation stops, this feedback process sustains the perturbation and excitation of the shear layer. While this process seems plausible, more research is needed to verify this finding and provide further information and better understanding of the process.
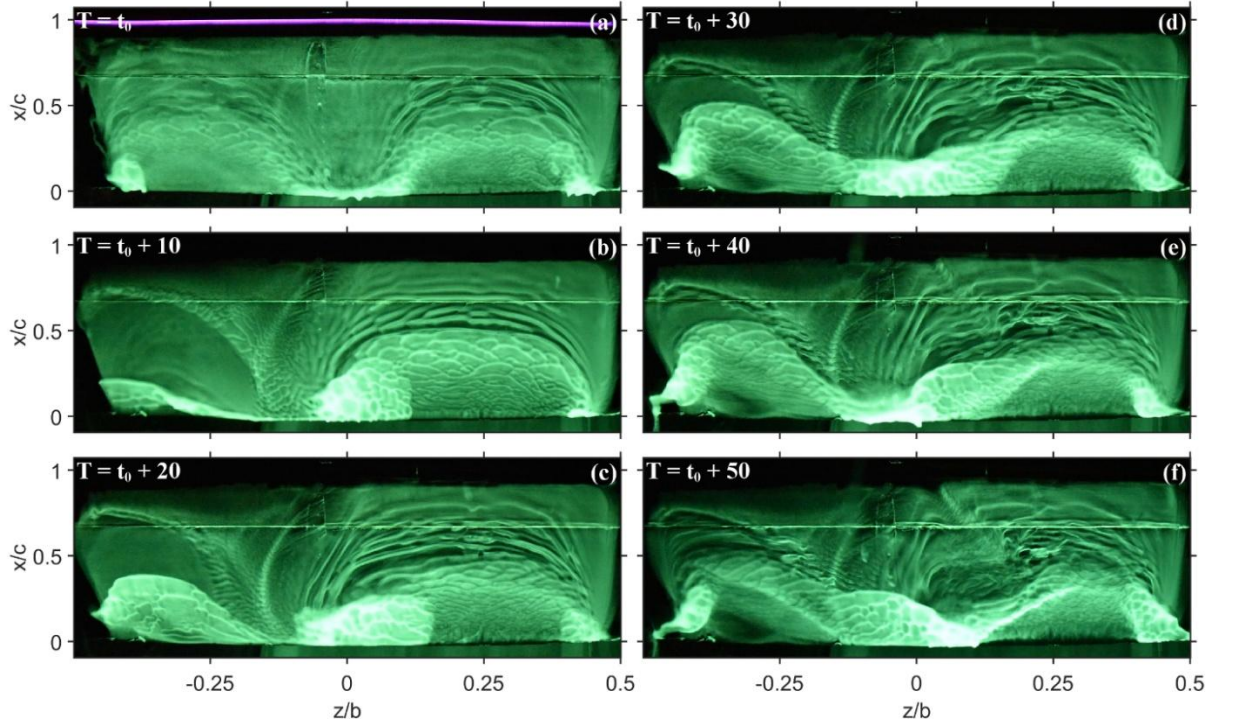
Figure 90. Series of still oil flow visualization images acquired at α = 19° and Re = 0.5×10⁶ depicting the development of surface topology pattern after turning off the actuator (St_e = 10.73) at T = t_0

To better ascertain the dependence of the three-dimensionality of the flow field on excitation frequency, spanwise maps of velocity distribution downstream of the trailing edge at x/c =1.05 were acquired for a sweep of excitation frequencies. The ensemble-averaged maps of normalized streamwise velocity for baseline and excited cases are presented in Figure 91 and Figure 92. Dashed black lines indicate zero streamwise velocity and can be used to assess separation height at each spanwise location. As mentioned previously, the baseline distribution of streamwise velocity indicates a 3-D separation line pattern. Additionally, evidence of a vortex pair embedded within the shear layer with its cores located at z/b = -0.4 and -0.1, bending the zero-velocity line at those spanwise locations, previously observed by Ragni and Ferreira[41] and Manolesos[77], may be present in Figure 91a.

Exciting the flow at St_e = 0.3 results in a nearly two-dimensional distribution of velocity as is seen in Figure 91b. The extent of the pockets of strong reversed flow is considerably reduced as is the amplitude of the streamwise velocity from y/c = 0.4 to 0.6. These affects have been attributed to the large-scale structures caused by excitation. The vertical velocity component (shown in Figure 93 and Figure 94) supports this claim by providing evidence of strong, spanwise-uniform shedding. These strong spanwise structures have been previously observed in the spanwise phase-locked PIV data and are believed to be the cause of the apparent discrepancy (noted earlier) between Figure 85b and Figure 86b. It is hypothesized that the strong spanwise structures confine the 3-D topology of the stall cells to the near surface region. This is observed for the low frequency cases (St_e < 2.04)

145

in which strong spanwise shedding is evident (see Figure 93b-d). Despite the relatively 2-D zero-velocity line in the low frequency cases, as the excitation Strouhal number increases, two pockets of strong reversed flow begin to form (see Figure 91d). This is can be due to the weakening of the strong spanwise structures and the incremental expansion of the stall cell topology from the near wall region.

Further increase of excitation frequency into the (previously defined) "high" frequency regime, St_e = 2.04 (Figure 91e), and beyond, results in the emergence two asymmetric stall cells with the right-hand cell having a slightly larger separation height than the one located on the left. The existing literature[43], [46], [50], [51], [72] does not offer any clear explanations as to why stall cells are sometimes asymmetrical. At St_e = 4.27, while the separation height at z/b = 0 is reduced compared to St_e = 2.04 (Figure 91e and f) which will appear as a reduction in the size of the separated flow region in the streamwise planar PIV data, the separation height of the stall cells has increased. Comparing the plots of normal velocity components for St_e = 2.04 and St_e = 4.27 (Figure 93e and f) indicates that vortex shedding has been weakened significantly with increases in frequency compared to the baseline case. This is in line with the fact that excitation at higher frequencies expedites the development and breakdown of small-scale structures[34] and their disintegration results in diminishing values of the normal component of velocity. The same trends are observed as the excitation frequency continues to increase.
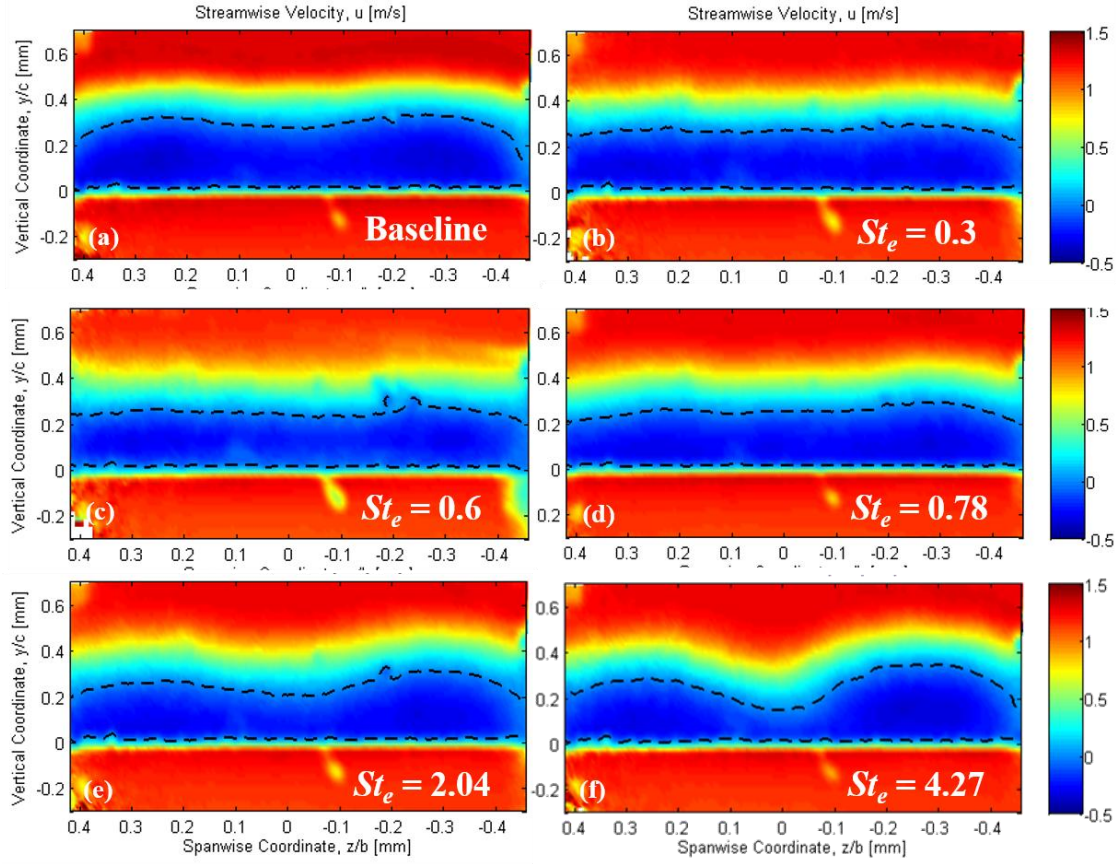
Figure 91. Color maps of normalized ensemble-averaged streamwise component of velocity u^* on a cross-stream plane at x/c =1.05 for α = 19° and Re = 0.5×10^6 for low to mid-frequency excitation regimes. Dashed black lines indicate zero streamwise velocity

Figure 92. Color maps of normalized ensemble-averaged streamwise component of velocity u^* on a cross-stream plane at x/c =1.05 for α = 19° and Re = 0.5×10^6 for high-frequency excitation regime. Dashed black lines indicate zero streamwise velocity
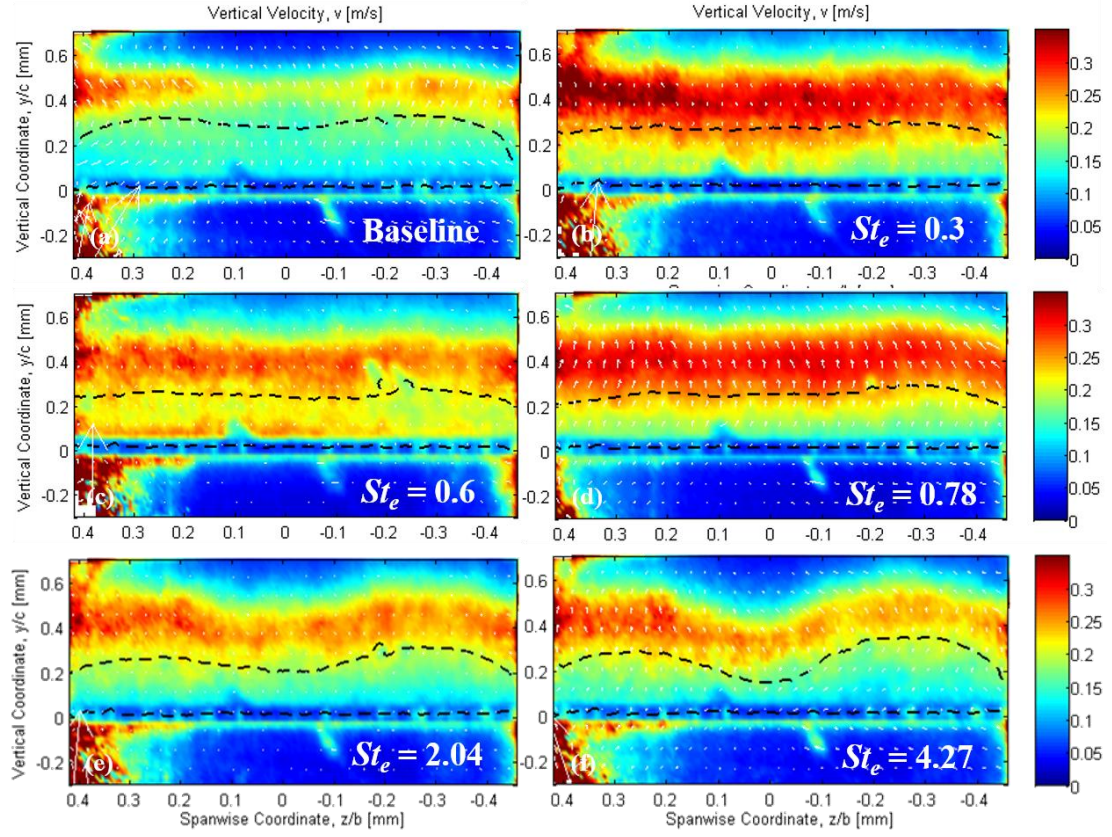
Figure 93. Color maps of normalized ensemble-averaged normal component of velocity v^* on a cross-stream plane at x/c =1.05 for α = 19° and Re = 0.5×10^6 for low to mid-frequency excitation regimes. Dashed black lines indicate zero streamwise velocity
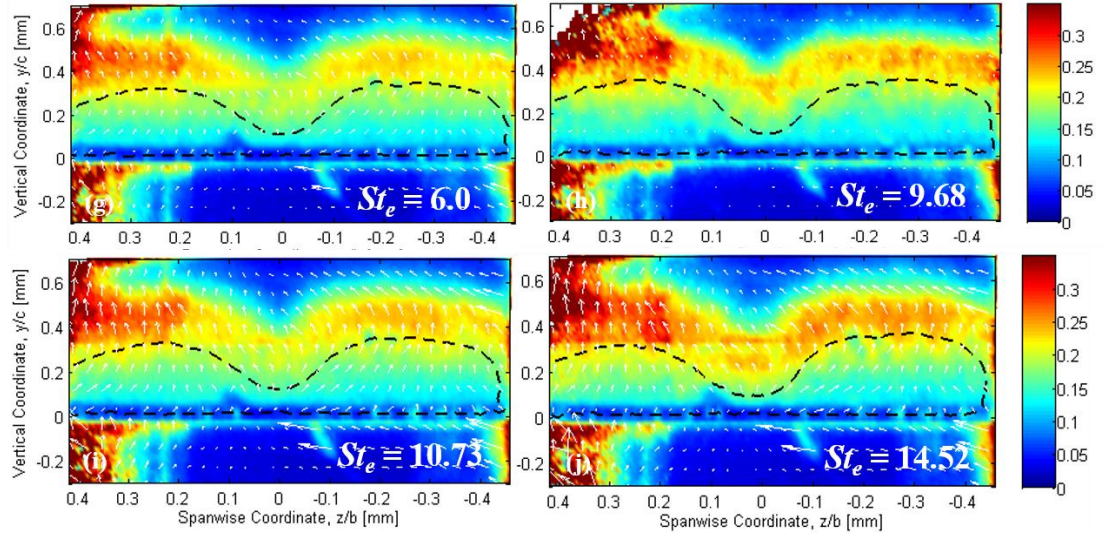
Figure 94. Color maps of normalized ensemble-averaged normal component of velocity v^* on a cross-stream plane at x/c =1.05 for α = 19° and Re = 0.5×10⁶ for high-frequency excitation regime. Dashed black lines indicate zero streamwise velocity

The previously-mentioned reduction in the magnitude of the reversed flow can be attributed to higher levels of streamwise Reynolds shear stresses ($\boldsymbol{u'^*v'^*}$) compared to the baseline case as can be seen in ensemble-averaged maps of spanwise shear stress distribution in Figure 95 and Figure 96. Multi plane measurements by Dell'Orso et al.[51] indicate that in a 2-D flow, the streamwise shear stress distribution does not vary significantly in the spanwise direction and where the stall cells are present, the highest levels of shear stress are found in the shear layer above the stall cells. Higher levels of streamwise Reynolds shear stress at low excitation frequencies (Figure 95b-d) are likely due to the flow unsteadiness as result of the shedding of coherent structures rather than increases in momentum transport across the separated shear layer which in turn serves to reduce the momentum deficit in the stall cells and sustain the surface topology of the cells[52], [72], as is the case in the high-frequency-excited regime. The increases in streamwise and normal velocity fluctuations (v' and u') in Figure 95b for $St_e = 0.6$ are due to the generation and downstream convection of large-scale structures. In contrast, high-frequency excitation leads to the generation of small-scale structures that disintegrate quickly and thus, the amplitude of v' and u' and consequently streamwise Reynolds shear stress is clearly lower for $St_e = 6.0$, 10.73 and 14.52 as is seen in Figure 96a, c and d. Unfortunately, high levels on noise in the vertical component of velocity data, likely caused by shot to shot variations in laser output power, completely masks the features of the flow field from $z/b = 0.2$ to 0.4. However, if the unrealistically high levels of noise-induced shear stress concentrations are discarded, a clear pattern in the data, , described

in what follows, starts to emerge. At the low- to medium-frequency excitation regime, high levels of shear stress are due to flow unsteadiness rather than moment transport. As the excitation frequency is increased and the stall cells begin to emerge, the flow unsteadiness disappears due to the weakening of the shedding and early breakdown of the coherent structures. At the same time, this reduction in magnitude of u' and v' is compensated by the well-documented[49], [51] increases in shear stress concentrations above the stall cells. As the excitation frequency is increased, the stall cells become more well-defined and the magnitude of the fluctuating components of velocity, which have been dropped to their minimum due to the disappearance of the shedding at the laser sheet plane at $St_e = 6.0$, begin to increase again as seen in Figure 96.

It must be noted that Manolesos and Voutsinas[49], Disotell[72] and Dell'Orso et al.[51] reported the maximum values of normalized streamwise shear stress above the stall cells in their studies to be from 0.04 to 0.07 which is somewhat consistent with the highest levels of shear stress seen in Figure 96a, b and d where well-defined stall cells are present.
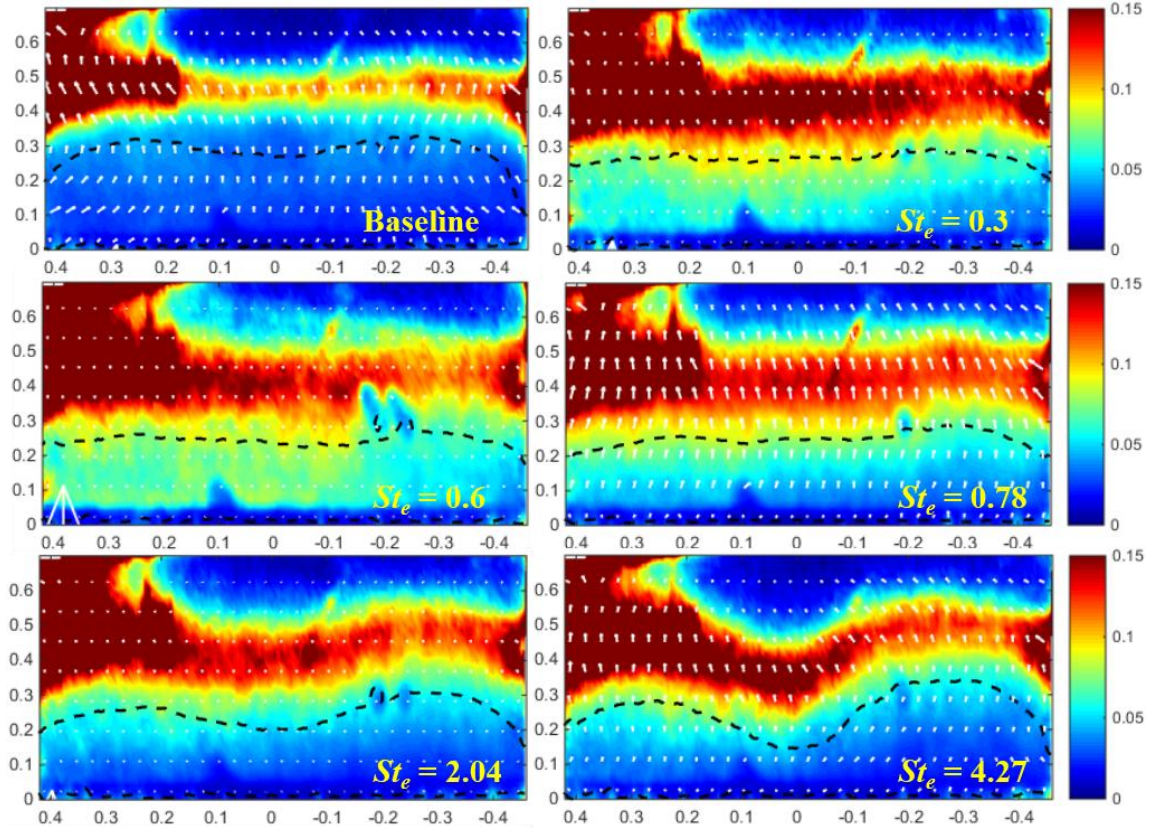
Figure 95. Color maps of normalized ensemble-averaged shear stress $u'^* v'^*$ on a cross-stream plane at x/c =1.05 for $\alpha = 19°$ and Re = 0.5×10^6 for low to mid-frequency excitation regimes. Dashed black lines indicate zero streamwise velocity
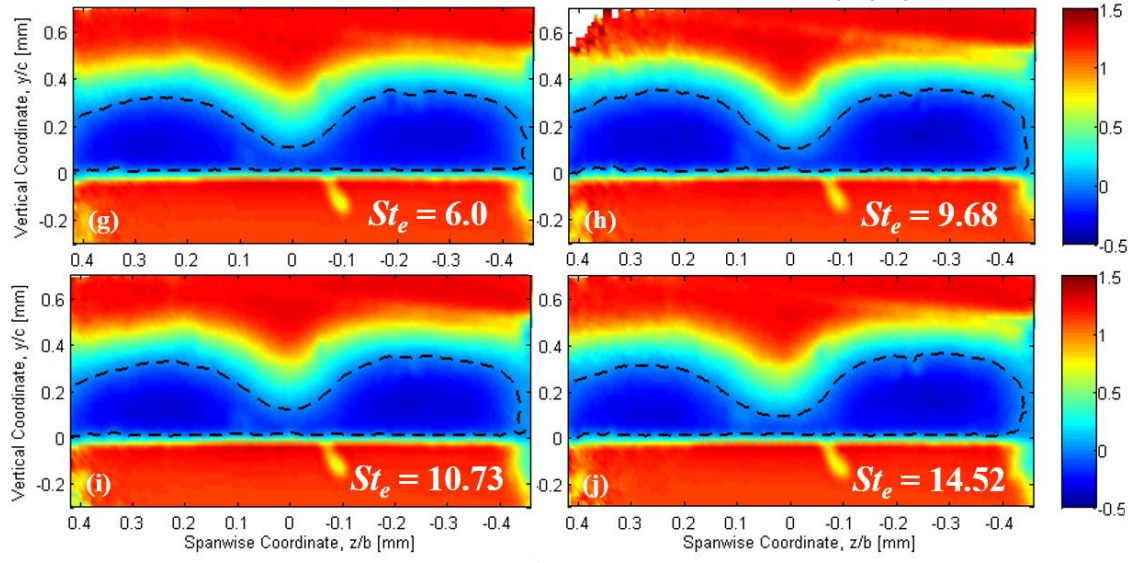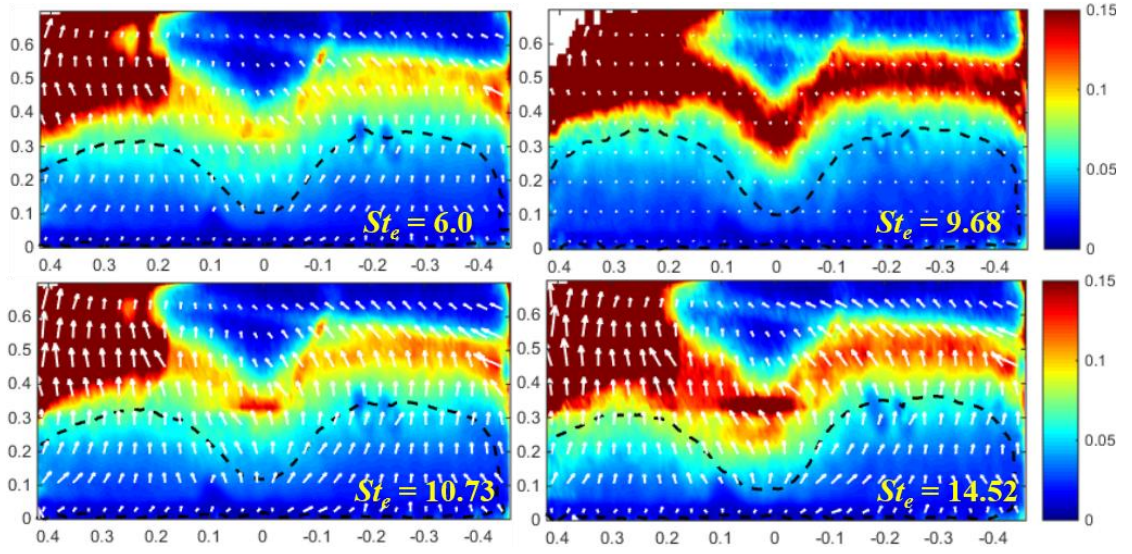
Figure 96. Color maps of normalized ensemble-averaged shear stress $\boldsymbol{u'^*v'^*}$ on a cross-stream plane at x/c =1.05 for α = 19° and Re = 0.5×10^6 for high-frequency excitation regime. Dashed black lines indicate zero streamwise velocity

### 4.3.2 Modulated Excitation of the Flow Field

The Experiments conducted by Dawson and Little[28] [29]indicate that an increase in discharge pulse repetition rate would increase the total amount of energy coupled to the flow by the discharge. Although the amplitude of thermal perturbations (measured by rotational-translational (R-T) temperature of nitrogen and dry air by Montello et al.[78]) generated by a single pulse due to vibrational-translational (V-T) relaxation might increase due to marginal increases in the current drawn by the discharge, the main reason behind the effects reported by Dawson and Little might be the higher number of total pulses in a specific period of time meaning that the total perturbation amplitude and the energy coupled to the flow would higher as the frequency is increased. This suggests that a cumulative effect might be at play. On the other hand, when exciting the flow instabilities, the amplitude of the first pulse is crucial[79] and the total energy coupled to the flow might not be relevant. To ascertain whether the emergence of stall cells is related to an increase in the perturbation amplitude or the frequency content of the excitation signal, a limited series of experiments were conducted where a high-frequency carrier waveform was modulated with a low pulse-repetition rate excitation signal. The frequency of the square carrier waveform in these experiments was fixed at 2 kHz (St_e = 10.97).

Velocity distribution maps and surface pressure distributions with and without modulated excitation were acquired and are presented in the following section to further explore the

characteristics of the introduced perturbation environment which is responsible for the formation of the stall cells.

Cross-stream maps of normalized components of velocity for cases excited only at St_e = 0.6, and the cases where the carrier excitation signal (St_e = 10.97) is modulated by St_e = 0.6 are presented Figure 97. Excitation in the low-frequency regime, as mentioned previously, results in a nearly two-dimensional distribution downstream of the trailing edge as can be seen in Figure 97c and d. However, in the modulated case, the distinct, asymmetric spanwise distribution associated with stall cells previously seen in high frequency cases (Figure 91 and Figure 92e-j) emerges (see Figure 97e and f). It is interesting to note that while the magnitude of the streamwise component of the flow has not changed, the magnitude of the vertical component of velocity has increased significantly. As mentioned previously, the formation of stall cells leads to an increase in v' above the stall cells but not v.

The total in-plane velocity maps, in agreement with colormaps of normal velocity distribution, suggest that the modulated case leads to not only stronger shedding, but also a 3-D flow field. As St_e = 0.6 is close to the most amplified frequency in this flow conditions, it is possible that higher amplitude of excitation leads to the generation of stronger large-scale coherent structures in addition to inducing stall cells. Acquiring phase-locked, streamwise PIV data for the modulated cases could help to verify this.

Results of modulating the carrier waveform at an excitation frequency corresponding to St_e = 4.27 are presented in Figure 98. Here, a well-defined, asymmetric pattern already exists when the flow is excited by the non-modulated signal (Figure 91). Although the modulated cases have stall cells of the same size and shape as the non-modulated case, the introduction of a modulated signal does reduce the separation height in the mid-span location and the streamwise flow magnitude above the stall cells from y/c = 0.4 to 0.6 (see Figure 98e and j). The amplitude of the normal component of the velocity has also reduced significantly indicating that the coherent structures breakdown and dissipate much earlier than was the case for St_e = 4.27. The marginal reductions in the magnitude of the revered flow inside the stall cells might indeed be the result of better moment transport across the shear layer that accompanies well-defined stall cells previously seen under high-frequency excitation. The marginal reduction in the separation height is also a tell-tale sign of a well-defined stall cell. So, it appears that by modulating the a high-frequency carrier waveform, the flow field responds as if it is excited by the carrier waveform frequency and not the modulation frequency. Although it is not possible to exclusively determine whether the observed effects have their roots in the frequency content or amplitude of the excitation based on the data provided here, it appears that the frequency content, be it in the unmodulated or modulated form, plays a major role in inducing stall cells.
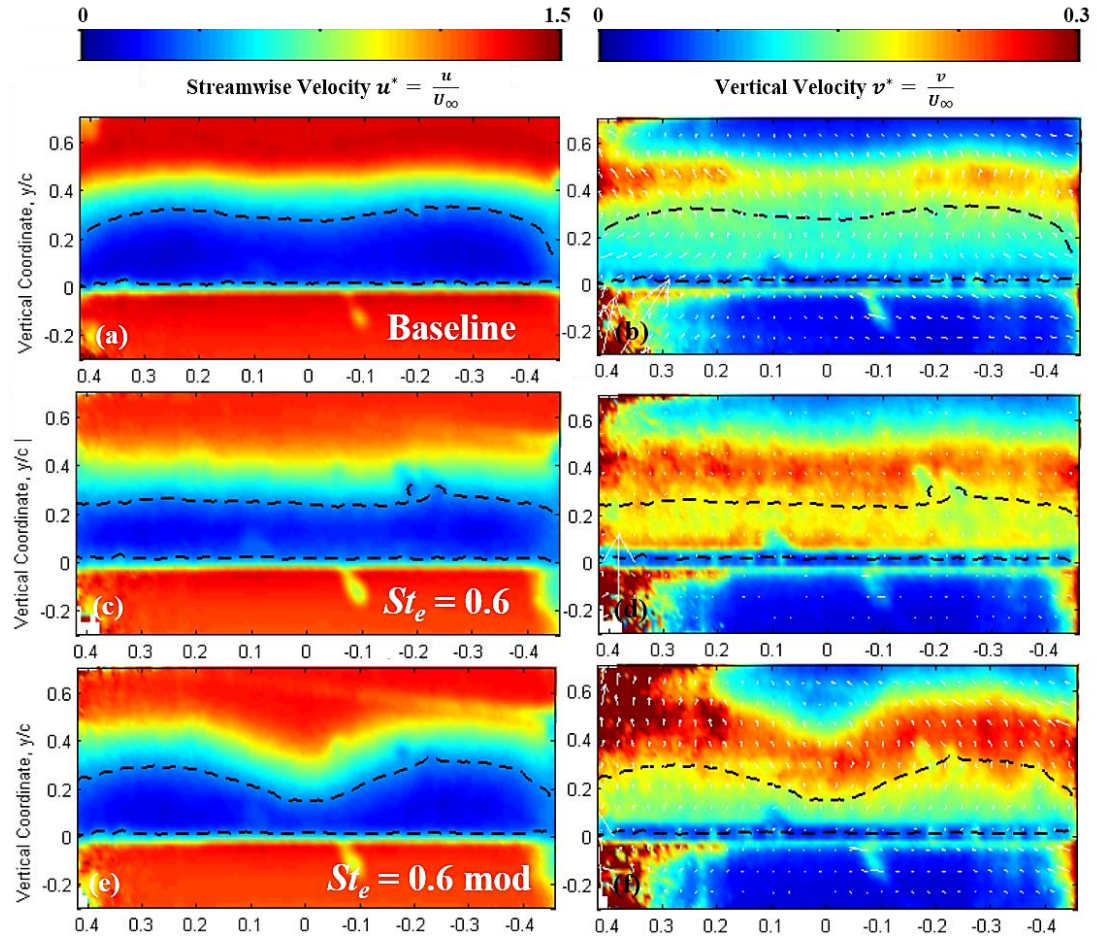
Figure 97. Color maps of normalized ensemble-averaged velocity on a cross-stream plane

at *x/c* =1.05 superimposed on total, in-plane velocity vectors at α = 19° and Re = 0.5×10⁶

for baseline, modulated and non-modulated excitation at St_e = 0.6

158
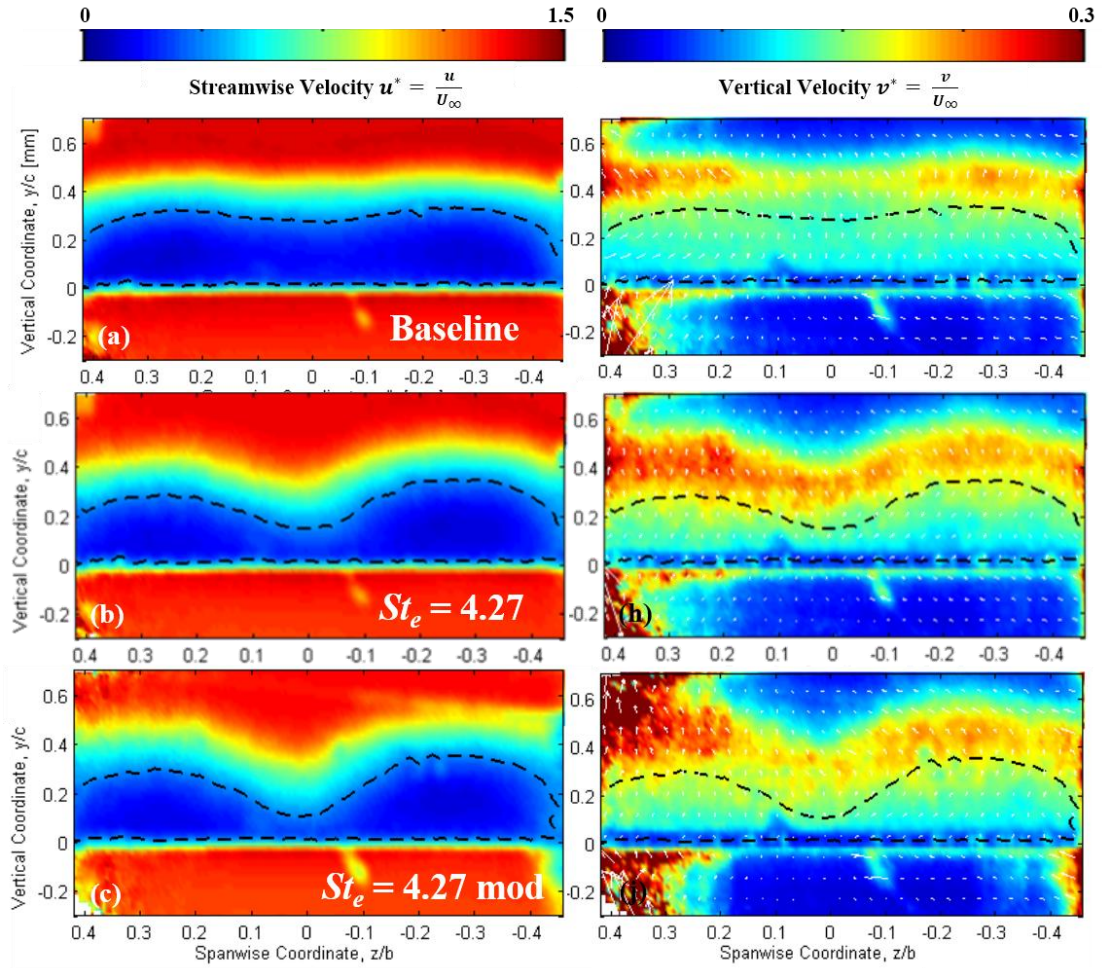
Figure 98. Color maps of normalized ensemble-averaged velocity on a cross-stream plane
at x/c =1.05 superimposed on total, in-plane velocity vectors at α = 19° and Re = 0.5×10^6
for baseline, modulated and non-modulated excitation at St_e = 4.27

159

Examining the plots of surface pressure distribution for modulated and non-modulated cases further illustrates the role of excitation signal modulation in flow field development. Comparing the modulated excitation data presented in Figure 99, with non-modulated data, it is readily evident that modulating a high-frequency carrier signal results in effects similar to that of high-frequency excitation, namely the sharp suction peak close to the leading edge. The magnitude of the suction peak, even for the low-frequency excitation cases, is comparable to that observed in non-modulated high-frequency cases. As is the case with high-frequency excitation regime, the rapid development of small-scale structures and their early breakdown leads to a sharp drop in negative pressure. These observations further support the hypothesis that the flow field, most likely, responds to the frequency content of the carrier waveform and not the modulation signal frequency.

160
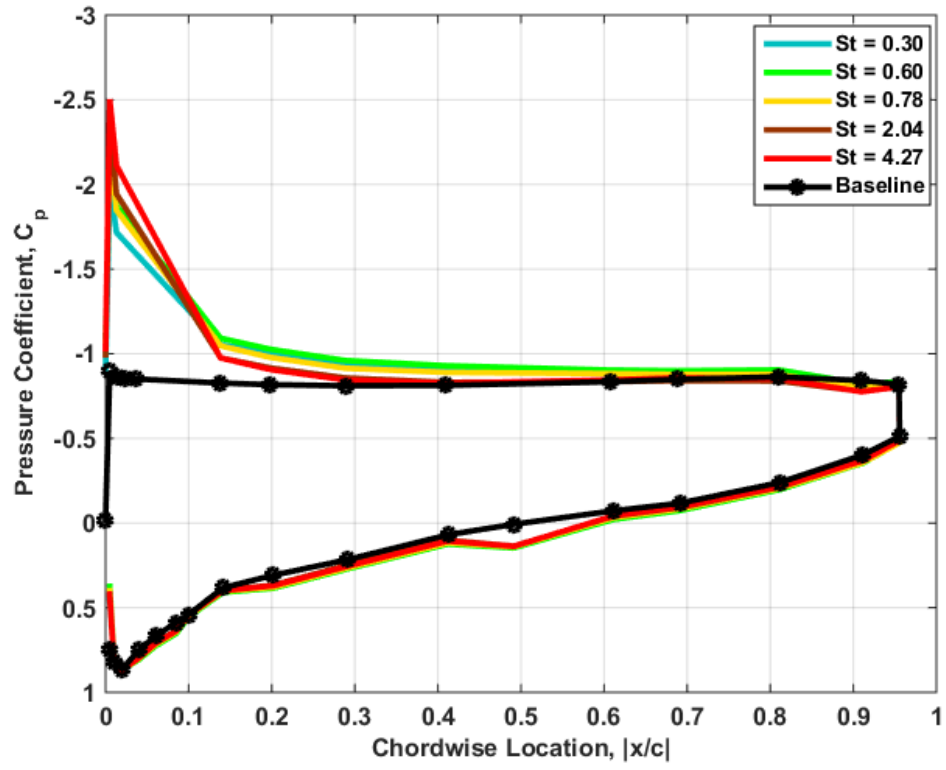
Figure 99. Pressure coefficient distribution for baseline and frequency modulated cases (2 kHz carrier signal) at α = 19° and Re = 0.5×10⁶

Chapter 5: Conclusions and Future Work

5.1 Summary and Conclusions

Flow control experiments were performed using a NS-DBD actuator on a Boeing VR7 airfoil installed in a recirculating wind tunnel such that the flow was fully separated. A 19° angle of attack at a Reynolds number of 0.50×10^6 was selected for detailed investigation. Fully separated flow on the suction side extended well beyond the airfoil with highly asymmetric velocity and vorticity fields and a natural shedding Strouhal number of 0.60. The effects of two excitation regimes, namely low-frequency and high-frequency excitation were explored using streamwise and spanwise ensemble-averaged and phase-locked PIV, wake pressure spectra and surface pressure distribution.

It was found that low-frequency excitation generates large-scale, coherent structures in the shear layer over the separated region, which convect into the wake region. Excitation around St_e =0.6, the shedding Strouhal number, had the most significant effects in the low-frequency excitation regime creating moderately sized structures that convect far downstream and increased the lift and drag. Surface pressure and phase-locked PIV data suggest that convection of these structures along the chord of the airfoil results in a nearly

uniform increase in suction in the chordwise direction. The periodic shedding of large-scale structures, as demonstrated by phase-locked PIV data, resulted in unsteadiness in separation line location and the time-dependent ejection of vorticity into to the wake which suggests that the airfoil has been subjected to unsteady and periodic loads as verified by time-resolved pressure measurements. This can be considered the most crucial disadvantage of low-frequency excitation in flow control applications.

In contrast, excitation at higher Strouhal numbers resulted in the formation of a three-dimensional flow field and numerous small-scale structures that contribute significantly to momentum transfer, accelerate the flow close to the surface and move the separation point further downstream. Plots of vorticity indicate that these structures quickly breakdown and disintegrate past the separation line. The absence of organized shedding in the separated shear layer in this regime means that the separation line location is time-independent. Wake pressure spectra for low-frequency excitation cases indicate strong peaks corresponding to large-scale structures were observed phase-locked PIV data whereas the early breakdown of small-scale structures leads to flat spectra in the high-frequency excitation regime. Surface pressure data indicate that small-scale structures generated as result of high-frequency excitation, unlike the large-scale structures that harvest energy from the freestream flow, do not impose a drag penalty on the airfoil and are nearly as efficient in increasing the lift coefficient. In conclusion, high-frequency excitation of flow, based on the empirical evidence, appears to be superior to low-frequency excitation in the function of separation control for the investigated airfoil as

163

comparable results to low-frequency excitation can be achieved without imposing unsteady and cyclic loads on the airfoil. These conclusions are similar to the work of researchers that have investigated the use of synthetic jet actuators in various excitation regimes. Thus, it can be concluded that the physical processes and the control mechanisms are the same regardless of the actuator employed to create the perturbations.

In the second part of this work, the emergence of three-dimensional features due to excitation at mid to high-frequencies was explored. The discrepancies between result from different diagnostics at various spanwise locations gave rise to this suspicion. While the existence of stall cells over thick airfoils at shallow post-stall angles is well-documented in the literature, the results of this work indicate that appropriate disturbance environments are conducive to the emergence of stall cells even over thin airfoils at deep post-stall angles. The overall features of the three-dimensional flow fields were investigated primarily with streamwise planar and spanwise stereo PIV measurements and complimentary surface oil flow visualization. The flow was excited using NS-DBD actuators over a large range of Strouhal numbers. A spanwise three-dimensional separation front was observed in the surface oil flow visualization images of the baseline flow while stereo PIV data acquired downstream of the trailing edge indicated the presence of a quasi-two-dimensional flow field. Low-frequency excitation of the flow led to the emergence of two asymmetrical stall cells with well-defined spiral nodes over the airfoil with the flow field downstream of the trailing edge being nearly two-dimensional throughout the low-frequency excitation sweep. The strong, spanwise coherent structures

generated by low-frequency excitation, which entrain high-momentum freestream flow into the separated region and reduce the size of separation, are believed to confine the three-dimensional flow features, clearly visible in the surface flow visualization data, to the near-wall region. High-frequency excitation resulted in generation of smaller coherent-structures, which are developed further upstream in the shear layer, and the emergence of distinct, asymmetrical, mushroom-shaped cells over the airfoil. The magnitude of the reversed flow in the cells was also increased due to inefficient transport of momentum across the shear layer, by the small-scale structures generated by the excitation. Modulation of a high-frequency carrier waveform with a low-frequency excitation signal also resulted in the emergence of stall cells. It is believed that the perturbation environment created by the NS-DBD actuators is responsible for the emergence of stall cells in flow conditions where appearance of these features was previously perceived to be unlikely. Since the perturbations were used to excite instability of the shear layer over the separated region, which lead to the appearance of stall cells, the results seem to show a strong connection between these cells and the shear layer instability. However, more research is needed to provide additional information and better understanding of the connection. These findings also show the power of using actuators as flow diagnostic as well as flow control tools.

5.2 Recommendations and Future Work

Perhaps the most significant aspect of this work is the discovery, for the first time in the flow control community, that perturbing the massively separated flow fields over a thin

airfoil will lead to the emergence of stall cells. Several avenues of research can be followed to further investigate the findings of this work. As the thin, curved airfoils are widely used in rotorcraft blades, which experience dynamics stall, it would be interesting to find out whether there are critical conditions at which the stall cells are present over a thin, baseline airfoil in dynamic stall – as is the case with thick airfoils in static stall – and also see if exciting the flow in the mid to high-frequency regime would lead to their emergence. Since stall cells are known to be present over high aspect ratio blades of wind turbines, understanding the underlying physics of their formation would garner immense interest. Clearly, as demonstrated in this work, this calls for extensive 3-D diagnostics of the flow field and the use of new diagnostic techniques such as PSP and fluorescent flow visualization at GDTL for the first time during the course of this work has laid the necessary foundations for further implementation of these techniques. The use of pressure sensitive paint and low-viscosity oil for visualizing the surface topology during dynamic stall experiments would outline a complete picture of the flow field and thus provide a better understanding of the flow physics.

As mentioned in regards to the mechanisms of stall cell emergence under high-frequency excitation, further work in needed to establish the dominant factor in the appearance of stall cells. Conducting experiments where the perturbation amplitude is varied greatly, would be helpful in establishing whether perturbation amplitude plays an important role or not.

The composite airfoil used in this work was not suited for PSP measurements due to its structural qualities and poor heat conduction. Efforts are currently underway at GDTL to design and fabricate a hollow metal airfoil for PSP measurements. Also, the issue of intrusive exposed electrodes must be addressed as the emergence of stall cells can be triggered by passive geometrical disturbances as well as active perturbations. The technique for fabricating circuit-printed electrodes, which was briefly examined in this work, must be perfected and the future experiments must be conducted with "non-intrusive" electrodes to ensure that they are not part of the "disturbance environment".

Further changes to the control systems of the low-speed facility at GDTL have to be made to ensure their robustness for future experiments. Numerous breakdowns and software crashes greatly hindered the earlier parts of this project. Nevertheless, automating the facility is of great importance as it enables the operator to conduct vast sweeps in large parameter spaces and increases productivity while eliminating human error.

References

[1] J. G. Leishman, *Principles of Helicopter Aerodynamics*, 2nd ed. Cambridge University Press, 2006.

[2] E. Moreau, "Airflow control by non-thermal plasma actuators," *J. Phys. Appl. Phys.*, vol. 40, no. 3, p. 605, 2007.

[3] M. Samimy, I. Adamovich, B. Webb, J. Kastner, J. Hileman, S. Keshav, P. Palm "Development and characterization of plasma actuators for high-speed jet control," *Exp. Fluids*, vol. 37, no. 4, pp. 577–588, Aug. 2004.

[4] N. Benard and E. Moreau, "Capabilities of the dielectric barrier discharge plasma actuator for multi-frequency excitations," *J. Phys. Appl. Phys.*, vol. 43, no. 14, p. 145201, 2010.

[5] F. O. Thomas, T. C. Corke, M. Iqbal, A. Kozlov, and D. Schatzman, "Optimization of Dielectric Barrier Discharge Plasma Actuators for Active Aerodynamic Flow Control," *AIAA J.*, vol. 47, no. 9, pp. 2169–2178, 2009.

[6] M. P. Patel, T. C. Corke, "Scaling Effects of an Aerodynamic Plasma Actuator," *J. Aircr.*, vol. 45, no. 1, pp. 223–236, 2008.

[7] M. Wicks, T. C. Corke, "A Parametric Investigation of Plasma Streamwise Vortex Generator Performance," in *50th AIAA Aerospace Sciences Meeting including the New Horizons Forum and Aerospace Exposition*, American Institute of Aeronautics and Astronautics.

[8] M. Wicks, F. O. Thomas, T. C. Corke, M. Patel, and A. B. Cain, "Mechanism of Vorticity Generation in Plasma Streamwise Vortex Generators," *AIAA J.*, vol. 53, no. 11, pp. 3404–3413, 2015.

[9] C. L. Kelley, T. C. Corke, "Leading-Edge Separation Control Using Alternating-Current and Nanosecond-Pulse Plasma Actuators," *AIAA J.*, vol. 52, no. 9, pp. 1871–1884, 2014.

[10] D. Roupassov, I. Zavialov, and A. Starikovskii, "Boundary Layer Separation Plasma Control Using Low-Temperature Non-Equilibrium Plasma of Gas Discharge," in *44th AIAA Aerospace Sciences Meeting and Exhibit*, American Institute of Aeronautics and Astronautics.

[11] D. Roupassov, A. Starikovskii, A. Nikipelov, and M. Nudnova, "Boundary Layer Separation Control by Nanosecond Plasma Actuator," in *44th AIAA/ASME/SAE/ASEE Joint Propulsion Conference & Exhibit*, American Institute of Aeronautics and Astronautics.

[12] D. V. Roupassov, A. A. Nikipelov, M. M. Nudnova, and A. Y. Starikovskii, "Flow Separation Control by Plasma Actuator with Nanosecond Pulsed-Periodic Discharge," *AIAA J.*, vol. 47, no. 1, pp. 168–185, 2009.

[13] A. Marino, P. Catalano, C. Marongiu, P. Peschke, C. Hollenstein, and R. Donelli, "Effects of High Voltage Pulsed DBD on the Aerodynamic Performances in Subsonic and Transonic Conditions," in *43rd Fluid Dynamics Conference*, American Institute of Aeronautics and Astronautics.

[14] P. Peschke, S. Goekce, P. Leyland, P. Ott, and C. Hollenstein, "Experimental Investigation of Pulsed Dielectric Barrier Discharge Actuators in Sub- and Transonic Flow," in *44th AIAA Plasmadynamics and Lasers Conference*, American Institute of Aeronautics and Astronautics.

[15] J. Little, K. Takashima, M. Nishihara, I. Adamovich, and M. Samimy, "High Lift Airfoil Leading Edge Separation Control with Nanosecond Pulse DBD Plasma Actuators," in *5th Flow Control Conference*, American Institute of Aeronautics and Astronautics.

[16] I. Adamovich, J. Little, M. Nishihara, K. Takashima, and M. Samimy, "Nanosecond Pulse Surface Discharges for High-Speed Flow Control," in *6th AIAA Flow Control Conference*, American Institute of Aeronautics and Astronautics.

[17] C. Rethmel, J. Little, K. Takashima, A. Sinha, I. Adamovich, and M. Samimy, "Flow Separation Control over an Airfoil with Nanosecond Pulse Driven DBD Plasma Actuators," in *49th AIAA Aerospace Sciences Meeting including the New Horizons Forum and Aerospace Exposition*, American Institute of Aeronautics and Astronautics.

[18] M. Nishihara, K. Takashima, J. W. Rich, and I. V. Adamovich, "Mach 5 bow shock control by a nanosecond pulse surface dielectric barrier discharge," *Phys. Fluids 1994-Present*, vol. 23, no. 6, p. 066101, Jun. 2011.

[19] J. Little, K. Takashima, M. Nishihara, I. Adamovich, and M. Samimy, "Separation Control with Nanosecond-Pulse-Driven Dielectric Barrier Discharge Plasma Actuators," *AIAA J.*, vol. 50, no. 2, pp. 350–365, 2012.

[20] X. Che, T. Shao, W. Nie, and P. Yan, "Numerical simulation on a nanosecond-pulse surface dielectric barrier discharge actuator in near space," *J. Phys. Appl. Phys.*, vol. 45, no. 14, p. 145201, Apr. 2012.

[21] I. Popov *et al.*, "Experimental Study and Numerical Simulation of Flow Separation Control with Pulsed Nanosecond Discharge Actuator," in *51st AIAA Aerospace Sciences Meeting including the New Horizons Forum and Aerospace Exposition*, American Institute of Aeronautics and Astronautics.

[22] G. Correale, I. Popov, A. Rakitin, A. Starikovskii, S. Hulshoff, and L. Veldhuis, "Flow Separation Control on Airfoil With Pulsed Nanosecond Discharge Actuator," in *49th AIAA Aerospace Sciences Meeting including the New Horizons Forum and Aerospace Exposition*, American Institute of Aeronautics and Astronautics.

[23] A. Y. Starikovskii, A. A. Nikipelov, M. M. Nudnova, and D. V. Roupassov, "SDBD plasma actuator with nanosecond pulse-periodic discharge," *Plasma Sources Sci. Technol.*, vol. 18, no. 3, p. 034015, 2009.

[24] K. Takashima, Y. Zuzeek, W. Lempert, and I. Adamovich, "Characterization of Surface Dielectric Barrier Discharge Plasma Sustained by Repetitive Nanosecond Pulses," in *41st Plasmadynamics and Lasers Conference*, American Institute of Aeronautics and Astronautics.

[25] K. Takashima (Udagawa), Y. Zuzeek, W. R. Lempert, and I. V. Adamovich, "Characterization of a surface dielectric barrier discharge plasma sustained by repetitive nanosecond pulses," *Plasma Sources Sci. Technol.*, vol. 20, no. 5, p. 055009, Oct. 2011.

[26] S. B. Leonov, V. Petrishchev, and I. V. Adamovich, "Dynamics of energy coupling and thermalization in barrier discharges over dielectric and weakly conducting surfaces on μ s to ms time scales," *J. Phys. Appl. Phys.*, vol. 47, no. 46, p. 465201, 2014.

[27] D. J. Akins, A. Singh, and J. C. Little, "Effects of Pulse Energy on Shear Layer Control using Surface Plasma Discharges," in *45th AIAA Fluid Dynamics Conference*, American Institute of Aeronautics and Astronautics.

[28] R. Dawson and J. Little, "Characterization of nanosecond pulse driven dielectric barrier discharge plasma actuators for aerodynamic flow control," *J. Appl. Phys.*, vol. 113, no. 10, p. 103302, Mar. 2013.

[29]   R. A. Dawson and J. Little, "Effects of pulse polarity on nanosecond pulse driven dielectric barrier discharge plasma actuators," *J. Appl. Phys.*, vol. 115, no. 4, p. 043306, Jan. 2014.

[30]   P. Peschke, S. Goekce, C. Hollenstein, P. Leyland, and P. Ott, "Interaction Between Nanosecond Pulse DBD Actuators and Transonic Flow," in *42nd AIAA Plasmadynamics and Lasers Conference*, American Institute of Aeronautics and Astronautics.

[31]   D. Greenblatt and I. Wygnanski, "Effect of Leading-Edge Curvature on Airfoil Separation Control," *J. Aircr.*, vol. 40, no. 3, pp. 473–481, 2003.

[32]   K. Sunneechurra and W. J. Crowther, "Problems with Leading-Edge Flow Control Experiments," *J. Aircr.*, vol. 44, no. 3, pp. 1052–1055, 2007.

[33]   M. Amitay and A. Glezer, "Role of Actuation Frequency in Controlled Flow Reattachment over a Stalled Airfoil," *AIAA J.*, vol. 40, no. 2, pp. 209–216, 2002.

[34]   A. Glezer, M. Amitay, and A. M. Honohan, "Aspects of Low- and High-Frequency Actuation for Aerodynamic Flow Control," *AIAA J.*, vol. 43, no. 7, pp. 1501–1511, 2005.

[35]   M. Amitay, D. R. Smith, V. Kibens, D. E. Parekh, and A. Glezer, "Aerodynamic Flow Control over an Unconventional Airfoil Using Synthetic Jet Actuators," *AIAA J.*, vol. 39, no. 3, pp. 361–370, 2001.

[36]   D. Smith, M. Amitay, V. Kibens, D. Parekh, and A. Glezer, "Modification of lifting body aerodynamics using synthetic jet actuators," in *36th AIAA Aerospace Sciences Meeting and Exhibit*, American Institute of Aeronautics and Astronautics.

[37]   M. Amitay, M. Horvath, M. Michaux, and A. Glezer, "Virtual aerodynamic shape modification at low angles of attack using synthetic jet actuators," in *15th AIAA Computational Fluid Dynamics Conference*, American Institute of Aeronautics and Astronautics.

[38]   A. Seifert, A. Darabi, and I. Wyganski, "Delay of airfoil stall by periodic excitation," *J. Aircr.*, vol. 33, no. 4, pp. 691–698, 1996.

[39]   G. B. Mccullough and D. E. Gault, "Examples of Three Representative Types of Airfoil-section Stall at Low Speed," Sep. 1951.

[40]   P. R. Spalart, "Prediction of Lift Cells for Stalling Wings by Lifting-Line Theory," *AIAA J.*, vol. 52, no. 8, pp. 1817–1821, 2014.

[41]   D. Ragni and C. Ferreira, "Effect of 3-D stall-cells on the pressure distribution of a laminar NACA64-418 wing," *Exp. Fluids*, vol. 57, no. 8, p. 127, Aug. 2016.

[42] N. Gregory, "Progress report on observations of three-dimensional flow patterns obtained during stall development on aerofoils, and on the problem of measuring two-dimensional characteristics." British A.R.C.C.P . 1146, 1971.

[43] A. E. Winkelman and J. B. Barlow, "Flowfield Model for a Rectangular Planform Wing beyond Stall," *AIAA J.*, vol. 18, no. 8, pp. 1006–1008, 1980.

[44] D. Weihs and J. Katz, "Cellular patterns in poststall flow over unswept wings," *AIAA J.*, vol. 21, no. 12, pp. 1757–1759, 1983.

[45] A. V. Boiko, A. V. Dovgal, Y. B. Zanin, and V. V. Kozlov, "Three-dimensional structure of separated flows on wings (review)," *Thermophys. Aeromechanics*, vol. 3, no. 1, pp. 1–13, Jan. 1996.

[46] S. A. Yon and J. Katz, "Study of the Unsteady Flow Features on a Stalled Wing," *AIAA J.*, vol. 36, no. 3, pp. 305–312, 1998.

[47] A. P. Broeren and M. B. Bragg, "Spanwise Variation in the Unsteady Stalling Flowfields of Two-Dimensional Airfoil Models," *AIAA J.*, vol. 39, no. 9, pp. 1641–1651, 2001.

[48] G. Schewe, "Reynolds-number effects in flow around more-or-less bluff bodies," *J. Wind Eng. Ind. Aerodyn.*, vol. 89, no. 14–15, pp. 1267–1289, Dec. 2001.

[49] M. Manolesos and S. G. Voutsinas, "Study of a stall cell using stereo particle image velocimetry," *Phys. Fluids 1994-Present*, vol. 26, no. 4, p. 045101, Apr. 2014.

[50] E. P. Demauro, H. Dell'Orso, V. Sivaneri, B. Tuna, and M. Amitay, "Measurements of 3-D Stall Cells on 2-D Airfoil," in *45th AIAA Fluid Dynamics Conference*, American Institute of Aeronautics and Astronautics.

[51] H. Dell'Orso, B. A. Tuna, and M. Amitay, "Measurement of Three-Dimensional Stall Cells on a Two-Dimensional NACA0015 Airfoil," *AIAA J.*, vol. 54, no. 12, pp. 3872–3883, 2016.

[52] K. J. Disotell and J. Gregory, "Time-Resolved Measurements of Cellular Separation on a Stalling Airfoil," in *53rd AIAA Aerospace Sciences Meeting*, American Institute of Aeronautics and Astronautics.

[53] K. J. Disotell, P. Nikoueeyan, J. W. Naughton, and J. W. Gregory, "Global surface pressure measurements of static and dynamic stall on a wind turbine airfoil at low Reynolds number," *Exp. Fluids*, vol. 57, no. 5, p. 82, May 2016.

[54] S. C. Crow, "Stability theory for a pair of trailing vortices," *AIAA J.*, vol. 8, no. 12, pp. 2172–2179, 1970.

[55] D. Rodríguez and V. Theofilis, "On the birth of stall cells on airfoils," *Theor. Comput. Fluid Dyn.*, vol. 25, no. 1–4, pp. 105–117, Jun. 2011.

[56] H. Dell'Orso, W. Chan, and M. Amitay, "Induced Stall Cells on a NACA0015 Airfoil using Passive and Active Trips," in *8th AIAA Flow Control Conference*, American Institute of Aeronautics and Astronautics.

[57] D. M. Driver, H. L. Seegmiller, and J. G. Marvin, "Time-dependent behavior of a reattaching shear layer," *AIAA J.*, vol. 25, no. 7, pp. 914–919, 1987.

[58] M. Samimy, J.-H. Kim, J. Kastner, I. Adamovich, and Y. Utkin, "Active control of high-speed and high-Reynolds-number jets using plasma actuators," *J. Fluid Mech.*, vol. 578, pp. 305–330, May 2007.

[59] M. Stanislas, K. Okamoto, C. J. Kähler, J. Westerweel, and F. Scarano, "Main results of the third international PIV Challenge," *Exp. Fluids*, vol. 45, no. 1, pp. 27–71, Apr. 2008.

[60] R. J. Adrian, K. T. Christensen, and Z.-C. Liu, "Analysis and interpretation of instantaneous turbulent velocity fields," *Exp. Fluids*, vol. 29, no. 3, pp. 275–290, Sep. 2000.

[61] C. J. Clifford, "An Investigation of Physics and Control of Flow Passing a NACA 0015 in Fully-Reversed Condition," The Ohio State University, 2015.

[62] A. K. Prasad, "Stereoscopic particle image velocimetry," *Exp. Fluids*, vol. 29, no. 2, pp. 103–116, Aug. 2000.

[63] G. S. Settles, *Schlieren and Shadowgraph Techniques - Visualizing Phenomena in Transparent Media*. Springer Berlin Heidelberg, 2001.

[64] M. J. Hargather and G. S. Settles, "A comparison of three quantitative schlieren techniques," *Opt. Lasers Eng.*, vol. 50, no. 1, pp. 8–17, Jan. 2012.

[65] K. W. McAlister, "Application of the ONERA Model."

[66] K. W. Mcalister, S. L. Pucci, W. J. Mccroskey, and L. W. Carr, "An experimental study of dynamic stall on advanced airfoil section. Volume 2: Pressure and force data," Sep. 1982.

[67] K. W. Mcalister and C. Tung, "Suppression of dynamic stall with a leading-edge slat on a VR-7 airfoil," Mar. 1993.

[68] K. Disotell, "Low-Frequency Flow Oscillations on Stalled Wings Exhibiting Cellular Separation Topology," PhD thesis, The Ohio State University, 2015.

[69]   S. Yarusevych, P. E. Sullivan, and J. G. Kawall, "On vortex shedding from an airfoil in low-Reynolds-number flows," *J. Fluid Mech.*, vol. 632, pp. 245–271, Aug. 2009.

[70]   A. V. Dovgal, V. V. Kozlov, and A. Michalke, "Laminar boundary layer separation: Instability and associated phenomena," *Prog. Aerosp. Sci.*, vol. 30, no. 1, pp. 61–94, 1994.

[71]   T. J. Mueller, "The influence of laminar separation and transition on low Reynolds number airfoil hysteresis," *J. Aircr.*, vol. 22, no. 9, pp. 763–770, 1985.

[72]   K. J. Disotell, "Low-Frequency Flow Oscillations on Stalled Wings Exhibiting Cellular Separation Topology," The Ohio State University, 2015.

[73]   A. Esfahani, A. Singhal, C. J. Clifford, and M. Samimy, "Flow Separation Control over a Boeing Vertol VR-7 using NS-DBD Plasma Actuators," in *54th AIAA Aerospace Sciences Meeting*, American Institute of Aeronautics and Astronautics.

[74]   A. Gross, H. F. Fasel, and M. Gaster, "Criterion for Spanwise Spacing of Stall Cells," *AIAA J.*, vol. 53, no. 1, pp. 272–274, 2015.

[75]   M. Manolesos, G. Papadakis, and S. G. Voutsinas, "Experimental and computational analysis of stall cells on rectangular wings," *Wind Energy*, vol. 17, no. 6, pp. 939–955, Jun. 2014.

[76]   D. Rockwell and E. Naudascher, "Review—Self-Sustaining Oscillations of Flow Past Cavities," *J. Fluids Eng.*, vol. 100, no. 2, pp. 152–165, Jun. 1978.

[77]   M. Manolesos, G. Papadakis, and S. G. Voutsinas, "Experimental and computational analysis of stall cells on rectangular wings," *Wind Energy*, vol. 17, no. 6, pp. 939–955, Jun. 2014.

[78]   A. Montello, D. Burnette, and I. Adamovich, "Dynamics of Rapid Localized Heating in Nanosecond Pulse Discharges for High Speed Flow Control," *J. Fluid Sci. Technol.*, vol. 8, no. 2, pp. 147–159, 2013.

[79]   M. Samimy, J.-H. Kim, J. Kastner, I. Adamovich, and Y. Utkin, "Active control of high-speed and high-Reynolds-number jets using plasma actuators," *J. Fluid Mech.*, vol. 578, pp. 305–330, May 2007.

[80]   G. Correale, R. Winkel, and M. Kotsonis, "Energy Deposition Characteristics of Nanosecond Dielectric Barrier Discharge Plasma Actuators: Influence of Dielectric Material," *J. Appl. Phys.*, vol. 118, no. 8, p. 083301, Aug. 2015.

[81]   R. Prescott, "A Method of Correction of Astigmatism in Schlieren Systems," *J. Aeronaut. Sci.*, vol. 18, no. 1, pp. 69–69, 1951.

[82]   G. Settles, *Schlieren and Shadowgraph Techniques: Visualizing Phenomena in Transparent Media*, Softcover reprint of the original 1st ed. 2001 edition. Springer, 2012.

[83]   C. Alvarez-Herrera, D. Moreno-Hernández, B. Barrientos-García, and J. A. Guerrero-Viramontes, "Temperature measurement of air convection using a Schlieren system," *Opt. Laser Technol.*, vol. 41, no. 3, pp. 233–240, Apr. 2009.

Appendix A: Schlieren System Alignment and Calibration

A.1 Introduction

As a precursor to deflectometry test campaign, the beam deflection angles on the setup were adjusted several times to bring the angles to the lowest possible value in order to reduce astigmatism, a calibration tool was constructed and briefly tested and 2nd order calibration curve equations were obtained for the pixels throughout the image.

A.2 Beam deflection adjustment

One of the most important drawbacks of Z-type Schlieren methods is coma and astigmatism that is generated due to off-axis beam deflection. For qualitative measurements, the effects of these phenomena might not be too detrimental and probably will be evident in the form of glare in the Schlieren image. Prescott[81] has proposed a method to correct these effects using a special lens but that approach leads to lower system resolution. As generally acknowledged by Settles[82], the best approach is to reduce off-axis beam deflection angles as much as possible. Astigmatic effects in the knife edge plane can be seen in Figure A.1.
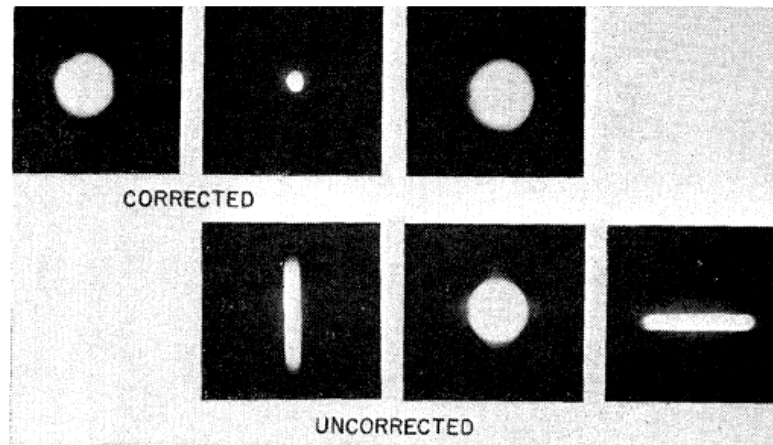
Figure A.1 Astigmatic effects in knife edge pane in a) corrected setup b) uncorrected

setup

So, before embarking on system calibration, it was deemed necessary to reduce astigmatic effects, which would potentially introduce uncertainty in temperature measurements, by minimizing the off-axis angles. As mentioned, never before in our work there was a need for such accurate angle measurements and as a result, this procedure has never been carried out. The details of this procedure are outlined in the following section.

A.3 Procedure

The distance between the post holders of optical elements were measured using a laser aligner equipped with a special head to generate vertical lines. The laser lines were placed on post holders and then the distance between laser projections on the tunnel acrylic wall was measured using a ruler. For measurements involving parabolic mirrors,

177

the laser line was placed on a marker passing through the center of the mirror. The use of

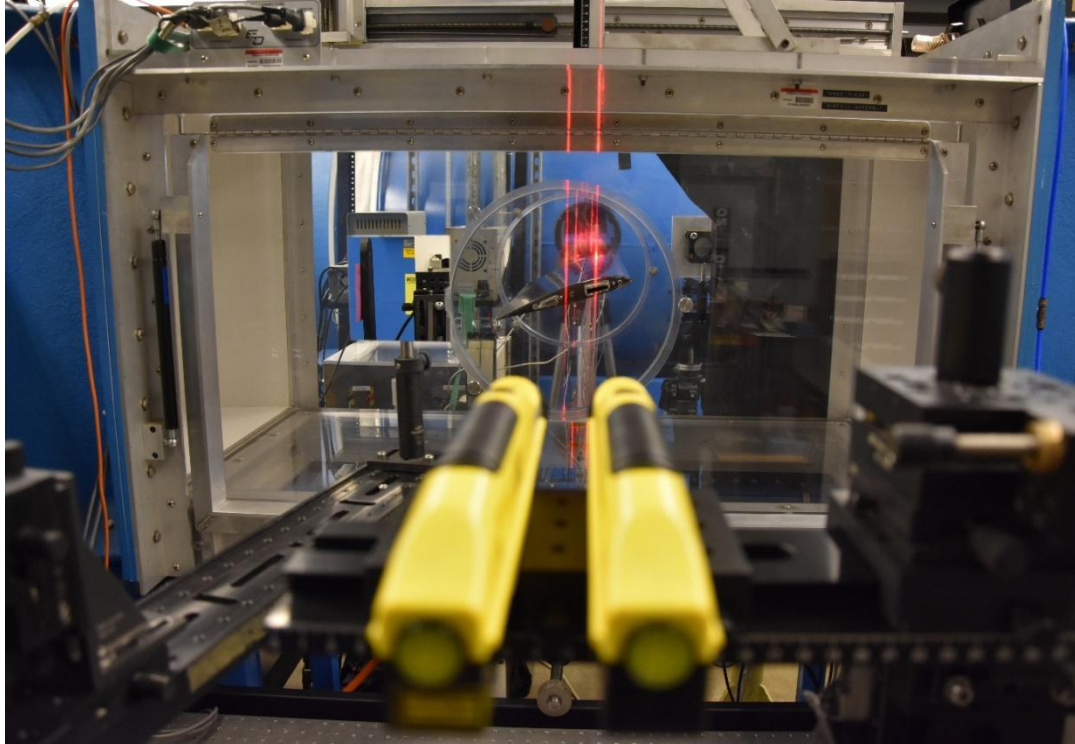a laser pointers for aligning the optics is demonstrated in Figure A.2.

Figure A.2 Using parallel laser lines for finding the focal point of parabolic mirrors

The measurements are depicted in Figures A.3 and A.4 for the illuminator and analyzer

sections of the system, respectively.

Second Parabolic Mirror

Φ_1

$L_1 = 157.66$ cm
(measured)

155.43 cm
(calculated)
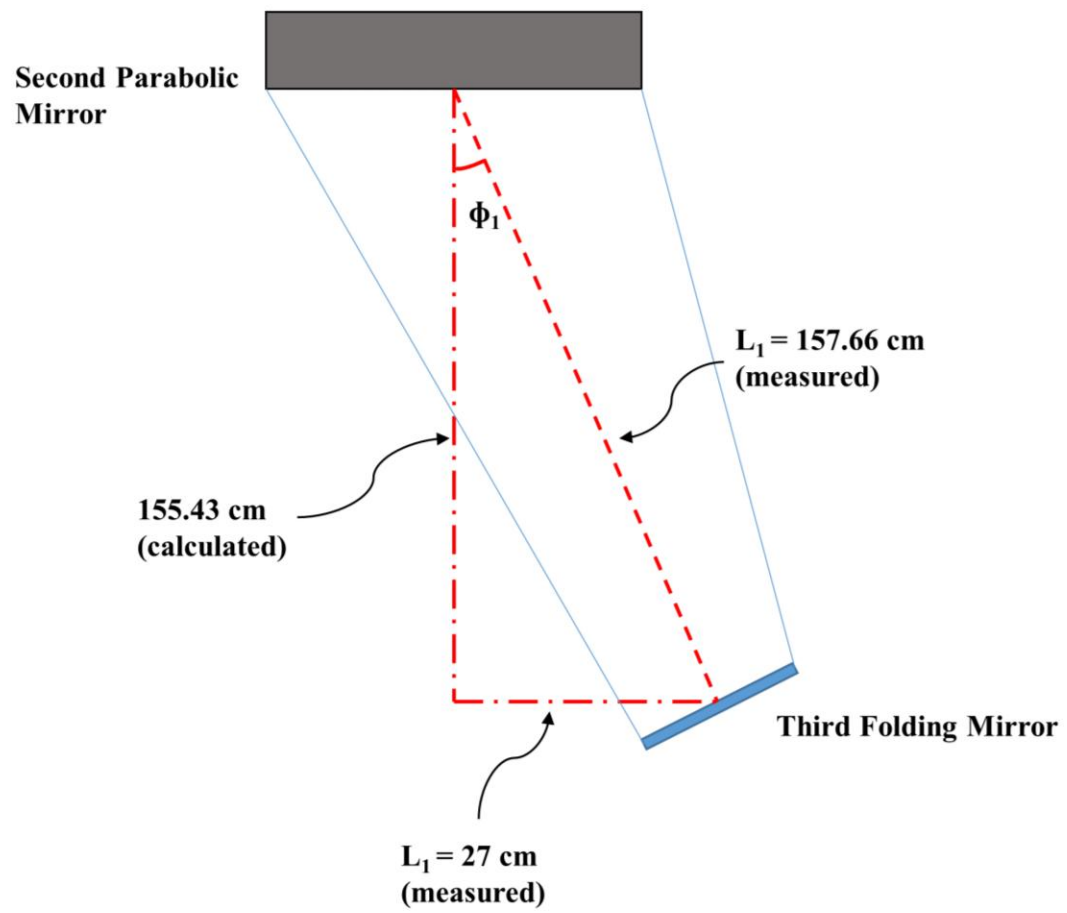
Third Folding Mirror

$L_1 = 27$ cm
(measured)
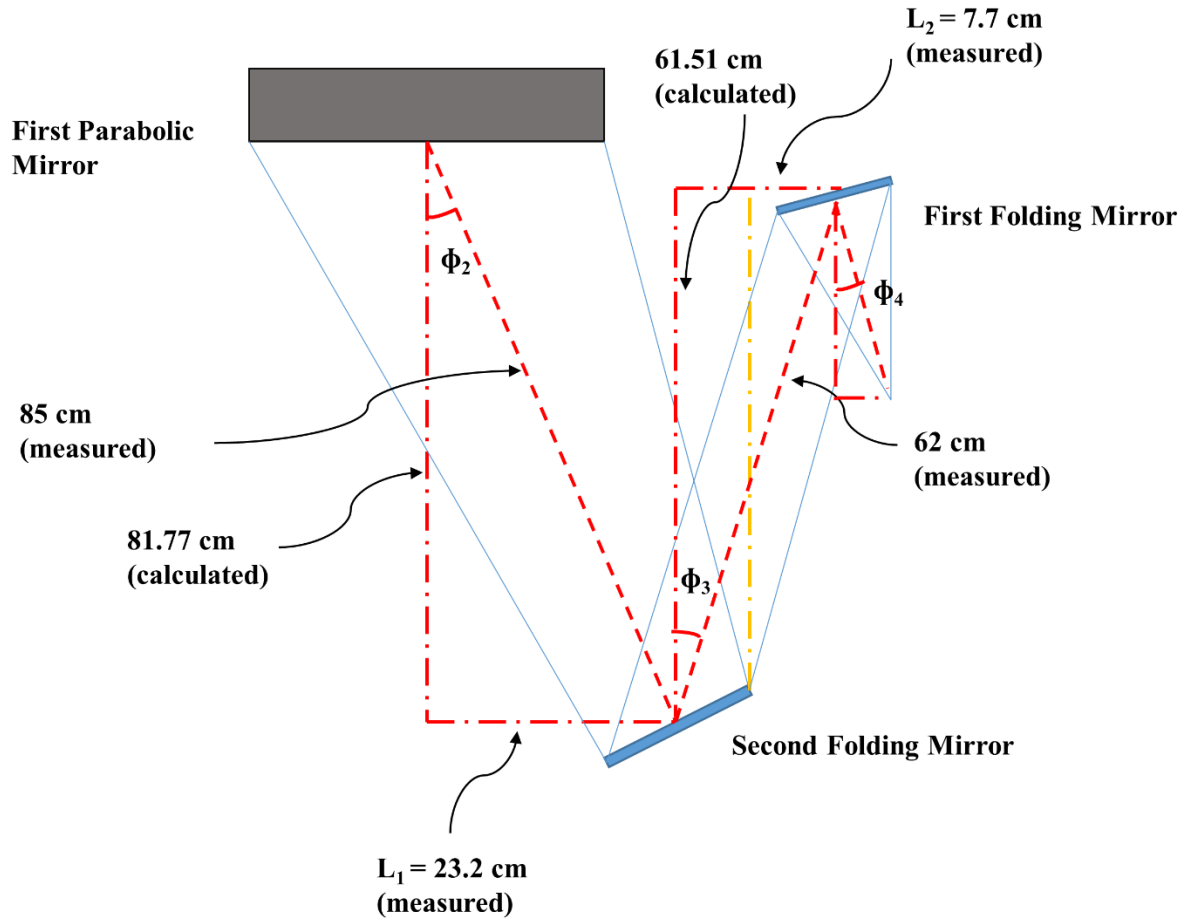
Figure A.3 Analyzer section of the system

Figure A.4 Illuminator section of the system

Settles[63] recommends using an off-axis angle of 6° to minimize astigmatic effects, however, due to the size of various optical elements in the present setup, it is impossible to bring down the off-axis angle to this level. Based on initial measurements, ϕ_1 was found to be equal to 10°, $\phi_2 = 16.48°$ and ϕ_3 was found to be negligible. After some

discussion with Nathan, it was decided to use the following relation to calculate ϕ_2 and ϕ_3 that need to be matched to ϕ_1 to compensate beam deflection effects.

$$\phi_1 = \sin^{-1}(\sin\phi_2 + \sin\phi_3)$$

To reduce ϕ_2 the spacing between the axes of second folding mirror and first parabolic mirror had to be reduced from 23.2 cm. Initial adjustments resulted in a portion of the source image being cut off by the edge of the second folding mirrors. After aligning the edge of the second folding mirror with the parabolic mirror using the reflections from a laser aligner, the spacing was reduced to 17.70 cm and ϕ_2 was reduced to 12.50°. Several attempts were made to reduce ϕ_3 but after inspecting the Schlieren image after each attempt, no significant difference in the observed blurriness in the image was observed. After another discussion with Nathan, we came to the conclusion that angles A1 and A2 (as can be seen in Figure A.5) are the only off-axis angles that play a crucial role in astigmatism correction (ϕ_1 and ϕ_2) and decided to concentrate our efforts on matching these two angles. Subsequently, no further attempts were made to adjust ϕ_3 and ϕ_4.
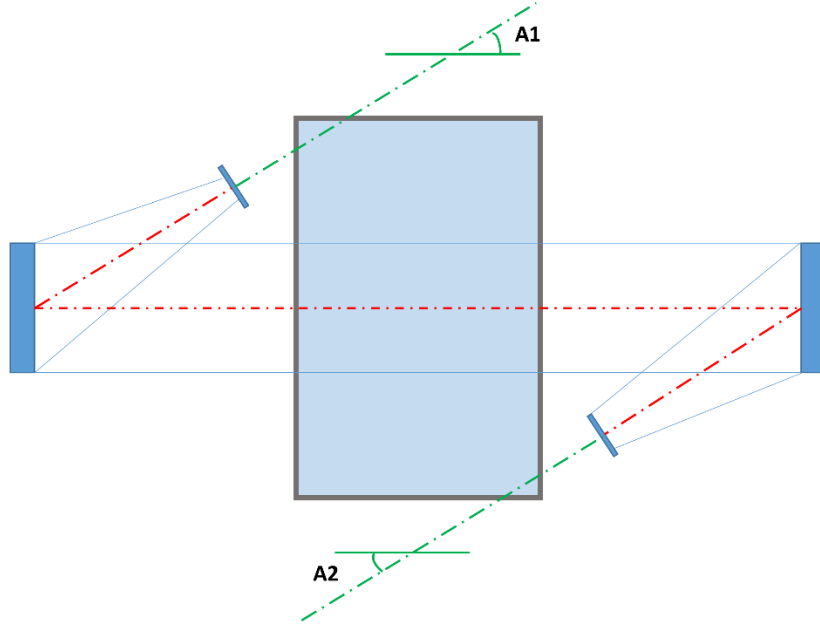
Figure A.5 Astigmatism can be effectively eliminated by matching A1 and A2

Finally, ϕ_1 was adjusted and brought up to 12.5° to match ϕ_2.

A.4 Calibration Process

The calibration approach employed in this work, as mentioned before, is based on the knife edge method described by Martinez[83] et al. At the heart of the method is a precision micrometer actuated stage that makes accurate movement of the knife edge possible. The construction of the precision mount for knife edge movement, taking data and obtaining calibration curves for each pixel are explained in detail in this section.

A.5 Building the Precision Mount for Calibration

Precise movement of knife edge in the vertical axis is needed to obtain an accurate calibration. The old mount was discarded and a new mount that can move in 3 axes was built using new and existing components. A heavy, height-adjustable mount was selected as a basis and the rest of the components were mounted on this assembly. A manual linear stage was used to enable coarse adjustments in y direction and the newly procured precision, micrometer-actuated stage was mounted on that for finer adjustments. Coarse lateral adjustments are made using a manual linear stage. A new assembly for housing the knife edge, protects the operator against sharp edges of the blade and makes rotation of the blade possible. The final assembly can be seen in Figure A.6.
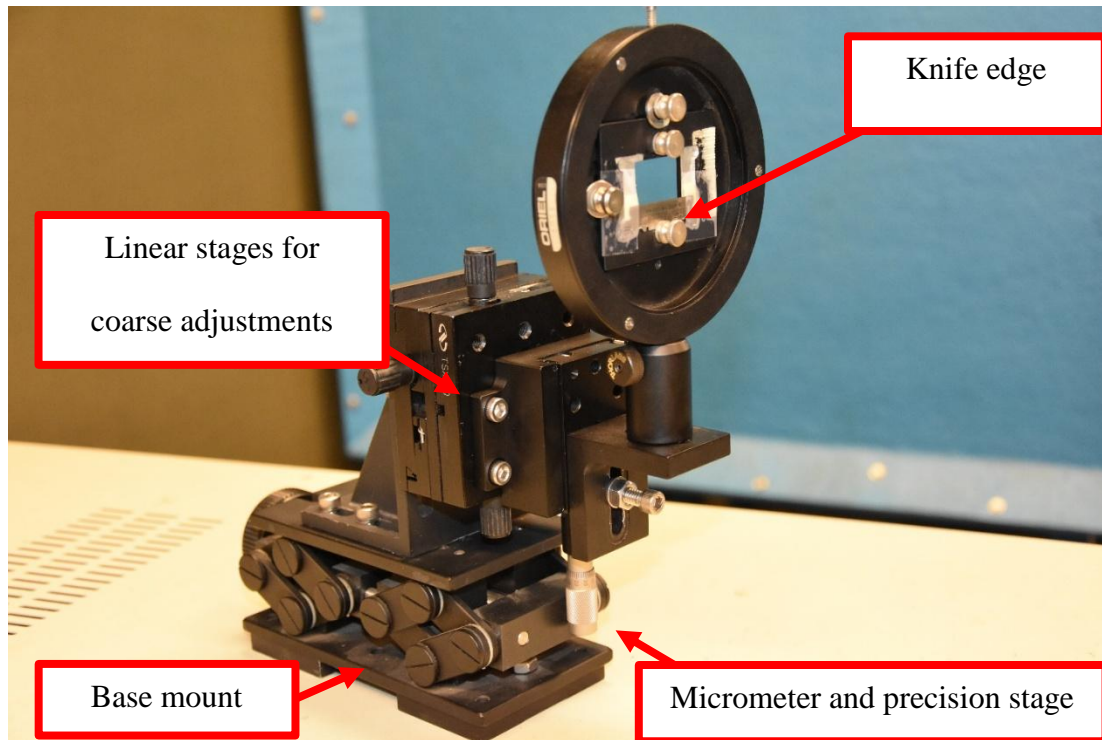
Figure A.6 Knife edge calibration assembly

A.6 Calibration

In order to assess the performance of the system, an initial calibration was performed. Based on the approximate height of the tangential image (astigmatic effects are reduced but still are present) which is roughly 1 mm, 5 cutoff values (0, 30, 55, 70 and 90 %) which correspond to 300, 550, 700 and 900 µm displacement of knife edge were chosen and images were acquired for each case. The acquired background images can be seen in Figure A.7.
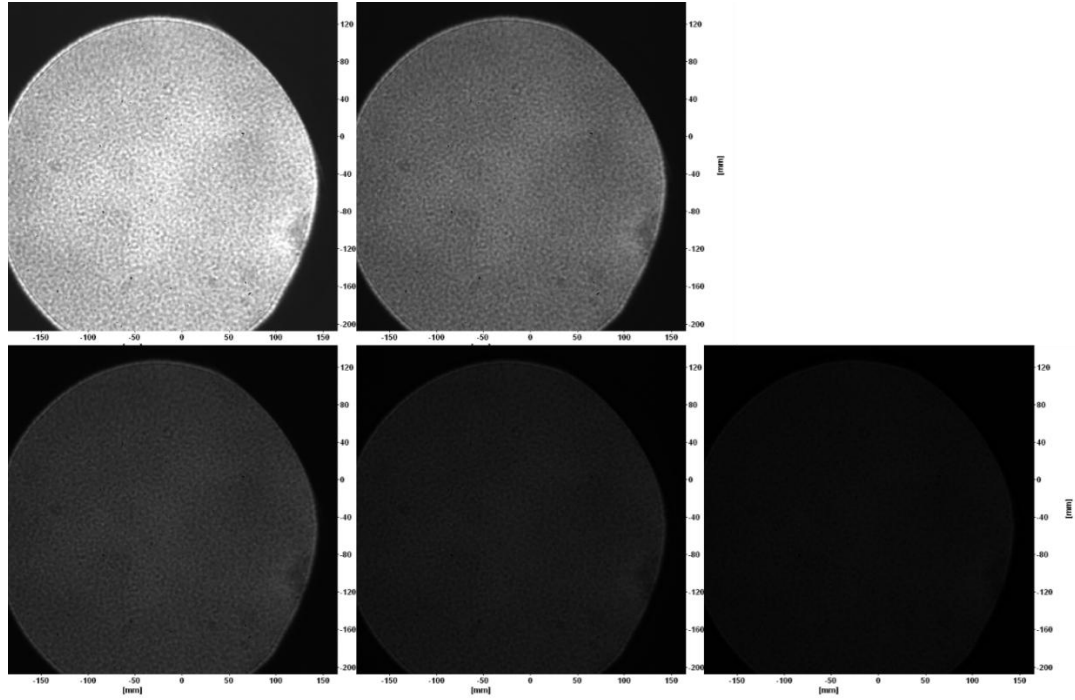
Figure A.7 Background images with different cutoff values

The acquired images were then imported in MATALB and converted into 16-bit grayscale matrices. The calibration must be performed for each pixel and this was done for two sample pixels at (238 294) and (238 52). The calibration curves for these two pixels can be seen in Figure A.8.
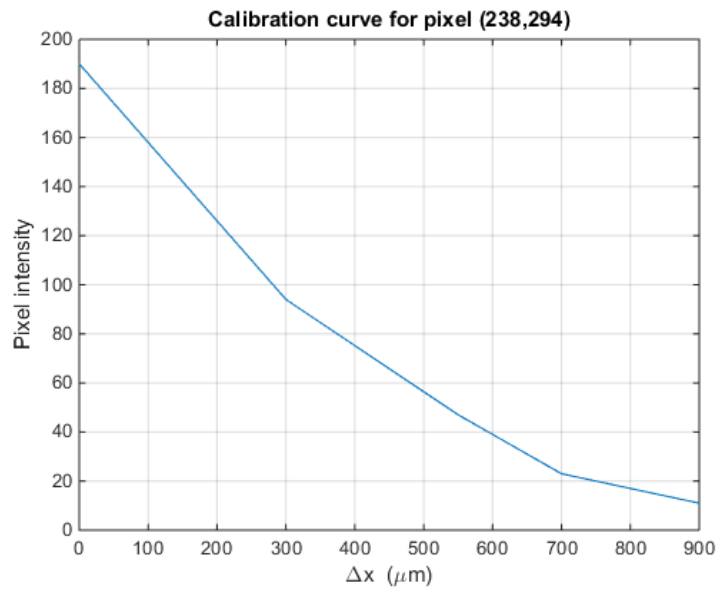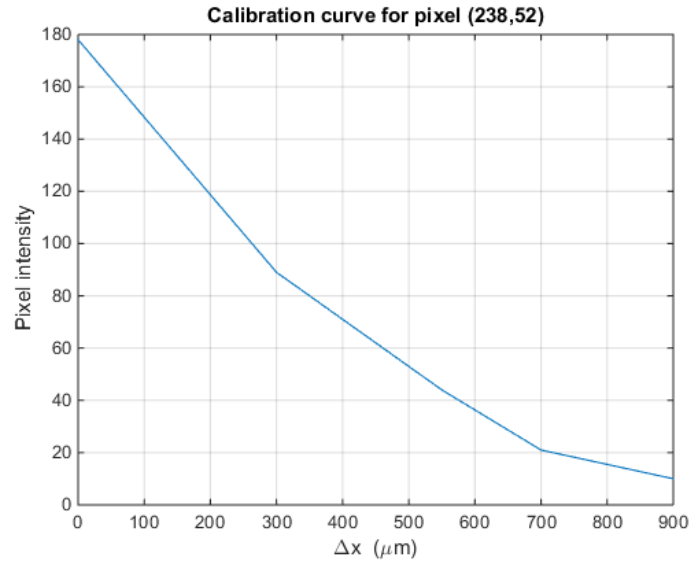
Figure A.8 Calibration curves for two pixels

A 2nd degree polynomial was then fitted to each curve to obtain intensity vs. displacement

functions for each pixel. The fitted curve equations are as follows

P (238 294)

Linear model Poly2:

$f(x) = p1*x^2 + p2*x + p3$

Coefficients (with 95% confidence bounds):

$p1 =$ *0.01886 (0.01281, 0.0249)*

$p2 =$ *-3.679 (-4.24, -3.119)*

$p3 =$ *189.5 (178.3, 200.6)*

P(238 52)

$f(x) = p1*x^2 + p2*x + p3$

Coefficients (with 95% confidence bounds):

$p1 =$ *0.01743 (0.01216, 0.0227)*

$p2 =$ *-3.434 (-3.923, -2.946)*

$p3 =$ *177.7 (167.9, 187.4)*

Given that the background is non-uniform due to imperfections in the optical interfaces (parabolic mirrors), the obtained calibration coefficients are within 8% of each other which seems acceptable. These values are not attainable, however, if the windows are

installed. Replacing the existing Acrylic side windows with the ones with optical quality will likely yield better calibration values in future experiments.